Predictions and Observations of Seafloor Infrasonic Noise Generated by Sea Surface Orbital Motion

THESIS
L663232

by

Timothy Edward Lindstrom

B.S., Electrical Engineering
Rochester Institute of Technology (1978)

Submitted in partial fulfillment of the
requirements for the degree of

OCEAN ENGINEER

at the

MASSACHUSETTS INSTITUTE OF TECHNOLOGY

and the

WOODS HOLE OCEANOGRAPHIC INSTITUTION

September 1991

© Timothy Edward Lindstrom, 1991

The author hereby grants to MIT, WHOI and the U.S. Government permission to reproduce and to distribute copies of this thesis document in whole or in part.

1 K2515
L663232
C.1

Predictions and Observations of Seafloor Infrasonic Noise Generated by Sea Surface Orbital Motion

by

Timothy Edward Lindstrom

Submitted to the Massachusetts Institute of Technology/
Woods Hole Oceanographic Institution
Joint Program in Oceanographic Engineering
on August 9, 1991, in partial fulfillment of the
requirements for the degree of
Ocean Engineer

Abstract

A model is developed for the prediction of the seismo-acoustic noise spectrum in the microseism peak region (0.1 to 0.7 Hz). The model uses a theory developed by Cato [J. Acoust. Soc. Am., 89 , 1096-1112 (1991)] for an infinite depth ocean in which the surface orbital motion caused by gravity waves may produce acoustic waves at twice the gravity wave frequency. Using directional wave spectra as inputs, acoustic source levels are computed and incorporated into a more realistic environment consisting of a horizontally stratified ocean with an elastic bottom. Noise predictions are made using directional wave spectra obtained from the SWADE surface buoys moored off the coast of Virginia and the SAFARI sound propagation code, with a bottom model derived using wave speeds measured in the EDGE deep seismic reflection survey. The predictions are analyzed for noise level variations with frequency, wave height, wind direction, and receiver depth. These predictions are compared to noise measurements made in ECONOMEX using near-bottom receivers located close to the surface buoys. Good agreement is found between the predictions and observations under a variety of environmental conditions.

Thesis Supervisor: Dr. George V. Frisk
Senior Scientist
Woods Hole Oceanographic Institution

Acknowledgements

I would like to thank a number of people whose help made this work possible. Foremost on this list are my thesis advisor, George Frisk, my co-advisor, Subramaniam Rajan, and my MIT advisor, Henrik Schmidt. These three were truly instrumental in the successful completion of both my course of study and my research, and are greatly deserving of my gratitude.

This particular thesis would not have been possible without the ECONOMEX and SWADE program support provided by the Office of Naval Research. Additionally, a great many individuals contributed directly to the sucess of these two experiments and to my understanding and data acquisition efforts. Among those at WHOI, I would like to especially thank Paul Boutin, John Collins, Jim Doutt, John Hallinan, and John Kemp. Those at other institutions who greatly aided my work include Steve Elgar, Hans Graber, and John Schneider. I would also like to thank Mike Purdy and Steve Holbrook for providing me with the EDGE data so soon after it was analyzed.

I will also be forever indebted to Eddie Scheer and Randy Richards for their help in my titanic struggle with the computer.

Finally I would like to acknowledge Captain Frank Lacroix, USN, whose professional guidance made it possible for me to become part of the Joint Program; and my wife Cindy, whose love and support made it all worthwhile.

Contents

1 Introduction **6**

2 Basic Equations **9**

3 Solution to the Inhomogeneous Wave Equation **13**

4 Application to Orbital Motion in the Deep Ocean **21**

5 Prediction Techniques **32**

5.1 SWADE data 32

5.2 Coupling factors and bottom gain 38

6 Predictions for Receivers at 450 meters and 2500 meters **42**

6.1 Variation of spectral level with frequency (spectral shape) 42

6.2 Variation of spectral level with wave height 44

6.3 Variation of spectral level with changing wind direction 46

6.4 Variation of spectral level with receiver depth 47

7 Experimental Noise Measurements **49**

7.1 Experimental description 49

7.2 Data selection and processing 51

7.3 Observed results and comparison with predictions 52

7.3.1 Spectral shape and overall spectral noise levels 52

7.3.2 Variation with wave height 52
7.3.3 Variation with changes in wind direction 54

8 Conclusions and Recommendations for Future Research 55
8.1 Conclusions 55
8.2 Recommendations for future research 56

Bibliography 58

Figures 61

Chapter 1

Introduction

Researchers have long been aware of a peak in both the seismic ambient ground motion spectrum and the ocean bottom pressure spectrum which occurs with a period of about three to four seconds. This peak has historically been called the microseism peak. It has been noted that the frequency of this peak seems to occur at twice the frequency of the peak in the surface gravity wave spectrum. Longuet-Higgins [1] was the first to develop a comprehensive theory which proposed the interaction of opposing surface waves, which closely approximate standing waves, as the source of the microseism peak. He showed that while the first-order pressure fluctuations caused by the gravity waves exhibit an exponential decay in depth, the second-order fluctuations caused by the nonlinear interaction of two opposing waves does not attenuate. Brekhovskikh [2] was the first to develop this idea into a prediction of noise in the ocean. He has been followed by others, most recently Kibblewhite and Wu [3], who all used a perturbation expansion as the solution to the wave equation with the resulting second order solution as the acoustic field. Cato [4] has developed a model which does not rely on a perturbation expansion, and does not require that a standing wave approximation be made. His theory predicts somewhat higher noise levels for a shallow receiver than those using the perturbation expansion, and a different directionality. In contrast to these predictions, which have the wave interaction as the source mechanism, are those of Guo [5] who has proposed the wind turbulence acting on the surface directly as the source of noise in the microseism peak region.

Previous measurements of noise in the deep ocean have been few, and the results have been broadly consistent with all the above theories [6,7,8,9]. What has been lacking is a direct accurate measurement of the source field believed to be causing the noise, either the wave field or the wind field. Without these quality source data, broad assumptions concerning the source field must be made, and the potential variance in the predictions based on these assumptions are typically greater than the differences in levels predicted by the different theories. Thus without the accurate measurement of the source field, it is difficult to evaluate the adequacy or inadequacy of particular theories. In the case of the surface wave field, the required measurements consist of directional surface wave spectra. This lack of high-quality, simultaneously measured, noise and surface wave data was the primary reason for the deployment of the ECONOMEX and SAMSON experiments [10,11]. An additional desirable feature of the ECONOMEX experiment was its long-term nature, allowing noise measurements under a wide variety of environmental conditions. The measurements consisted of near-seafloor water pressure and ground motion at various depths from ~100 meters to 2500 meters in the Atlantic Ocean. During the time the ECONOMEX instruments were deployed, instruments in the same area from the SWADE program were measuring surface parameters including directional wave spectra, wind speed, and other meteorological quantities. These two coupled data sets provide researchers with the measurements needed to test the theories mentioned above.

This work will examine the model developed by Cato [12] for an infinite depth ocean and will present the derivation of that model in detail. Using the SWADE directional wave spectra as inputs, we will estimate the resulting acoustic source level. We will then incorporate this source level into a more realistic environment consisting of a horizontally stratified ocean with an elastic bottom using the SAFARI program [13,14]. The geoacoustic model for our bottom comes in part from the EDGE deep seismic reflection study [15]. The resulting ambient noise predictions will then be compared to the measured noise from ECONOMEX in an effort to judge the adequacy of our model.

In Chap. 2, we review the equations of motion and derive the inhomogeneous wave equation in terms of the Lighthill analogy [16]. The inhomogeneous wave equation is then solved in the presence of a sound speed and density discontinuity in Chap. 3. In Chap. 4, we make some simplifications to allow us to apply the theory to the motion of surface gravity waves. Additionally in this chapter we follow the work of Cato [12] in deriving an expression for the noise level in terms of the directional wave spectrum, a problem for which we also introduce an elastic bottom. In Chap. 5 we describe the methods used to make predictions of noise levels using the equations in Chap. 4, the SWADE directional spectra, and the SAFARI program. Finally in Chap. 7 we present the ECONOMEX noise observations and compare them to our predictions which, for the most part, agree very well. Our conclusions and recommendations for future research are presented in Chap. 8.

Chapter 2

Basic Equations

In any consideration of sound generation, the most basic question to ask is "What is sound?" That is, how do we distinguish particle motions associated with acoustic energy from that associated with other types of energy such as vortical energy (that due to turbulence) or thermal energy? In general, this is a very difficult question, for the equations governing the three types of motion are a set of coupled, inhomogeneous, non-linear partial differential equations, first derived in a linear form by Rayleigh [17], and later in a more general form by Doak [18]. Doak further showed that for small Stokes number the set decouples into three separate equations for the acoustical, vortical, and thermal type motions. For our model of sound generation, we will consider only this decoupled, small Stokes number approximation, and introduce any coupling between the three types of motion via external forcing, heat addition, or boundary conditions. The acoustic motion is then easily recognized as the small scale pressure perturbation associated only with the internal elastic properties of the medium.

Let us consider the validity of the small Stokes number approximation in the case of low-frequency sound in the ocean. If we limit our interest to a maximum frequency of 50 Hz, then the maximum Stokes number ($\omega\nu/c^2$) is $\approx 10^{-7}$, where ω is the acoustic frequency, ν is the medium viscosity, and c is the sound speed. We are then justified in using the assumption of small Stokes number and can take advantage of the great mathematical and conceptual simplifications it allows.

In our derivation of the sound generated by a moving fluid, we will follow the acoustic analogy method of Lighthill [16], but will use the pressure perturbation as our field variable in preference to fluctuations in mass density as suggested by Doak [18]. We will first derive an expression for the pressure perturbations in an ideal acoustic medium at rest, and then derive a similar expression for a real fluid which may contain variations in density, variations in sound speed, and which can have existing within it any type of motion. When we compare the two expressions, the difference will contain the effects of motion in the real fluid which generate sound.

The exact equations of mass conservation and momentum can be written as

$$\frac{\partial \rho}{\partial t} + \frac{\partial(\rho u_i)}{\partial x_i} = 0, \tag{2.1}$$

$$\frac{\partial(\rho u_i)}{\partial t} + \frac{\partial(\rho u_i u_j + \sigma_{ij})}{\partial x_j} - \rho f_i = 0, \tag{2.2}$$

where ρ is the mass density, u_i is the fluid velocity in the x_i direction, σ_{ij} is the stress tensor consisting of hydrostatic and viscous stresses, and f_i is the body force in the x_i direction. The indices i and j may take any value 1, 2, or 3, corresponding to the Cartesian coordinate axes, and a repeated index in a term indicates the term is to be summed over all values of the index.

If we consider the "acoustic approximation", $p - p_0 = {c_o}^2(\rho - \rho_0)$, where p is the fluid pressure, then Eq. (2.1) can be rewritten

$$\frac{1}{{c_0}^2}\frac{\partial p}{\partial t} + \frac{\partial(\rho u_i)}{\partial x_i} = 0. \tag{2.3}$$

Doak has shown that this approximation is exact for an inviscid, non-heat conducting fluid, and valid for a Stokesian fluid to first order in the Stokes number.

Equation (2.2) can be applied to our ideal acoustic medium by linearizing it and neglecting viscous terms, leaving

$$\frac{\partial(\rho u_i)}{\partial t} + \frac{\partial p}{\partial x_i} = 0. \tag{2.4}$$

We can now combine Eqs. (2.3) and (2.4) by eliminating ρu_i to yield

$$\frac{\partial^2 p}{\partial t^2} - c_0^2 \frac{\partial^2 p}{\partial x_i^2} = 0. \tag{2.5}$$

This, then, is the familiar homogeneous wave equation governing the pressure perturbations in an ideal acoustic medium.

Now consider the exact equation of momentum balance, Eq. (2.2). This can be expanded as

$$\frac{\partial(\rho u_i)}{\partial t} + \frac{\partial p}{\partial x_i} = -\frac{\partial(\rho u_i u_j + S_{ij})}{\partial x_j} + \rho f_i, \tag{2.6}$$

where S is the viscous stress tensor, and the hydrostatic term has been explicitly stated. Next we again eliminate ρu_i by using the *exact* equation of mass conservation, Eq. (2.1). By adding $\partial^2 p/\partial x_i^2$ to both sides to allow direct comparison with Eq. (2.5), we arrive at

$$\frac{\partial^2 p}{\partial t^2} - c_0^2 \frac{\partial^2 p}{\partial x_i^2} = c_0^2 \frac{\partial^2(\rho u_i u_j + S_{ij})}{\partial x_i x_j} + \frac{\partial^2(p - c_0^2 \rho)}{\partial t^2} - c_0^2 \frac{\partial(\rho f_i)}{\partial x_i}. \tag{2.7}$$

This is the inhomogeneous wave equation as derived by Doak [18]. It is identical to that derived by Cato [4] with the exception of the final term, which he neglected. The pressure fluctuations in a real fluid are exactly those which would occur in a uniform acoustic fluid subject to the external stress system given by the right hand side of Eq. (2.7). As c_0^2 is assumed constant, not only the sound generation but also the propagation effects of a real fluid are included in the equivalent stress system. It will be our task not only to solve Eq. (2.7) in an ocean geometry with a realistic stress imposed, but also to separate out the sound generation terms from the propagation terms.

It is useful at this point to consider the importance of the term $c_0^2\partial(\rho f_i)/\partial x_i$, which was neglected by Cato in his theory of noise generated by surface orbital motion [4]. In the ocean, this term reduces to $c_0^2 g(\partial\rho/\partial z)$. We will consider motions with a periodic time dependence ($p \propto e^{-i\omega t}$) and a characteristic length scale L. Then we can form the ratio of the last to the first of the terms on the right hand side of Eq. (2.7) as $(g\rho/L)/(\rho u^2/L^2)$. From Eq. (2.1), we can see $|\rho U/L| \sim |\omega\rho|$ so we can rewrite our ratio as $g/L\omega^2$. We can also see from Eq. (2.1) that the first two terms on the right hand side of Eq. (2.7) are of the same order. If we consider as our worst case a minimum frequency of 0.1 Hz, we can neglect the gravity dependent term if $L \gg 25$m. If we were concerned with purely acoustic motion, the appropriate length scale would be the wavelength $L = \lambda = c/f \simeq$ 15,000 m. However the length scale appropriate to the equivalent sources resulting from surface gravity waves would be the wavelength obtained from the deep water low frequency surface gravity wave dispersion relation $\omega^2 = 2\pi g/\lambda$ which yields $L = \lambda \simeq 160$ m. In both cases we can therefore neglect the last term in Eq. (2.7).

Chapter 3

Solution to the Inhomogeneous Wave Equation

The general solution to the inhomogeneous wave equation is well known (cf. Stratton [19]). For the source term in Eq. (2.7), it is given by

$$
\begin{aligned}
&p(\mathbf{x},t) - p_0 = \\
&\quad \frac{1}{4\pi}\int_V \left[\frac{\partial^2(\rho u_i u_j + S_{ij})}{\partial y_i \partial y_j} + \frac{\partial^2(p/c_0^2 - \rho)}{\partial t^2}\right]_\tau \frac{d\mathbf{y}}{r} \\
&\quad + \frac{1}{4\pi}\int_S \left[\frac{1}{r}\frac{\partial p}{\partial n} + \frac{1}{r^2}\frac{\partial r}{\partial n} p + \frac{1}{c_0^2 r}\frac{\partial r}{\partial n}\frac{\partial p}{\partial t}\right]_\tau dS(\mathbf{y}), \qquad (3.1)
\end{aligned}
$$

where $r = |\mathbf{x} - \mathbf{y}|$, $\hat{n}$ is the outward normal to the surface of integration, and the integrands are evaluated at the retarded time $\tau = t - r/c$. The volume of integration above must include all possible regions where noise could be generated, and the surface integral will include the boundaries of these regions. We will choose our volume to be a cylinder of infinite height above the sea surface, and extending to the ocean bottom. The radius of this cylinder Y is assumed to be large enough to include any regions of motion which could contribute to $p(\mathbf{x}, t)$, and thus the sides of the cylinder do not contribute to the surface integral. We next follow

Cato [4] in modeling the sea surface density discontinuity as a Heaviside function so that the derivatives in Eq. (3.1) exist. The density is given by

$$\rho = H(\mathbf{x} - \varsigma)(\rho_w - \rho_a) + \rho_a$$

where ρ_w is the density in water, ρ_a is the density in air, ς is the value of $\mathbf{x}$ at the interface, and $H(\mathbf{x} - \varsigma)$ is the Heaviside function

$$\begin{aligned} H(y) &= 0, \quad y \geq 0, \\ H(y) &= 1, \quad y < 0. \end{aligned} \tag{3.2}$$

We can then expand terms containing spatial derivatives of ρ as follows:

$$\begin{aligned} &\frac{\partial^2(\rho u_i u_j)}{\partial y_i \partial y_j} = \\ &H\frac{\partial^2}{\partial y_i \partial y_j}(\rho_w - \rho_a)u_i u_j + \frac{\partial^2}{\partial y_i \partial y_j}(\rho_a u_i u_j) \\ &+2\frac{\partial H}{\partial y_i}\frac{\partial}{\partial y_j}(\rho_w - \rho_a)u_i u_j + (\rho_w - \rho_a)u_i u_j \frac{\partial^2}{\partial y_i \partial y_j}H. \end{aligned} \tag{3.3}$$

We can also combine Eqs. (2.1) and (2.2) to yield

$$\frac{\partial^2 \rho}{\partial t_2} = \frac{\partial^2(\rho u_i u_j + \sigma_{i,j})}{\partial y_i \partial y_j}, \tag{3.4}$$

which can be used with Eq. (3.3) to eliminate the derivatives of the Heaviside function in Eq. (3.1) resulting in

$$\begin{aligned} &4\pi(p(\mathbf{x}, t) - p_0) = \\ &\int_V \frac{d\mathbf{y}}{r}\left[H\frac{\partial^2}{\partial y_i \partial y_j}(\rho_w u_i u_j) + (1 - H)\frac{\partial^2}{\partial y_i \partial y_j}(\rho_a u_i u_j) + \frac{\partial^2 S_{ij}}{\partial y_i \partial y_j}\right]_\tau \\ &-\int_V \frac{d\mathbf{y}}{r}\left[H\frac{\partial^2}{\partial y_i \partial y_j}(\rho_w u_i u_j) + (1 - H)\frac{\partial^2}{\partial y_i \partial y_j}(\rho_a u_i u_j) + \frac{\partial^2 S_{ij}}{\partial y_i \partial y_j} - \frac{\partial^2}{\partial t^2}(\frac{\mathrm{p}}{c_0^2})\right]_\tau \\ &+\int_S \left[\frac{1}{r}\frac{\partial p}{\partial n} + \frac{1}{r^2}\frac{\partial r}{\partial n}p + \frac{1}{c_0^2 r}\frac{\partial r}{\partial n}\frac{\partial p}{\partial t}\right]_\tau dS(\mathbf{y}). \end{aligned} \tag{3.5}$$

Now we can split the volume integral into one integral over the water volume and one integral over the air volume, noting that $H = 1$ in water and $H = 0$ in water, and after recombining terms to form $\partial^2\rho/\partial t^2$ we find

$$4\pi(p(\mathbf{x},t) - p_0) =$$

$$\int_{V_w} \frac{d\mathbf{y}}{r} \left[\frac{\partial^2}{\partial y_i y_j}(\rho_w u_i u_j + S_{ij}) + \frac{\partial^2}{\partial t^2}(\frac{p}{c_0^2} - \rho_w) \right]_\tau$$

$$+ \int_{V_a} \frac{d\mathbf{y}}{r} \left[\frac{\partial^2}{\partial y_i \partial y_j}(\rho_a u_i u_j + S_{ij}) + \frac{\partial^2}{\partial t^2}(\frac{p}{c_0^2} - \rho_a) \right]_\tau$$

$$+ \int_S \left[\frac{1}{r}\frac{\partial p}{\partial n} + \frac{1}{r^2}\frac{\partial r}{\partial n}p + \frac{1}{c_0^2 r}\frac{\partial r}{\partial n}\frac{\partial p}{\partial t} \right]_\tau dS(\mathbf{y}). \tag{3.6}$$

As before, the integrands must be evaluated at time $\tau = t - r/c$

The next step is to apply the divergence theorem in a manner first described by Curle [20], and presented in detail by Cato [12]. This is not a straightforward process, as the terms to be evaluated depend on $\mathbf{y}$ both directly and also through the dependence on r. Curle stated and Cato demonstrated that

$$\int_V \frac{\partial^2 F_{ij}}{\partial y_i \partial y_j}\frac{d\mathbf{y}}{r} - \frac{\partial}{\partial x_i}\int_V \frac{\partial F_{ij}}{\partial y_j}\frac{d\mathbf{y}}{r} = \int_V \frac{\partial}{\partial y_i}\left[\frac{\partial F_{ij}}{\partial y_j}\frac{1}{r}\right]_\tau d\mathbf{y}$$

$$= \int_S l_i \frac{\partial F_{ij}}{\partial y_j}\frac{dS(\mathbf{y})}{r}, \tag{3.7}$$

where l_i are the direction cosines of the outward normal of the surface enclosing V. We can then repeat this operation a second time to yield

$$\int_V \frac{\partial F_{ij}}{\partial y_j}\frac{d\mathbf{y}}{r} - \frac{\partial}{\partial x_i}\int_V F_{ij}\frac{d\mathbf{y}}{r} = \int_S l_j Fij \frac{dS(\mathbf{y})}{r}. \tag{3.8}$$

We can now combine Eqs. (3.8) and (3.9) to achieve Curle's result

$$\int_V \frac{\partial^2 F_{ij}}{\partial y_i y_j}\frac{d\mathbf{y}}{r} =$$

$$\frac{\partial^2}{\partial x_i \partial x_j}\int_V F_{ij}\frac{d\mathbf{y}}{r} + \frac{\partial}{\partial x_i}\int_S l_j F_{ij}\frac{d\mathbf{y}}{r} + \int_S l_i \frac{\partial F_{ij}}{\partial y_j}\frac{dS(\mathbf{y})}{r}. \tag{3.9}$$

We can also easily transform the surface integral in Eq. (3.1) as follows. First we resolve the normal derivatives into Cartesian coordinates which yields

$$\int_S \left[\frac{1}{r}\frac{\partial p}{\partial n} + \frac{1}{r^2}\frac{\partial r}{\partial n}p + \frac{1}{c_0^2 r}\frac{\partial r}{\partial n}\frac{\partial p}{\partial t}\right]_\tau dS(\mathrm{y}) =$$

$$\int_S l_i \left[\frac{1}{r}\frac{\partial p}{\partial y_i} + \frac{1}{r^2}\frac{\partial r}{\partial y_i}p + \frac{1}{c_0^2 r}\frac{\partial r}{\partial y_i}\frac{\partial p}{\partial t}\right]_\tau dS(\mathrm{y}). \tag{3.10}$$

By substituting $\partial r/\partial y_i = -\partial r/\partial x_i$ and $\partial p/\partial y_i = \partial(p\delta_{ij})/y_j$, we have

$$\int_S l_i \left[\frac{1}{r}\frac{\partial p}{\partial y_i}\frac{1}{r^2}\frac{\partial r}{\partial y_i}p + \frac{1}{c_0^2 r}\frac{\partial r}{\partial y_i}\frac{\partial p}{\partial t}\right]_\tau dS(\mathrm{y}) =$$

$$\int_S l_i \frac{\partial(p\delta_{ij})}{\partial y_j}\frac{dS(\mathrm{y})}{r} - \int_S l_i \left[\frac{1}{r}\frac{\partial r}{\partial x_i}p + \frac{1}{c_0^2}\frac{\partial r}{\partial x_i}\frac{\partial p}{\partial t}\right]_\tau \frac{dS(\mathrm{y})}{r}. \tag{3.11}$$

Next we note that

$$\frac{\partial}{\partial x_i}\left[\frac{1}{r}f\left(t - \frac{r}{c}\right)\right] = -\left[\frac{1}{r^2}f + \frac{1}{cr}f'\right]\frac{\partial r}{\partial x_i},$$

so that we can write

$$-\int_S l_i \frac{\partial(p\delta_{ij})}{\partial y_j}\frac{dS(\mathrm{y})}{r} - \int_S l_i \left[\frac{1}{r}\frac{\partial r}{\partial x_i}p + \frac{1}{c_0^2}\frac{\partial r}{\partial x_i}\frac{\partial p}{\partial t}\right]_\tau \frac{dS(\mathrm{y})}{r}$$

$$= \int_S l_j \frac{\partial}{\partial x_i}p\delta_{ij}\frac{dS(\mathrm{y})}{r}. \tag{3.12}$$

Combining Eqs. (3.10), (3.11), and (3.12) yields

$$\int_S \left[\frac{1}{r}\frac{\partial p}{\partial n} + \frac{1}{r^2}\frac{\partial r}{\partial n}p + \frac{1}{c_0^2 r}\frac{\partial r}{\partial n}\frac{\partial p}{\partial t}\right]_\tau dS(\mathrm{y}) =$$

$$\int_S l_i \frac{\partial(p\delta_{ij})}{\partial y_j}\frac{dS(\mathrm{y})}{r} + \int_S l_j \frac{\partial}{\partial x_i}p\delta_{ij}\frac{dS(\mathrm{y})}{r}. \tag{3.13}$$

Now we substitute Eqs. (3.9) and (3.13) into Eq. (3.5). After noting that the source motions at infinity do not contribute, we can separate the surface integrals enclosing the water volume into one at the air-sea interface designated S_i and one at the ocean bottom designated S_b, and can then combine the surface integral at the bottom derived by applying the divergence theorem to V_w with the surface integral of Eq. (3.13). This yields

$$
\begin{aligned}
&4\pi(p(\mathbf{x},t)-p_0)= \\
&\frac{\partial^2}{\partial x_i \partial x_j}\int_{V_w}(\rho_w u_i u_j + S_{ij})\frac{d\mathbf{y}}{r} + \int_{V_w}\frac{\partial^2}{\partial t^2}(\frac{p}{c_0^2}-\rho_w)\frac{d\mathbf{y}}{r} \\
&+\frac{\partial^2}{\partial x_i \partial x_j}\int_{V_a}(\rho_a u_i u_j + S_{ij})\frac{d\mathbf{y}}{r} + \int_{V_a}\frac{\partial^2}{\partial t^2}(\frac{p}{c_0^2}-\rho_a)\frac{d\mathbf{y}}{r} \\
&-\frac{\partial}{\partial x_i}\int_{S_i} l_j(\rho_w u_i u_j + S_{ij})\frac{dS(\mathbf{y})}{r} - \int_{S_i} l_i\left[\frac{\partial}{\partial y_j}(\rho_w u_i u_j + S_{ij})\right]\frac{dS(\mathbf{y})}{r} \\
&+\frac{\partial}{\partial x_i}\int_{S_i} l_j(\rho_a u_i u_j + S_{ij})\frac{dS(\mathbf{y})}{r} + \int_{S_i} l_i\left[\frac{\partial}{\partial y_j}(\rho_a u_i u_j + S_{ij})\right]\frac{dS(\mathbf{y})}{r} \\
&+\frac{\partial}{\partial x_i}\int_{S_b} l_j(\rho_w u_i u_j + S_{ij} + p\delta_{ij})\frac{dS(\mathbf{y})}{r} \\
&+\int_{S_b} l_i\left[\frac{\partial}{\partial y_j}(\rho_w u_i u_j + S_{ij} + p\delta_{ij})\right]\frac{dS(\mathbf{y})}{r}. \qquad (3.14)
\end{aligned}
$$

We can transform the $\mathbf{y}$ derivatives to time derivatives by noting from Eq. (2.2) that

$$l_i\left[\frac{\partial}{\partial y_j}(\rho u_i u_j + S_{ij} + p\delta_{ij})\right] = -l_i\frac{\partial}{\partial t}(\rho u_i),$$

and by defining $\Delta\rho = (\rho_w - \rho_a)$, we can finally write

$$
\begin{aligned}
&4\pi(p(\mathbf{x},t)-p_0)= \\
&\frac{\partial^2}{\partial x_i \partial x_j}\int_{V_w}(\rho_w u_i u_j + S_{ij})\frac{d\mathbf{y}}{r} + \int_{V_w}\frac{\partial^2}{\partial t^2}(\frac{p}{c_0^2}-\rho_w)\frac{d\mathbf{y}}{r} \\
&+\frac{\partial^2}{\partial x_i \partial x_j}\int_{V_a}(\rho_a u_i u_j + S_{ij})\frac{d\mathbf{y}}{r} + \int_{V_a}\frac{\partial^2}{\partial t^2}(\frac{p}{c_0^2}-\rho_a)\frac{d\mathbf{y}}{r} \\
&-\frac{\partial}{\partial x_i}\int_{S_i} l_j(\Delta\rho u_i u_j)\frac{dS(\mathbf{y})}{r} + \int_{S_i} l_i\frac{\partial}{\partial t}(\Delta\rho u_i)\frac{dS(\mathbf{y})}{r}
\end{aligned}
$$

$$+\frac{\partial}{\partial x_i}\int_{S_b} l_j(\rho_w u_i u_j + S_{ij} + p\delta_{ij})\frac{dS(\mathrm{y})}{r}$$

$$+\int_{S_b} l_i\frac{\partial}{\partial t}(\rho_w u_i)\frac{dS(\mathrm{y})}{r}. \tag{3.15}$$

We can now begin to interpret the meaning of Eq. (3.15) in terms of the sources of classical acoustics. The double spatial derivatives of the volume integrals are recognized as distributions of quadrupole sources in the volume V, and the single spatial derivatives of the volume integrals are recognized as dipole source distributions in the volume V. The spatial derivatives of the surface integrals at the interface are seen as dipole sources caused by the motion of the surface of the density discontinuity, and similarly the surface integrals of the time derivatives are seen as monopole source distributions caused by the motion of the surface of the density discontinuity. These interpretations are those given by Lighthill [16].

In order to interpret the terms involving the double time derivatives, we must make a further approximation to allow us to simplify Eq. (3.15), although it is one that is frequently made in classical acoustics. If we assume that the fluids are isentropic, then the density and pressure are simply related by $\partial p/\partial\rho = c^2$, where c is the local speed of sound [21]. Also, if entropy is conserved, the processes are reversible and the dissipative effects of viscosity can be ignored. (Note we must now treat the effects of attenuation due to absorption separately.) With no viscosity, $S_{ij} = 0$, or $\sigma_{ij} = p\delta_{ij}$. We can thus write

$$\frac{\partial^2}{t^2}\left(\frac{p}{c_o^2}-\rho\right) = \frac{\partial^2}{t^2}\left(\frac{p}{c_o^2}-\frac{p}{c^2}\right),$$

or using Eq. (3.4) we have

$$\frac{\partial^2}{t^2}\left(\frac{p}{c_o^2}-\rho\right) = \left(\frac{c^2}{c_0^2}-1\right)\frac{\partial^2\rho}{\partial t^2} =$$

$$\left(\frac{c^2}{c_0^2}-1\right)\left[\frac{\partial^2}{\partial y_i\partial y_j}(\rho u_i u_j + \sigma_{ij})\right]. \tag{3.16}$$

We can again apply the divergence theorem twice to Eq. (3.16) to yield

$$\int_V \frac{\partial^2}{t^2}\left(\frac{p}{c_o^2}-\rho\right)\frac{dy}{r} =$$

$$\frac{\partial^2}{\partial x_i \partial x_j}\int_V \left(\frac{c^2}{c_0^2}-1\right)(\rho u_i u_j + p\delta_{ij})\frac{dy}{r}$$

$$+\frac{\partial}{\partial x_i}\int_S l_j \left(\frac{c^2}{c_0^2}-1\right)(\rho u_i u_j + p\delta_{ij})\frac{dy}{r}$$

$$-\int_S l_i \frac{\partial}{\partial t}\left[\left(\frac{c^2}{c_0^2}-1\right)\rho u_i\right]\frac{S(y)}{r}. \tag{3.17}$$

From the above, we note that we can again identify both a quadrupole and a dipole volume source distribution, and both a dipole and a monopole surface distribution. Next we combine Eqs. (3.17) and (3.15) resulting in

$$4\pi(p(x,t)-p_0) =$$

$$\frac{\partial^2}{\partial x_i \partial x_j}\int_{V_w}\left[\frac{c^2}{c_0^2}(\rho_w u_i u_j + p\delta_{ij}) - p\delta_{ij}\right]\frac{dy}{r}$$

$$+\frac{\partial^2}{\partial x_i \partial x_j}\int_{V_a}\left[\frac{c^2}{c_0^2}(\rho_a u_i u_j + p\delta_{ij}) - p\delta_{ij}\right]\frac{dy}{r}$$

$$-\frac{1}{c_0^2}\frac{\partial}{\partial x_i}\int_{S_i} l_j\left[(\rho_w c_w^2 - \rho_a c_a^2)u_i u_j + (c_w^2 - c_a^2)p\delta_{ij}\right]\frac{dS(y)}{r}$$

$$+\frac{1}{c_0^2}\int_{S_i} l_j \frac{\partial}{\partial t}\left[(\rho_w c_w^2 - \rho_a c_a^2)u_i\right]\frac{dS(y)}{r}$$

$$+\frac{\partial}{\partial x_i}\int_{S_b} l_j \frac{c_w^2}{c_0^2}(\rho_w u_i u_j) + p\delta_{ij})\frac{dS(y)}{r}$$

$$-\int_{S_b} l_i \frac{\partial}{\partial t}(\frac{c_w^2}{c_0^2}\rho_w u_i)\frac{dS(y)}{r}. \tag{3.18}$$

This result shows that the sound received at a point is the sum of apparent sources distributed throughout the source volume, at the air-sea interface, and at the ocean bottom. The effects of the real ocean, such as refraction, are included in Eq. (3.18). The reflection from the ocean surface and bottom are also modeled in Eq. (3.18). Our next step will be to further simplify Eq. (3.18) to identify the real sources which transform other types of energy into acoustic energy, and to show how the sound generated by these real sources is modified by a homogeneous ocean.

Chapter 4

Application to Orbital Motion in the Deep Ocean

Equation (3.18) is quite general and could in theory be used to predict the acoustic pressure for a given source mechanism, but would require a knowledge of the particle motions u_i throughout the volume of the ocean and on the boundaries. In addition, the effects of a real fluid such as refraction are modeled as apparent sources, which further confuses the issue. We will now begin to make assumptions which will greatly simplify Eq. (3.18) to allow us to use it to predict infrasonic noise generated by the sea surface orbital motion.

We first assume a plane wave sea surface elevation

$$\varsigma = a\cos(\boldsymbol{\kappa}\cdot\mathbf{x}' - \sigma t), \tag{4.1}$$

where ς is the sea surface elevation, a is the amplitude, $\boldsymbol{\kappa}$ is the wavenumber vector, $\mathbf{x}' = x_1\hat{\imath} + x_2\hat{\jmath}$ is the horizontal position vector, and σ is the radian gravity wave frequency. The solution to the linear equations of motion yields a velocity potential ϕ at depth $x_3 = z$ given by

$$\phi = \frac{\sigma a \cosh\kappa(z+d)}{\kappa\sinh\kappa d}\sin(\boldsymbol{\kappa}\cdot\mathbf{x}' - \sigma t), \tag{4.2}$$

where d is the total water depth and $\kappa = |\boldsymbol{\kappa}|$ [22]. Ignoring surface tension, this leads to the dispersion relationship

$$\sigma^2 = g\kappa \tanh \kappa d, \tag{4.3}$$

where g is the gravitational constant. If we restrict ourselves to water deep enough to satisfy $\kappa d > \pi/2$, Eq. (4.3) reduces to the deep water surface gravity wave dispersion relation

$$\sigma^2 = \kappa g. \tag{4.4}$$

We then find the particle motions to be

$$\begin{aligned} x_i' &= a e^{\kappa z_0} \sin(\boldsymbol{\kappa} \cdot \mathbf{x}_0' - \sigma t), \quad i = 1, 2, \\ z &= a e^{\kappa z_0} \cos(\boldsymbol{\kappa} \cdot \mathbf{x}_0' - \sigma t), \end{aligned} \tag{4.5}$$

where the initial position of the particle is $(\mathbf{x}_0', z_0)$. We can see that the particles describe a circular path, and hence the term orbital motion. Now we must determine the minimum water depth for which we may neglect the orbital motions at the bottom. We will also need to find the minimum water depth for which Eq. (4.4) holds. If we consider a minimum gravity wave frequency of 0.05 Hz, the deep water dispersion relationship is valid in water depths $\geq$ 200m. To find the depth at which we can neglect orbital motion on the bottom, we consider the $e^{-\kappa z}$ decay with depth and we find the orbital motions are 5% of the surface value at a water depth $\geq$ 300m. We will therefore consider to be the effective source generation region to be $\leq$300 m. Outside this region we may neglect the volume integral of Eq. (3.18) and also neglect the orbital motions on the bottom.

We can eliminate any apparent sources caused by refraction by considering the case of an isovelocity ocean, or $c_w = c_0$, and by considering the air also to be isovelocity, $c_a = \overline{c_a}$. We can also eliminate a number of terms in Eq. (3.18) by noting that $c_w^2 \gg c_a^2$ and $\rho_w c_w^2 \gg \rho_a c_a^2$. Thus, we neglect the air volume integral, and we assume the upper half-space to be a vacuum. We have now reduced the motions on the bottom to those due only to the motion of the acoustic wave. Thus, in Eq. (3.18) we can eliminate from the bottom integral the $\rho_w u_i u_j$ and $\partial(\rho u)/\partial t$ terms, since for an acoustic wave $\rho u \ll p$. After all these simplifications, we are left with

$$\begin{aligned} 4\pi(p(\mathrm{x},t) - p_0) &= \frac{\partial^2}{\partial x_i \partial x_j} \int_{V_w} \rho_w u_i u_j \frac{d\mathrm{y}}{r} \\ &- \frac{\partial}{\partial x_i} \int_{S_i} l_j \left[\rho_w u_i u_j + p\delta_{ij}\right] \frac{dS(\mathrm{y})}{r} \\ &+ \int_{S_i} l_j \frac{\partial}{\partial t} \left[\rho_w u_i\right] \frac{dS(\mathrm{y})}{r} + \frac{\partial}{\partial x_i} \int_{S_b} l_j p \delta_{ij} \frac{dS(\mathrm{y})}{r}. \end{aligned} \tag{4.6}$$

One can now identify each term in Eq. (4.6) and relate it to a specific physical mechanism. The quadrupole volume integral involving $\rho u_i u_j$ is identified as the volume contribution to the second order pressure fluctuation first proposed as the cause of microseisms by Longuet-Higgins [1] . The dipole surface integral involving $\rho u_i u_j$ is identified as the sea surface contribution to this mechanism. The monopole surface integral containing $\frac{\partial}{\partial t}\rho u_i$ is identified as the first order pressure effect which attenuates with depth. The apparent sources due to the surface and bottom reflections are contained in the two $p\delta_{ij}$ terms . We can see in this case that the bottom does not influence the real source terms directly, and the real sources caused by the transformation of mechanical energy to acoustic energy can be evaluated first, and the bottom effects added later.

Cato has shown [4] the quadrupole contribution to be $\leq 2\sigma/c\kappa$ times the dipole contribution in the far field, which is defined by $r\kappa > 1$. For a minimum wave frequency of 0.05 Hz, this is then valid at depths greater than 100 m below the region of effective volume generation, which we found to be no greater than 300 m. Thus we are able to ignore the quadrupole term for receivers greater than 400 m. Since we are mainly interested in the microseism peak region, we will also neglect the monopole term, although it will be significant at moderate depths for frequencies below the microseism peak.

In finding the acoustic source level, we must make two major calculations. The first is to relate the source acoustic power density $P(\omega, z)$ to the frequency-wavenumber spectrum of the source motions $\rho u_i u_j$. We must then relate this spectrum, say $\Phi(\omega, \mathrm{k})$, to $\Omega(\sigma)$ which is the readily measured power spectrum of the sea surface elevation ς. Both of these derivations have been performed by Cato [4,12], and we will present the important steps for the dipole sources below. We must then incorporate these source levels into an appropriate ocean model to find the noise power for an ocean receiver.

We start by redefining some terms. Let

$$p_D(\mathrm{x}, t) = \frac{\partial}{\partial x_i} \int_S l_j G(r) W_{ij}(\hat{\mathrm{y}}, \tau) dy, \tag{4.7}$$

where $W_{ij} = \rho u_i u_j$, $G(r) = 1/(4\pi r)$, and $\hat{\mathrm{y}}$ is the source coordinate on the sea surface. Since we will perform the integration over the mean sea surface, we can immediately align the x_3 axis with the depth axis z and then $l_1 = l_2 = 0$, $l_3 = 1$, and $W_{ij} = W_i = \rho u_i u_3$. We assume W_i to be temporally stationary and ergodic, and spatially homogeneous. Then the autocorrelation function of $p_D(\mathrm{x}, t)$ is

$$R_p(t, t+\varsigma) = \langle (p_D(\mathrm{x}, t) p_D(\mathrm{x}, t+\varsigma) \rangle, \tag{4.8}$$

and since the process is ergodic

$$R_p(t+\varsigma) = R_p(\varsigma) = \lim_{T\to\infty} \frac{1}{2T} \int_{-T}^{T} p_D(\mathrm{x}, t) p_D(\mathrm{x}, t+\varsigma) dt, \tag{4.9}$$

and the power spectrum is

$$\begin{aligned} Q_D(\omega) &= \lim_{T\to\infty} \int_{-\infty}^{\infty} \frac{1}{2T} \int_{-T}^{T} p_D(\mathrm{x}, t) p_D(\mathrm{x}, t+\varsigma) dt\, e^{i\omega\varsigma} d\varsigma \\ &= \lim_{T\to\infty} \int_{-\infty}^{\infty} \frac{1}{2T} \int_{-T}^{T} \left[\frac{\partial}{\partial x_i} \int_S G(r) W_i(\hat{\mathrm{y}}, \tau) d\hat{\mathrm{y}} \right] \\ &\quad \times \left[\frac{\partial}{\partial x_i'} \int_S G(r') W_l(\hat{\mathrm{y}}', \tau') d\hat{\mathrm{y}}' \right] dt\, e^{i\omega\varsigma}\, d\varsigma. \end{aligned} \tag{4.10}$$

Since $\hat{\mathbf{y}}$ and $\hat{\mathbf{y}}'$ are independent, we can define a separation parameter η in a cross correlation function of W_i

$$R_{W_{il}} = \lim_{T\to\infty} \frac{1}{2T} \int_{-T}^{T} W_i(\hat{\mathbf{y}}, t) W_l(\hat{\mathbf{y}}' + \eta, t + \varsigma) dt, \tag{4.11}$$

and we can further define the cross spectrum of W_i

$$\hat{\Phi}_{il}(\eta, \omega) = \int_{-\infty}^{\infty} R_{W_{il}}(\eta, \varsigma) e^{i\omega\varsigma} \, d\varsigma. \tag{4.12}$$

We also note that

$$\hat{\Phi}_{il}(\eta, \omega) = \int_{-\infty}^{\infty} \Phi_{il}(\omega, \mathbf{k}) e^{i\mathbf{k}\cdot\eta} \frac{d\mathbf{k}}{(2\pi)^2}. \tag{4.13}$$

Finally we can combine Eqs. (4.10)-(4.13) and after making some substitutions, find that

$$Q_D(\omega) = \int_{-\infty}^{\infty} \Phi_{il}(\omega, \mathbf{k}) H_i(\omega, \mathbf{k}, z) H_l^*(\omega, \mathbf{k}, z) \frac{d\mathbf{k}}{(2\pi)^2}, \tag{4.14}$$

where

$$H_i(\omega, \mathbf{k}, z) = \frac{e^{-i\mathbf{k}\cdot\hat{\mathbf{x}}}}{4\pi} \frac{\partial}{\partial x_i} \left(e^{-i\mathbf{k}\cdot\hat{\mathbf{x}}} \int_S e^{-i(\omega r/c + \mathbf{k}\cdot\hat{\mathbf{r}})} \frac{d\mathbf{y}}{r} \right). \tag{4.15}$$

This completes the first step in determining the source levels from surface orbital motion. We have the source level Q_D as an integral of the wavenumber-frequency spectrum of the orbital motions times the coupling factors $H_i H_l^*$. Cato has calculated H_i analytically for an infinite ocean radius, and the values can be calculated numerically for a finite ocean radius [4]. Cato provides a thorough discussion of the behavior of the coupling factors [4] and has shown the spatial dependence of the coupling factors to be

$$H_i \propto \exp\left\{ -i \left[\mathbf{k} \cdot \hat{\mathbf{x}} + z\sqrt{(\omega^2/c^2) - k^2} \right] \right\}. \tag{4.16}$$

One can see that the spatial dependence is entirely oscillatory in the horizontal direction, but is oscillatory in the vertical only for $k \leq \omega/c$. For $k > \omega/c$ the coupling factor magnitude has an exponential decay with depth. This will lead to an important approximation later in the development.

Cato has also provided a convenient form for the coupling factors in terms of dimensionless quantities $M = \omega/kc$, $X = x'\omega/c$, $X_0 = R\omega/c$ and $A = z\omega/c$:

$$\begin{aligned} H_1(\omega, \mathbf{k}, z) &= -i\cos\alpha\, H_0(\omega, \mathbf{k}, z)/M, \\ H_2(\omega, \mathbf{k}, z) &= -i\sin\alpha\, H_0(\omega, \mathbf{k}, z)/M, \\ H_3(\omega, \mathbf{k}, z) &= \frac{\partial}{\partial A} H_0(\omega, \mathbf{k}, z), \end{aligned} \tag{4.17}$$

where α is the angle between $\mathbf{k}$ and the y_1 axis, and H_0 is the monopole coupling factor

$$H_0(\omega, \mathbf{k}, z) = \frac{1}{2}\int_0^{X_0} \frac{X e^{-i\sqrt{X^2+A^2}}}{\sqrt{X^2+A^2}} J_0(X/M)\, dX, \tag{4.18}$$

J_0 being the Bessel function of the first kind, order zero.

We must now relate the frequency-wavenumber spectrum Φ_{il} to the surface wave height power spectrum Ω. We start by relating the spectrum of u_i to that of $\rho u_i u_j$. Cato has shown [12] that

$$\Phi_{ijlm}(\omega, \mathbf{k})/\rho^2 = \Psi_{il}(\omega, \mathbf{k}) * \Psi_{jm}(\omega, \mathbf{k}) + \Psi_{im}(\omega, \mathbf{k}) * \Psi_{ij}(\omega, \mathbf{k}), \tag{4.19}$$

where $*$ denotes convolution and $\Psi_{il}(\omega, \mathbf{k})$ is the power spectrum of u_i. We can expand one of these terms in polar coordinates, with σ being the gravity wave frequency, as

$$\begin{aligned} [\Phi_{ijlm}(\omega, k, \alpha)]_1 &= \rho^2 \int_{\kappa=0}^{\infty} \int_{\gamma=0}^{2\pi} \int_{\sigma=-\infty}^{\infty} \Psi_{il}(\sigma, \kappa, \gamma) \\ &\times \Psi_{jm}(\omega - \sigma, \kappa', \gamma') \frac{\kappa\, d\kappa\, d\gamma\, d\sigma}{(2\pi)^3}, \end{aligned} \tag{4.20}$$

where $\boldsymbol{\kappa}' = \mathbf{k} - \boldsymbol{\kappa}$, with γ, γ' being the angles $\boldsymbol{\kappa}$, $\boldsymbol{\kappa}'$ make with the y_1 axis. We can define $\sigma' = \omega - \sigma$, and can now identify σ and σ' as the frequencies and $\boldsymbol{\kappa}$ and $\boldsymbol{\kappa}'$ as the wavenumber vectors of the two interacting waves $u_i u_j$, and ω and $\mathbf{k}$ as the resulting acoustic frequency and wavenumber. We can relate the wavenumbers and angles by

$$\begin{aligned} k\cos\alpha &= \kappa\cos\gamma + \kappa'\cos\gamma', \\ k\sin\alpha &= \kappa\sin\gamma + \kappa'\sin\gamma'. \end{aligned} \tag{4.21}$$

Since σ and $\boldsymbol{\kappa}$ (and σ' and $\boldsymbol{\kappa}'$) are associated with the orbital motion of surface gravity waves, they are uniquely related by Eq. (4.4). This is not true for ω and **k**. We can, however, use the behavior of the coupling factors previously described to find approximations for ω and k in terms of σ and κ.

We will again follow Cato [12] in noting the exponential decay of the coupling factors as k exceeds ω/c, and we can choose a value β such that we will only consider a Fourier component to ensonify a region if $k \leq \beta\omega/c$. From Cato's examination of the coupling factors [4], we can choose $\beta = 5$ for a practical receiver depth. We can now write

$$-\beta\omega/c \leq |\mathbf{k}| \leq \beta\omega/c, \tag{4.22}$$

but $|\mathbf{k}| \geq |\boldsymbol{\kappa}| - |\boldsymbol{\kappa}'|$ so we may use the deep water dispersion relationship to write

$$-\beta\omega/c \leq \sigma^2/g - (\omega - \sigma)^2/g \leq \beta\omega/c, \tag{4.23}$$

or

$$|\omega - 2\sigma| \leq \beta g/c. \tag{4.24}$$

Thus, the acoustic frequency will be within 3% of twice the gravity wave frequency. We can say with reasonable accuracy that

$$\omega \simeq 2\sigma \simeq 2\sigma'. \tag{4.25}$$

We now have formally obtained the frequency doubling effect, where two gravity waves of the same frequency interact to generate an acoustic wave of twice that frequency. We can similarly show that $\kappa \simeq \kappa'$.

Next we define the two-dimensional wavenumber spectrum of u_i

$$\hat{\chi}_{il}(\kappa, \gamma) = \int_{-\infty}^{\infty} \Psi(\sigma, \kappa, \gamma)\,\frac{d\sigma}{2\pi}. \tag{4.26}$$

Since σ and κ are related, we can define $\hat{\sigma}$ as the specific value of σ determined by Eq. (4.4). Also, since k and ω are not variables in the convolution integral Eq. (4.20), $\kappa' = |\mathrm{k} - \kappa|$, and we have the two relations of Eq. (4.21), we can find κ and κ' in terms of γ. We will define the values of $\hat{\sigma}$ and κ thus determined as $\hat{\sigma}_\gamma$ and κ_γ. Now we will make the assumption that the two-dimensional wavenumber spectrum is separable into a one-dimensional spectrum times an angular spectrum,

$$\hat{\chi}_{il}(\kappa,\gamma) = 2\pi\chi_{il}(\kappa)G(\sigma,\gamma)/\kappa, \tag{4.27}$$

where the angular dependence satisfies

$$\int_0^{2\pi} G(\sigma,\gamma)\,d\gamma = 1. \tag{4.28}$$

After substituting Eqs.(4.26) and (4.27) into Eq. (4.20), making the variable substitutions mentioned above, and also substituting $d\kappa = (\partial\kappa/\partial\hat{\sigma})\,d\hat{\sigma}$, we note that we can eliminate two of the three integrals in the convolution. Then

$$\begin{aligned} [\Phi_{ijlm}(\omega,k,\alpha)]_1 &= 2\pi\rho^2 \int_{\gamma=0}^{2\pi} \chi_{il}(\kappa)\chi_{jm}(\kappa')G(\sigma,\gamma)G(\sigma',\gamma') \\ &\times \frac{1}{\kappa'_\gamma(\gamma')}\frac{\partial\kappa_\gamma}{\partial\hat{\sigma}_\gamma}d\gamma. \end{aligned} \tag{4.29}$$

We arrive at a similar expression for the second term on the left hand side of Eq. (4.19) by substituting subscripts. We can write the sound pressure spectrum as

$$\begin{aligned} Q_D(\omega) &= \int_{-\infty}^{\infty} 2\pi\rho^2 \int_{\gamma=0}^{2\pi} [\chi_{il}(\kappa)\chi_{jm}(\kappa') \\ &+ \chi_{im}(\kappa)\chi_{jl}(\kappa')]G(\sigma,\gamma)G(\sigma',\gamma') \\ &\times \frac{\partial\kappa_\gamma}{\partial\hat{\sigma}}\frac{d\gamma}{\kappa'}H_{ij}H^*_{lm}\frac{d\mathrm{k}}{(2\pi)^2}. \end{aligned} \tag{4.30}$$

Cato has shown that for significant ensonification of the noise field κ_γ, κ'_γ, and σ can vary by only a small proportion of their values, and thus can be regarded as constants in the integration. Also, $G(\sigma,\gamma)$ varies relatively slowly, and $\kappa \simeq \kappa'$, so we can substitute $G(\sigma,\gamma)G(\sigma,\gamma+\pi)$ for $G(\sigma,\gamma)G(\sigma',\gamma')$. We can differentiate Eq. (4.5) to find

$$\begin{aligned} \chi_{11} &= \cos^2\gamma \cdot \chi_{33}, \\ \chi_{22} &= \sin^2\gamma \cdot \chi_{33}, \\ \chi_{13} &= \cos\gamma \cdot \chi_{33}, \\ \chi_{23} &= \sin\gamma \cdot \chi_{33}. \end{aligned} \tag{4.31}$$

We further define the one-sided frequency spectrum of u_3 as $\hat{\Omega}(\sigma)$ and can write

$$\hat{\Omega}(\sigma) = \frac{\partial\kappa}{\partial\sigma}\chi_{33}(\kappa), \tag{4.32}$$

and since $u_3 = \partial\varsigma/\partial t$, we have the frequency spectrum of the wave height in terms of the wavenumber spectrum

$$\Omega(\sigma) = \frac{1}{\sigma^2}\frac{\partial\kappa}{\partial\sigma}\chi_{33}(\kappa). \tag{4.33}$$

We can now see that

$$\chi_{il}(\kappa) = g_{il}(\gamma)\Omega(\sigma)\frac{\partial\sigma}{\partial\kappa}\sigma^2\delta_{il}, \tag{4.34}$$

where g_{il} can be found from Eq. (4.31) and $g_{33} = 1$. We note that

$$g_{il}(\gamma)g_{33}(\gamma+\pi)\delta_{il} = g_{i3}(\gamma)g_{l3}(\gamma+\pi)\delta_{il}, \tag{4.35}$$

and so both terms of Eq. (4.30) are identical. We can then write the sound pressure in terms of $\Omega(\sigma)$,

$$Q_D(\omega) = 2\rho^2\frac{\hat{\sigma}^4}{\kappa'}\frac{\partial\hat{\sigma}}{\partial\kappa}\Omega^2(\hat{\sigma})I_{\alpha_{il}}(\hat{\sigma})\int_0^{k_0}\int_0^{2\pi} H_i H_l^* k\frac{d\alpha\, dk}{2\pi}\delta_{il}, \tag{4.36}$$

where

$$I_{\alpha_{il}}(\hat{\sigma}) = \int_0^{2\pi} g_{il}(\gamma)g_{33}(\gamma+\pi)G(\sigma,\gamma)G(\sigma,\gamma+\pi)\,d\gamma. \tag{4.37}$$

We can see that $I_{\alpha_{11}} + I_{\alpha_{22}} = I_{\alpha_{33}}$.

Next we separate out the α dependence of the H_i, perform the α integration of Eq. (4.36), and note that $H_1 = H_2$ to find

$$Q_D(\omega) = \rho^2 \frac{\hat{\sigma}^4}{\kappa'} \frac{\partial \hat{\sigma}}{\partial \kappa} \Omega^2(\hat{\sigma}) I_{\alpha_{33}}(\hat{\sigma}) \int_0^{k_0} \left(\hat{H}_1 \hat{H}_1{}^* + 2 \hat{H}_3 \hat{H}_3{}^* \right) k \, dk, \tag{4.38}$$

where $\hat{H}_i = \hat{H}_i(w, k, z)$. Finally, we use the dispersion relationship to substitute $\kappa' = \sigma'^2/g$, $\partial \hat{\sigma}/\kappa = g/(2\hat{\sigma})$, and we use Eq. (4.25) to substitute $\hat{\sigma} = \hat{\sigma}' = \omega/2$, and we have the result

$$Q_D(\omega) = \frac{\rho^2 g^2}{4} \omega \Omega^2(\omega/2) I_{\alpha_{33}}(\omega/2) \int_0^{k_0} (\hat{H}_1 \hat{H}_1^* + 2 \hat{H}_3 \hat{H}_3^*) k \, dk. \tag{4.39}$$

This gives us the received pressure for an infinite depth ocean in terms of known or measurable quantities. We can measure $\Omega(\sigma)$ directly or use an empirical spectrum based on wind speed. We can similarly measure or imply from the wind speed $G(\sigma, \gamma)$ and thus calculate $I_{\alpha_{33}}(\sigma)$. $\hat{H}_i \hat{H}_i^*$ can be calculated for a given geometry, and ρ and g are physical constants. We thus have an equation which will allow us to predict the noise spectral levels for a receiver in an infinitely deep ocean.

We must now turn to the problem of finding the noise levels in a more realistic ocean. We will consider the case of horizontally stratified media in the water column and in the bottom. Schmidt and Kuperman have shown that we can write the noise intensity generated by a horizontal distribution of homogeneous sources at depth z' as [23]

$$P(\omega, z, z') = q^2(\omega, z') T_m^2(\omega, z, z'), \tag{4.40}$$

where $q^2(\omega, z')$ is the acoustic monopole source strength of the distributed sources of order m, and we can call T_m^2 the bottom gain:

$$T_m^2(\omega, z, z') = \frac{8\pi m}{K^{2m}(z')} \int_0^\infty |g(k, z, z')| [K^2(z') - k^2] k \, dk. \tag{4.41}$$

In this equation $K(z) = \omega/c(z)$, and g is the depth-dependent Green's function satisfying

$$\frac{d^2 g}{dz^2} + [K^2(z) - k^2] g = -\frac{1}{2\pi} \delta(z - z'). \tag{4.42}$$

We can eliminate the depth dependence in $q(\omega, z')$ by normalizing the source strength to that produced by the same source distribution in an infinitely deep ocean, $Q(\omega)$, where to first order $q^2(\omega, z') = Q^2(\omega)/16\pi(z')^2$. Now, provided z' is chosen small enough compared to the wavelength, Eq. (4.40) is approximately independent of z', and we have only to find the equivalent monopole source strength and evaluate $T(\omega, z, z')$ to find $P(\omega, z)$. While the solution to Eq. (4.41) for an elastic bottom is not available analytically, there are numerical solutions available. We can easily relate $Q_D(\omega)$ to its equivalent monopole source strength by noting from Eq. (4.17) that

$$\begin{aligned} H_1 H_1^* + H_2 H_2^* &= H_0 H_0^* / M^2, \\ H_3 H_3^* &= \frac{\omega}{c} \frac{\partial}{\partial z} H_0 H_0^*. \end{aligned} \tag{4.43}$$

Thus the combined horizontal components are of vertical order $m = 1$ and the vertical component is of order $m = 2$. We can now write

$$\begin{aligned} P_D(\omega) &= \left[\frac{\rho^2 g^2}{8\pi} \omega \Omega^2(\omega/2) I_{\alpha_{33}}(\omega/2)\right] \times \left[T_1^2(\omega, z) \int_0^{k_0} H_0 H_0^* / M^2 k\, dk \right. \\ &+ \left. T_2^2(\omega, z) \int_0^{k_0} \frac{\omega}{c} H_0 H_0^* k\, dk\right], \end{aligned} \tag{4.44}$$

where the index on T indicates the order of the vertical model used in Eq. (4.41).

We now have the full solution to the received pressure spectrum in a horizontally stratified ocean. We will next look at the specific techniques and data used to generate predictions of the noise pressure spectrum.

Chapter 5

Prediction Techniques

5.1 SWADE data

The SWADE project (Surface Wave Dynamics Experiment) was an effort to characterize the sea surface using a variety of sensors and, at the same time, to measure other relevant environmental parameters [24]. The project included several pitch and roll surface buoys, satellite radar backscatter measurements, SWATH ship array deployments, and aircraft overflights. The long-term deployment of the pitch and roll buoys is the element of the experiment of direct use to us in our effort to predict noise generated by surface orbital motion.

SWADE and ECONOMEX instrument locations are shown in Fig. 1, and the overall experimental schematic is shown in Fig. 2. Deployment locations of SWADE instruments are listed in Table 5.1.

The buoys provided one complete set of measurements including a spectral

Instrument name	Type	Latitude	Longitude	Water depth
DISCUS E	Pitch and roll	$37^o\ 20.0'N$	$73^o\ 23.5'W$	2670m
DISCUS C	Pitch and roll	$37^o\ 32.1'N$	$74^o\ 23.5'W$	102m
DISCUS N	Pitch and roll	$38^o\ 22.1'N$	$73^o\ 38.9'W$	115m

Table 5.1: Relevant SWADE instrument summary.

estimate each hour, allowing us to update our estimate of the noise each hour. The spectral data from the SWADE buoys was provided for frequencies from 0.03 Hz to 0.34 Hz in 0.01 Hz bins, allowing acoustic predictions from 0.06 Hz to 0.68 Hz. The SWADE buoys which were closest to the ECONOMEX instruments were the Discus E and Discus C buoys. For predicting the noise at the deep ECONOMEX site, the data of Discus E was used, while predictions of noise at the three shallow ECONOMEX instruments were based on the data of Discus C. The SWADE project had deployed a SPAR buoy near the shallow ECONOMEX site with better angular resolution than the Discus buoys, but it sunk prior to the ECONOMEX deployments. We should consider here the possible effect of using a surface buoy moored in 95 meters of water (Discus C) on the predictions of noise at the 450 meter and 790 meter OBS's. We can note from the measured wave spectra that there is little energy below 0.1 Hz in the wave spectrum. If we calculate $\tanh(kd)$ for the worst case of 0.1 Hz with $d = 95$ m we find our dispersion relationship is in error by less than 1%. Thus we would expect no correction need be made to our wave spectra measured at Discus C.

Let us now consider the angular resolution available from pitch and roll measurements. Longuet-Higgins *et al.* [25] were the first to investigate the angular response of these buoys as follows. If the wavelengths of the surface motion are large with respect to the buoy diameter, the buoy tends to have the same motion and orientation as the surface. Then if we measure the vertical displacement and the two angles of pitch and roll, we will have three time series which represent the vertical displacement ς, and its spatial derivatives $\partial\varsigma/\partial x_1$ and $\partial\varsigma/\partial x_2$. Using the notation of the last chapter, we may represent the sea surface as a stochastic integral

$$\varsigma = \Re \int_S \exp(i(\kappa \cdot x - \sigma t))dS. \tag{5.1}$$

Then, since $\kappa = (\kappa \cos\gamma, \kappa \sin\gamma)$, we can write our three time series denoted by

ξ_1, ξ_2, ξ_3 as

$$\begin{aligned}
\xi_1 &= \Re \int_S \exp(i(\boldsymbol{\kappa} \cdot \boldsymbol{x} - \sigma t)) dS \\
\xi_2 &= \Re \int_S i\kappa \cos\gamma \exp(i(\boldsymbol{\kappa} \cdot \boldsymbol{x} - \sigma t)) dS \\
\xi_3 &= \Re \int_S i\kappa \sin\gamma \exp(i(\boldsymbol{\kappa} \cdot \boldsymbol{x} - \sigma t)) dS.
\end{aligned} \tag{5.2}$$

Next we can form co-spectra $C_{ij}(\sigma)$ and quadrature spectra $Q_{ij}(\sigma)$ from the time series ξ_i, ξ_j, and we find

$$\begin{aligned}
C_{11}(\sigma) &= \int_0^{2\pi} F(\sigma,\gamma)\, d\gamma, \\
C_{22}(\sigma) &= \int_0^{2\pi} \kappa^2 \cos^2\gamma F(\sigma,\gamma)\, d\gamma, \\
C_{33}(\sigma) &= \int_0^{2\pi} \kappa^2 \sin^2\gamma F(\sigma,\gamma)\, d\gamma, \\
C_{23}(\sigma) &= \int_0^{2\pi} \kappa^2 \cos\gamma \sin\gamma F(\sigma,\gamma)\, d\gamma, \\
Q_{12}(\sigma) &= \int_0^{2\pi} \kappa \cos\gamma F(\sigma,\gamma)\, d\gamma, \\
Q_{13}(\sigma) &= \int_0^{2\pi} \kappa \sin\gamma F(\sigma,\gamma)\, d\gamma,
\end{aligned} \tag{5.3}$$

where $F(\sigma,\gamma) = \Omega(\sigma) G(\sigma,\gamma)$ is the frequency-directional spectrum of the surface elevation. We can define the Fourier coefficients of $F(\sigma,\gamma)$ as

$$a_n(\sigma) + ib_n(\sigma) = \frac{1}{\pi} \int_0^{2\pi} e^{ni\gamma} F(\sigma,\gamma)\, d\gamma, \tag{5.4}$$

where

$$F(\sigma,\gamma) = \frac{1}{2} a_0 + \sum_{n=1}^{n=\infty} [a_n \cos(n\gamma) + b_n \sin(n\gamma)]. \tag{5.5}$$

We can see that the right hand sides of Eq. (5.3) are related to these Fourier coefficients as follows:

$$\begin{aligned}
a_0(\sigma) &= \frac{1}{\pi} C_{11}(\sigma), \\
a_1(\sigma) = \frac{1}{\pi k} Q_{12}(\sigma), \quad b_1(\sigma) &= \frac{1}{\pi k} Q_{13}(\sigma), \\
a_2(\sigma) = \frac{1}{\pi k^2} [C_{22}(\sigma) - C_{33}(\sigma)], \quad b_2(\sigma) &= \frac{2}{\pi k^2} C_{23}(\sigma).
\end{aligned} \tag{5.6}$$

The pitch and roll buoy then gives us the first five coefficients in the Fourier series describing the angular spectrum of the surface elevation at each of the frequencies for which we find the co-spectra and quadrature spectra of the time series. We must now use these five Fourier coefficients to find estimates of the frequency-directional spectra $\Omega(\sigma)$ and $G(\sigma,\gamma)$.

Our estimate of the wave power spectrum

$$\Omega(\sigma) = \int_0^{2\pi} F(\sigma,\gamma) = \pi a_0(\sigma) = C_{11}(\sigma), \tag{5.7}$$

is obvious from inspection of Eq. (5.5), as well as our definition of the co-spectra.

The best estimate of the directional spectrum is not as simple. An obvious choice would be to try the truncated sum

$$G(\sigma,\gamma) = \frac{1}{2\pi} + \frac{1}{\pi a_0}(a_1 \cos\gamma + b_1 \sin\gamma + a_2 \cos 2\gamma + b_2 \sin 2\gamma). \tag{5.8}$$

This sum is actually a convolution of the true directional spectrum with a weighting function, and considerable smoothing results in the estimated spectrum. Calculations of $I_{\alpha_{33}}$ made using this type of directional spectrum estimate from simulated directional spectra are typically in error by a factors of 10^3. Other weighted averages of the first five Fourier coefficients can be made, but they too produce a much smoothed estimate.

Several investigators have fit empirical curves to measured directional spectra. Longuet-Higgins has suggested the wave directional spectra fit the form [25]

$$G(\sigma,\gamma) \propto |\cos^{2s}(\gamma/2)| \tag{5.9}$$

where the spreading parameter s is a function of frequency and wind speed. Kibblewhite and Wu used an empirical relationship to find s based on the wind speed and frequency, and then calculated $I_{\alpha_{33}}$ analytically [3]. One could also match the measured first five Fourier coefficients to the first five Fourier coefficients of the empirical spectrum $\cos^{2s}\gamma/2$ to estimate the parameter s, as suggested by

Longuet-Higgins [25], and hence calculate $I_{\alpha_{33}}$. However, the data used to develop the empirical formula are generally taken under conditions of steady wind speed and direction. In our field data, the wind speed and direction can vary significantly, giving rise to wave fields with different directionality, and in general a broader directional spectrum than that predicted by the empirical formula. Therefore, we would expect predictions of $I_{\alpha_{33}}$ calculated from spectra derived from empirical formulas to be lower than the true value under variable meteorological conditions. In particular, if the true directional spectrum is bimodal (two peaks corresponding to two wave fields generated by winds in different directions) there can be significant energy in opposing wave directions $G(\gamma)G(\gamma+\pi)$ which is not predicted by the cosine power curve. Donelan *et al.* have suggested a better fit to the data is found in a $\text{sech}^2\beta\gamma$ distribution [26] with β being the spreading parameter, but estimates of $I_{\alpha_{33}}$ based on estimates of β are also too small.

Another approach would be to use a data adaptive spectral estimation technique such as the maximum likelihood method (MLM) or the maximum entropy method (MEM). The method used here to estimate the directional spectrum given the first five Fourier coefficients is the MEM. This method produces a spectal estimate which retains the first five Fourier coefficients and estimates the remaining coefficients based on the first five. We will follow Lygre and Krogstad [27] in developing an algorithm to make this estimate.

We will define a function with a Fourier series (suppressing the dependence on σ) on the interval $(-\pi, \pi)$ as

$$D(\gamma) = \frac{1}{2\pi} \sum_{n=-\infty}^{\infty} c_n^{in\gamma}, \; c_0 = 1, \; c_{-n} = c_n^*. \tag{5.10}$$

The entropy of D is defined by

$$H(D) = 1 \int_{-\pi}^{\pi} \log(D(\gamma))d\gamma, \tag{5.11}$$

and it has been shown by Burg [28] that the function maximizing $H(D)$ subject to the constraint that the coefficients c_n equal some known c_k for $k \leq N$ is

$$D(\gamma) = \frac{1}{2\pi} \frac{\theta_e^2}{|1 - \phi_1 e^{-i\gamma} - \cdots - \phi_N e^{-iN\gamma} D|^2}, \tag{5.12}$$

where $\phi_1 \cdots \phi_N$ and θ_e^2 are obtained from the Yule-Walker equations

$$\begin{bmatrix} 1 & c_1^* & \cdots & c_{N-1}^* \\ c_1 & \ddots & \ddots & \vdots \\ \vdots & \ddots & \ddots & c_1^* \\ c_{N-1} & \cdots & c_1 & 1 \end{bmatrix} \times \begin{bmatrix} \phi_1 \\ \vdots \\ \vdots \\ \phi_N \end{bmatrix} = \begin{bmatrix} c_1 \\ \vdots \\ \vdots \\ c_N \end{bmatrix}, \tag{5.13}$$

and

$$\theta_e^2 = 1 - \phi_1 c_1^* - \cdots - \phi_N c_N^*. \tag{5.14}$$

In our case we have $N = 2$ with $c_1 = (a_1 + ib_1)/a_0$ and $c_2 = (a_2 + ib_2)/a_0$. We can now solve this system of equations to find ϕ_n in terms of c_n:

$$\begin{aligned} \phi_1 &= (c_1 - c_2 c_1^*)/(1 - |c_1|^2), \\ \phi_2 &= c_2 - c_1 \phi_1, \end{aligned} \tag{5.15}$$

and finally we can substitute these into Eq. (5.12) to find our directional spectral estimate

$$D(\gamma) = \frac{1 - \phi_1 c_1^* - \phi_2 c_2^*}{2\pi |1 - \phi_1 e^{-i\gamma} - \phi_2 e^{2i\gamma}|^2}. \tag{5.16}$$

We now have an estimate of the angular distribution of the wave energy at each frequency which reproduces the first five Fourier coefficients which produced it, and uses these and the Yule-Walker equations to extrapolate the remaining coefficients. This technique has been shown by Lygre and Krogstad [27] to give a much more peaked distribution over the MLM technique, and to resolve a bimodal wavefield.

Figure 3 shows the estimated spectra from the various methods for a simulated bimodal spectral input, and Fig. 4 shows the estimates of directional spectra for the 0.16 Hz bin from Discus E on January 27 at 1200. This datum was chosen as illistrative because it occurs after a shift in wind direction, and one could expect the true spectrum to be bimodal. One can see for the estimates from the simulated data that the MEM estimate provides a better representation of the structure of the actual spectrum. One can also note in the comparison of actual data a bimodal structure is evident in the MEM estimate only.

5.2 Coupling factors and bottom gain

While the coupling factors $\int H_i H_i^* k\, dk$ can be evaluated analytically for an ocean of infinite radius, [4] they predict infinite noise when the horizontal components are considered. We can solve this by adding a relaxation mechanism and thereby attenuation in the water column, or we can use a finite effective radius with some physical basis such as the ocean basin radius, storm radius (if applicable), or such. The coupling factors must then be evaluated either approximately analytically or numerically. The attenuation due to absorption at the frequencies of interest is believed to be too small to limit the noise on ocean basin scales, and so we will assume an effective radius. Calculations show that at distant ranges the horizontal coupling factors vary roughly as $\sqrt{R}$, and thus doubling the effective radius has only a minor effect on the overall source strength $Q_D(\omega)$.

Based on the distance to shore of the ECONOMEX deployments and on transmission loss studies in this frequency range, an effective radius of 100 kilometers was chosen. The magnitude of the coupling factors was then calculated numerically for receiver depths of 450 meters and 2500 meters. These results are shown in Fig. 5.

The final step in making our predictions is the calculation of the bottom gain, T_m^2, for the horizontal and vertical components. The most computationally intensive part of this task is the calculation of the depth dependent Green's functions, $g(k, z, z')$, for which we use the fast field approach. The fast field approach can be generalized to a fully elastic elastic media, but requires that the wave equation be separable in depth, that is to say range-independent. We will use the fast field approach, that realizing errors that may ensue due to range dependent bathymetry and media.

The tool used to solve the full wave problem in this work is the SAFARI set of programs (Seismo-Acoustic Fast field Algorithm for Range Independent environments) developed by Schmidt and Jensen [13,14]. The basic solution technique in SAFARI is to represent the field in each of a series of homogeneous layers by the Hankel transforms of the unknown potentials satisfying the homogeneous wave equation. The boundary conditions at each layer interface yield a set of local equations involving the unknown potentials of the adjacent layers. These local equations are collected into a global matrix which can then be solved to yield all the unknown potentials simultaneously. Solutions are determined efficiently by implementing modern numerical techniques. An additional advantage relating to this work is the inclusion of the integration of Eq. (4.41) as an option in the code.

The environmental model used in SAFARI requires a number of parameters. The user must specify for each layer the compressional wave speed, shear wave speed, compressional and shear attenuations, and density. The uppermost and lowermost layers are taken to be semi-infinite half-spaces. Due to the long wavelengths involved at the very low frequencies of our predictions, the environmental model should be as accurate as possible fairly deep into the bottom. It is fortunate that compressional wave speed data from a deep seismic reflection study of the U.S. mid-Atlantic continental margin was made available prior to publication. The EDGE seismic experiment [15] involved recording seismic profiles to 16 seconds off the Virginia coast in the same region as the ECONOMEX and SWADE experiments. Using the compressional wave speed data, the figures and equations of Hamilton [29] and discussions with other investigators working in the area of geoacoustic modeling [30,31], geoacoustic models were developed for the bottom

layer	depth (m)	$C_p\,(m/s)$	$C_s\,(m/s)$	$\gamma_p\,(dB/\lambda)$	$\gamma_s\,(dB/\lambda)$	$\rho\,(g/cm^3)$
vacuum	*	0	0	0	0	0
fluid	0	1500	0	.015	0	1
elastic	2500	1756	200	.5	1	1.8
elastic	3165	2193	540	.3	.5	2.0
elastic	3678	2495	895	.1	.3	2.2
elastic	5011	2648	1314	.1	.3	2.4
elastic	5276	3817	1900	.1	.3	2.7
elastic	7231	4042	2011	.1	.3	2.8
elastic	8896	6380	3180	.05	.1	3.0

Table 5.2: Deep site environmental model. $C_{p,s}$ and $\gamma_{p,s}$ are compressional and shear wave speeds and attenuations, respectively; ρ is the density.

layer	depth (m)	$C_p\,(m/s)$	$C_s\,(m/s)$	$\gamma_p\,(dB/\lambda)$	$\gamma_s\,(dB/\lambda)$	$\rho\,(g/cm^3)$
vacuum	*	0	0	0	0	0
fluid	0	1500	0	.015	0	1
elastic	450	1799	200	.5	1	1.8
elastic	970	2174	540	.3	.5	2.0
elastic	1396	2683	895	.1	.3	2.2
elastic	2441	3441	1720	.1	.3	2.4
elastic	3332	4398	1739	.1	.3	2.5
elastic	4938	5872	2933	.1	.3	2.7
elastic	6582	6159	3059	.05	.1	2.9
elastic	8227	6380	3170	.05	.1	3.0

Table 5.3: Shallow site environmental model. $C_{p,s}$ and $\gamma_{p,s}$ are compressional and shear wave speeds and attenuations, respectively; ρ is the density.

at locations corresponding to water depths of 450 meters and 2500 meters. The models thus developed are given in tables 5.2 and 5.3. Depth profiles of compressional and shear wave speeds at the two sites are given in Fig. 6. SAFARI calculations of T_m^2 for both $m = 1$ and $m = 2$ for a receiver at 450 meters and 2500 meters are given in Fig. 7.

We can obtain a qualitative understanding of the relative importance of the different propagation mechanisms by looking at Fig. 8, contour plots of the magnitude of the wavenumber integrands plotted against the inverse of the phase speed, or “slowness” k/ω, and frequency. One can see for the deep site the normal modes play the predominant role in propagating the surface noise to the deep receiver, as only for the lowest frequencies do we get a contribution from waves with phase speeds less than 1500 m/s. In the shallow case there is a significant contribution at all the frequencies of interest from the lower phase speeds, indicating the importance of interface waves. These waves are propagating horizontally but suffer an exponential decay in the vertical, and thus they are excited only in the shallow case.

We can combine the effects of the coupling factors and the bottom gain, along with the constants in Eq. (4.44) to find the temporally invariant part of the solution, and we can write our prediction as the one-sided sound pressure spectrum level (dB *re* $1\mu Pa^2/Hz$)

$$SL(f) = 20 \log \Omega(f/2) + 10 \log I_{\alpha_{33}}(f) + 10 \log B(f), \tag{5.17}$$

where f is the acoustic frequency $f = \omega/(2\pi)$ and $B(f)$ is this time invariant part:

$$\begin{aligned} 10 \log B(f) = 197 \quad &+ \quad 10 \log \left[f \left(T_1^2(f) \int_0^{k_0} H_0 H_0^* / M^2 k \, dk \right.\right. \\ &+ \quad \left.\left. T_2^2(f) \int_0^{k_0} H_3 H_3^* k \, dk \right) \right] . \end{aligned} \tag{5.18}$$

The quantity $10 \log B(f)$ is shown in Fig. 9 for both the deep and shallow sites.

Chapter 6

Predictions for Receivers at 450 meters and 2500 meters

6.1 Variation of spectral level with frequency (spectral shape)

Since the wave height power spectrum appears in Eq. (4.19) as $\Omega^2(f/2)$, we might expect the shape of the acoustic spectrum to be related to the shape of the wave height spectrum at double the wave frequency, but we will see this shape is modified by a number of factors. The wave height spectrum generally shows a very steep rise to a spectral peak followed by a somewhat gentler ($\propto \sigma^{-4}$) slope at frequencies above the peak [26]. This peak frequency is generally characterized as being inversely proportional to wind speed, and thus is usually lower in frequency at higher wave heights. The peak tends to be quite narrow, normally occurring at frequencies of about 0.1 to 0.2 Hz, although in a newly developing wave field it can be higher. This tends to give rise to an acoustic spectrum with a peak in the 0.2 to 0.4 Hz range.

This overall shape will of course be modified by the effects of the directional spectrum, the coupling factors, and the bottom gain as functions of frequency. Effects of the coupling factors are easily seen in Fig. 5 and tend to emphasize the higher frequencies, which will tend to mitigate the slope of the peak in the acoustic spectrum at frequencies above the peak. The spectral slope of the coupling factors is $\propto \omega^2$. The bottom contribution to the spectral shape is more complicated, as seen in Fig. 7. In the shallow case, a peak in the bottom gain appears at about 0.18 Hz, which sharply drops to a low at about 0.28 Hz, and follows with a rise above 0.28 Hz with a slope of about ω^2. This will tend to flatten the acoustic spectrum if the peak in the wave spectrum occurs above 0.1 Hz (as it almost always does). The peak in the bottom gain at 0.18 Hz is normally well overcome by the sharp drop in the wave height spectrum at wave frequencies below 0.1 Hz. In the deep case, the peak in the bottom gain occurs at about 0.24 Hz, and is more likely to have an effect on the shape of the acoustic spectrum. In most cases, the frequency of this peak in the bottom gain falls slightly below twice the frequency in the wave height spectrum, thus serving to broaden the peak in the acoustic spectrum. Above 0.3 Hz the bottom gain is relatively flat in the deep case. Thus in the deep location the bottom will tend to enhance the peak in the acoustic spectrum, and at frequencies above the peak the down slope should be greater at the deep location than in the shallower case. When we look at the overall transfer function $B(f)$ shown in Fig. 9, we see for the shallow site a post peak slope of $\propto \omega^3$ and for the shallow case a slope of $\propto \omega^5$.

By far the greatest effect on the shape of the noise spectrum next to the wave height power spectrum is the behavior of $I_{\alpha_{33}}$. If one examines the behavior of the empirical models, it is clear that the value of the spreading parameters s or β vary such as to reduce the value of $I_{\alpha_{33}}$ at the frequency of the spectral peak. Mitsuyasu *et al.* [32] have proposed a model for frequencies above the spectral peak in which s varies as $s \propto (U/g\sigma)^{-2.5}$, where U is the wind speed. In Donelan's model, β is dependent on σ/σ_p only, with σ_p being the frequency at the peak [26].

Variation of $I_{\alpha_{33}}$ versus frequency for this model is shown in Fig. 10. One can see that for either of these empirical models the directional spectrum is narrower near the peak frequencies, and broader away from the peaks, and thus the spreading integral $I_{\alpha_{33}}$ will be a minimum near the peak. The effects of the wave height power spectrum and the spreading integral will oppose one another, and again tend to flatten the spectrum. We can see in Figs. 11- 26 the estimates of $10 \log P(f)$, $\Omega(\sigma/2\pi)$, $20 \log(\Omega(f/2))$, and $10 \log I_{\alpha_{33}}(f)$ for several illustrative examples for a 2500 m receiver, and in Figs. 27 - 30 the same quantities for a 450 m receiver. One can see from Figs. 11- 30 that the wave height power input can vary by as much as 60 dB in a given spectrum over the frequency range, whereas the spreading input varies over a much narrower range of up to 20 dB in a given spectrum. This will cause the wave height power spectrum to dominate, giving rise to a spectral peak, although one much diminished from the peak in the generating wave spectrum.

In summary we find the shape of the acoustic spectrum will in general resemble that of the generating wave spectrum in that their will be a sharp rise to a spectral peak, but in the acoustic spectrum the peak will be of a lower magnitude and broader than that present in the wave spectrum.

6.2 Variation of spectral level with wave height

The variation in the predicted noise with wave height will be the result of the combined effects of the wave height spectrum squared and the spreading integral. We saw in the last section that the two effects opposed one another, with the variation in the wave height spectrum dominating, giving rise to a spectral peak. When we look at predicted spectra from different times corresponding to different meteorological conditions, we find the variation in the wave height spectra is again greater than that of the spreading integral. We would thus predict an increase in noise level with an increase in overall wave height or sea state, with the increase in wave height again partially offset by the decrease in the spreading.

To allow us to see the effects of increasing wave height on our predictions, it is best to study a period of relatively constant wind direction with increasing wind speed and corresponding wave height. This will minimize the effects of other conditions which could effect the wave directional spectrum, such as wind direction versus fetch direction, sharp changes in wind direction, etc. We can see from Fig. 31 that we have such a time available to us at Discus E from 0300 to 1200 on January 21, 1991. During that time, wind speed rises from about 5 m/s to about 12 m/s with a rise in significant wave height of 0.25 m/s to 1.9 m/s. Some predicted noise spectra for this period are included as Figs. 11-14. One can see in the noise prediction at 0300 a peak forming at 0.6 Hz with a level of 121 dB. In subsequent predictions, this peak moves lower in frequency, to 0.45 Hz at 0600, 0.38 Hz at 0900 and finally 0.30 Hz at 1200. The peak level also increases from 121 dB to 125 dB, 130 dB, and finally 133 dB at 1200. It is interesting to note the wave height power at the peak for this period varies from -13 dB to 12 dB, a range of 25 dB, while the value of the spreading integral at the peak varies from -18 dB to -25 dB, for a range of -7 dB. This clearly shows the mitigating effect of the spreading integral in limiting the noise power at the peak under moderate conditions.

It is also interesting to consider the predictions in the case of severe weather conditions. The highest significant wave height recorded for which ECONOMEX data is available was 5.9 meters at Discus E in the late afternoon of March 4. Again the wind direction was relatively steady. The meteorological data for this period is shown in Fig. 32, and the noise predictions for 0400 to 1600 on that day are seen as Figs.15-21. The peak noise level prediction for this time is 155 dB, with a wave height input of 35 dB and a spreading integral value of -21 dB. Investigation of our MEM estimates of $I_{\alpha_{33}}$ shows that it reaches a minimum of about -25 dB at the peak frequency under conditions of moderate wave height ($\sim$ 3 meters), with no further decrease with increasing wave height above that level. This means our estimated directional distribution is not becoming increasingly narrow at wave heights above ~ 3m. This is in disagreement with the observed behavior of the directional spectra of wave height at high sea state [26]. We might, therefore, expect our predictions to overestimate the noise at high sea states. The increase in predicted noise level at wave heights above this threshold will be directly proportional to the increase in the wave height power squared.

At frequencies above the peak, the variation in wave height power with wave height is much less than that at the peak. One can see that the variation of the average wave height power on January 27 from 0300 to 1200 in the 0.5 Hz to 0.68 Hz was only from ~ -20 dB to ~ -15 dB. This is typical of most of the data analyzed in this frequency range. Even under the extreme conditions of March 4 the wave height power in this frequency range does not increase much above this level. Similarly the spreading input varies little in this range of frequencies for a steady wind direction, varying from ~ -5 dB to ~ 0 dB. We would therefore predict very little variation in the noise level in this frequency range for an increasing sea state.

6.3 Variation of spectral level with changing wind direction

One of the more interesting studies we can make involves examining the variation of noise level under conditions of constant wind speed but changing wind direction. A theory which proposes that wind turbulence is the direct cause of the acoustic noise would predict very little variation in noise levels under these conditions. Thus the predictions we make here may be useful in judging the actual contribution from the different mechanisms. Under our theory, we intuitively expect the noise to increase from the increased spread in the directional spectrum as the new wave field is developed, but we also realize the original wave field is diminishing, due to the loss of wind forcing and the combined effects of dissipation and non-linear interactions with the newly developing wave field.

We can see these combined effects in the data from Discus E in the early hours of February 23, 1991. As we can see in Fig. 33 the wind direction veers sharply by about 60 degrees at 0200 while the wind speed stays relatively constant at 8 to 11 m/s. The response in the predicted noise spectra is shown in Figs. 22-26. One can see the noise prediction at the peak is fairly constant at about 135 dB from 0200 through 0400, then begins to rise until it reaches 140 dB at 0600. The wave height power input during this period actually drops from 15 dB to 8 dB at 0400, and it rises back to about 15 dB at 0600. The spreading input at the peak increases from about -23 dB at 0200 to -17 dB at 0400, and then remains at about this value through 0600. Thus the increase in predicted noise is due to the increased spread in the directional spectrum, not an increase in wave height. Another effect of the wind shift on the predicted acoustic spectrum is that the peak tends to broaden. This is seen most clearly at 0400 in Fig. 24, when the peak in the developing wave field and the peak in the pre-existing wave field are both of similar magnitudes but different frequencies. This behavior is typical of the wind shifts analyzed.

6.4 Variation of spectral level with receiver depth

The variation in predicted spectral levels with receiver depth can be attributed to three factors. First, for a receiver in very shallow water, the gravity wave dispersion relationship will begin to depart from Eq. (4.4) and the bottom will begin to have an effect on the wave height spectrum. For our receivers at 2500 m and 450 m, this is not the case. The two remaining factors, the coupling factor differences and the bottom gain differences, will cause variation in our expected noise levels at these two depths.

Referring to Fig. 5, we can see that the difference in the coupling factor gain between the two locations varies from about 15 dB at 0.06 hz to about 7 dB at 0.68 Hz, with the shallow site having the higher value. The bottom gain is again more complicated, with the shallow bottom gain being higher at frequencies less than 0.2 Hz and greater than 0.5 Hz, and the deep bottom gain being higher between about 0.2 Hz and 0.4 Hz. The combined effects are visible in Fig. 9, where we can see the differences in the energetic part of the spectrum are quite minimal. Given the same wave height directional spectrum input, we expect the deep case to yield higher noise levels of about 6 dB at 0.25 Hz, and we expect the shallow case to yield higher noise levels of about 5 dB at 0.68 Hz. Due to the limited amount of data analyzed and the variance of the estimated spectra, it is difficult to see this variation in the predicted spectra between the two depths. We will therefore not try to judge the success of the predictions in this area.

Chapter 7

Experimental Noise Measurements

7.1 Experimental description

ECONOMEX (Environmentally Controlled Oceanfloor Noise Monitoring Experiment) [10] was designed to provide a long-term, high quality seismo-acoustic noise data set which could be coupled to the surface wave and meteorological data of the SWADE experiment. The instrumentation consisted of six Office of Naval Research (ONR) ocean bottom seismometers (OBS's) and two, one vertical and one horizontal, 75 meter six element hydrophone arrays. The instruments were off the Virginia coast in January 1991, recovered in February 1991 for maintenance , and redeployed from February through early April 1991. Precise instrument locations and deployment dates are listed in table 7.1.

The ONR OBS instruments deployed consisted of a three-component geophone for measuring ground motion in the 0.07 to 80 Hz range, a Cox-Webb differential pressure gauge (DPG) for measuring long period pressure signals in the water column, and in the original deployment, an OAS hydrophone [34]. In the later deployment, these hydrophones were removed to improve instrument reliability.

Instrument	Lat. (N)	Lon. (W)	Depth	Deployment dates
Vert. array	37° 24.7′	73° 26.8′	2573m	Jan 25-Feb 6; Feb 22-Apr 5
Hor. array	37° 24.7′	73° 26.8′	2573m	Jan 25-Feb 6; Feb 22-Apr 5
OBS 56	37° 24.7′	73° 26.8′	2548m	Jan 25-Feb 6; Feb 22-Apr 5
OBS 58	37° 26.4′	73° 31.4′	2417m	Jan 24-Feb 7; Feb 22-Apr 5
OBS 61	37° 23.8′	73° 24.4′	2600m	Jan 25-Feb 6; Feb 21-Apr 4
OBS 62	37° 33.2′	74° 14.1′	769m	Jan 11-Feb 6; Feb 22-Apr 5
OBS 63	37° 34.1′	74° 16.5′	443m	Jan 10-Feb 6; Feb 22-Apr 5
OBS 51	37° 35.9′	74° 21.3′	95m	Jan 10-Feb 6; Feb 22-Apr 5

Table 7.1: ECONOMEX instrument summary. Positions and depths listed are for the second leg of the experiment; those for the first leg differ only slightly. Also note OBS frames 61 and 62 exchanged positions between the first and second legs, although the instruments on them were exchanged also such that the instruments remained deployed in the same locations.

The sensors were connected via preamplifiers to an acquisition package consisting of a pre-whitening and anti-aliasing filter, a gain-ranging amplifier to improve dynamic range, and an analog to digital converter. The combined filter response is shown in Fig. 34. The acquisition package fed a recording package consisting of a RAM buffer and an optical disc recording system capable of storing 400 megabytes of data. The typical OBS's were programmed for continuous 8 Hz recording, with the anti-aliasing filter set to 2 Hz; however OBS 56 was set to record at 128 Hz with its anti-aliasing filter set to 40 Hz.

The 75 meter horizontal and vertical arrays each consisted of six OAS hydrophones at 15 meter separation. The hydrophone signals were preamplified by a low-noise, wide-range preamplifier and sent to acquisition and recording packages identical to those of the OBS's, with 128 Hz sampling and the anti-aliasing filter set to 40 Hz. In the second deployment the bottom three hydrophones of the vertical array were not included due to a cable malfunction. The array cable jacket included loose ended fiber strands to reduce strumming noise.

7.2 Data selection and processing

Following instrument recovery, the ECONOMEX data were transcribed from the optical disc to magnetic tape. While the data has not yet been transcribed from the binary machine format to a standard format for further dissemination, it is possible to read the binary format and produce ASCII files for limited time periods. The present work has concentrated on using the differential pressure gauge (DPG) data at the 8 Hz sampling rate to minimize the data processing involved while still adequately sampling the frequency band of interest. The DPG data were used instead of the geophone data because of current uncertainties in the geophone response. Since the model developed is only valid for receivers at depths greater than 400 meters, it was decided to analyze selected data from one deep DPG (OBS 58 at 2417 m) and the 450 m DPG (OBS 63). This allowed the maximum depth variation comparison given the instrument deployment depths.

Estimated spectra were generated by removing the mean and any linear trend from 64 second segments of the time series, and then averaging 512 point fast Fourier transforms of 34 minute sections of data using a Hanning window. The response of the pre-whitening and anti-aliasing filter was then removed. The bandwidth of 64 seconds results in a frequency resolution of 0.0156 Hz, which is consistent with the spectral resolution of our predictions, which is 0.02 Hz. An example of a full spectral range observation in shown in Fig. 35. Since the predictions are limited to a 0.06 to 0.68 Hz band, further observed spectra shown in this work are limited to the same band for clarity. For the most part, data were analyzed which corresponded to the same time periods for which predictions were made in Chap. 6.

7.3 Observed results and comparison with predictions

7.3.1 Spectral shape and overall spectral noise levels

In general, there is good overall agreement between the predicted spectral levels at most frequencies in the band of interest. Fig. 36 shows an example of one such case at the 2500 meter site, and Fig. 37 shows similar results at the 450 meter site. While the levels at a given frequency may differ between predicted and observed by up to 5 dB, there is an overall correspondence between the two. It is interesting to note in many of the comparisons between observed and predicted spectra that small peaks exist in the observed levels which are present in the predictions at the same frequenies but with differnt magnitudes. These two figures represent examples of the best agreement between predicted and observed spectra.

More typical of the level of agreement are Figs. 38-43, where we can see close agreement at frequencies around the spectral peak, but differences away from the peak of up to 7 dB in the deep case, and up to 17 dB in the shallow case. Here the overall shape is correctly predicted, but the peak is broader or narrower in the observed spectra, giving rise to large differences in the high slope region. In the predictions from the shallow site, there is a tendency to predict levels that are too high in the band 0.1 Hz to 0.2 Hz. Since this band corresponds to the peak in the bottom response in the shallow case, errors in the bottom model may account for this difference.

7.3.2 Variation with wave height

The observations show an increase in noise level with wave height, with good agreement between observations and predictions at moderate (~1-3 meters) wave heights, as seen in Figs. 39-43. At very low predicted noise levels, which correspond to times of low wave height, there is a disparity between predictions and observations. An example of this is the developing wave field of the early hours of January 27 at Discus E. As one can see in Figs. 44- 46, the agreement is good at frequencies corresponding to the peak in the predictions as the wave field develops, but the low levels predicted away from the peak are not confirmed by observation. By 1200 the wave field is developed, and Fig. 39 shows the good agreement between the prediction and observation at this time. A possible cause of the error in the predictions at low wave heights is the assumption of spatial homogeneity of the source wave field. Under very low local wave height conditions, it is possible for a much stronger wave field at some distance to dominate the noise field, thus making the predictions made from the local wave field very much in error. Another possible cause of the differences under low wave height conditions is the existence of another source mechanism generating acoustic energy, whose noise is normally dominated by that caused by orbital motion. Under low source strength conditions for the orbital motion noise, this assumed source may now dominate, giving rise to the errors noted above. The predictions in general are in reasonably close agreement when measured significant wave height is above ∼ 1 meter. For the period of the ECONOMEX data, roughly 77 percent of the wave height measurements are above this threshold.

We can see from the data of March 4, as seen in Fig. 47-50, the predictions again begin to deviate at very high wave height conditions which correspond to strong winds at relatively constant direction, with the predictions being higher than the observations. The disagreement at frequencies corresponding to the peak is up to 10 dB under these conditions. There is, however, the same general trend in the observed noise data as exists in the predictions, that of higher levels at higher wave heights and wind speeds. This would tend to indicate the wave directional spectral estimate provided by the MEM technique is overestimating the spread at these high wave heights. The empirical models, which are based on strong, steady winds, predict less spreading under these conditions than do the MEM estimates. Thus, under these conditions, the empirical model estimate for the spreading may be more accurate. The observations match the predictions fairly well in the region of frequencies above the peak under high wave height conditions.

7.3.3 Variation with changes in wind direction

The predictions agree quite well with the observed data under conditions of changing wind direction. We can again consider the wind shift of February 23 at 0200, depicted in Fig. 33, as typical. The observed and predicted noise levels for subsequent times are shown in Figs. 51- 55. The observed noise spectrum changes with time roughly as the predicted spectrum does. Of particular note is the broad peak in the observed spectrum at 0400, and the higher levels seen at the peak from 0500-0700.

It is also interesting to note the predictions and observations during a time of highly variable conditions such as those of the afternoon of January 27, again depicted in Fig. 31. The observations and predictions are seen in Figs. 36,56,57. Again we see relatively close agreement between predictions and observations, with the increased spreading adding to the noise as the wave height diminishes to keep the overall noise level fairly constant.

Chapter 8

Conclusions and Recommendations for Future Research

8.1 Conclusions

The most important conclusion one can draw from this work is the apparent importance of the orbital motion contribution to the total noise level in the frequency band 0.1 to 0.7 Hz. The close correspondence between the predicted and observed spectra under a wide range of conditions is strong evidence that the true noise generation mechanisms in this band are dominated by the interaction of opposing surface gravity waves. The fact that the predictions hold under the conditions of changing wind direction but constant wind speed would tend to negate the importance of the direct input of the wind turbulence on the sea surface as an important sound generation mechanism under most conditions. There is a possibility that some other source mechanism or mechanisms contribute significantly to the noise spectrum in this band under conditions of low wave height.

The second conclusion one may draw from this work is the importance of the measured directional spectrum in determining the overall noise level. Any model based on empirical relationships using wind speed as their input would have to also include the growth and decay of the wave field based on changing wind direction. The models which predict directional wave spectra from a knowledge of wind speed alone would be doomed to failure in the general case due to their assumption of a fully developed wave field and the changing nature of the true wave field.

Another important point brought out by this work is the importance of the propagation mechanisms in determining the overall levels and shape of the acoustic noise spectrum in this frequency band, which is consistant with the work of Schmidt and Kuperman [23]. It is imperative that one take into account the propagation if one wishes to compare source levels between two different locations. Otherwise differences in the bottom contribution could cloud important correlations or lead to incorrect conclusions. A key element in research of this type is the geoacoustic bottom model, and the availability of measured wave speeds deep into the bottom in the present work was extremely fortunate.

8.2 Recommendations for future research

As the predictions of acoustic noise depend so critically on the angular spread of the wave energy, a fruitful line of investigation would be to obtain directional wave height spectra of greater angular resolution in future experiments. It is unfortunate that the Spar buoy, the sensor with the greatest directional capability in the SWADE project, was lost prior to the ECONOMEX deployments. The increased directional resolution could have been used not only in estimating spectra at the location of the buoy, but also could have helped in determining the error in the estimate of the directional spectra made when we use the MEM technique at other locations. In lieu of higher resolution directional wave spectra, an attempt could be made to use some of the other SWADE data, such as directional spectral estimates made by shipborne arrays or radar backscatter, to improve the estimates from the pitch and roll buoys.

Another investigation which should provide interesting results would be the correlation of large amounts of the ECONOMEX data with the various SWADE parameters such as wind speed and wave height, and perhaps to automate the generation of acoustic predictions from the SWADE directional spectra. The present research only scratched the surface of the data available from this long term experiment. It would be useful to find the amount of long term agreement, and even more interesting to find other periods of disagreement between the predictions made with the model developed herein and ECONOMEX observations.

The final recommendation for research in this area would be the investigation of the range dependent aspects of the problem. There is range dependence in the both the source mechanism and the propagation mechanisms, which perhaps gives rise to some of the disagreement between our predictions and observations. The shallow site, in particular, would benefit from a consideration of its range dependent bathymetry. Buckingham [33] has found the noise in a wedged-shaped ocean with pressure-release boundaries to closely approximate the noise field in the range independent case, but further work is needed to extend his work to a more general bottom. As well, the investigation of the spatial variation of the wave height spectrum should prove feasible once the entire SWADE project data is collected and correlated. This could then be used to more accurately predict the noise at the ECONOMEX sites.

Bibliography

[1] M. S. Longuet-Higgins, "A theory of the origin of microseisms," Philos. Trans. R. Soc. London Ser. A **243**, 1-35 (1950).

[2] L. M. Brekhovskikh, "Underwater sound waves generated by surface waves in the ocean," izv. Atmos. Ocean Phys. **2**, 582-587 (1966).

[3] A. C. Kibblewhite and C. Y. Wu, "The generation of infrasonic ambient noise in the ocean by nonlinear interactions of ocean surface waves," J. Acoust. Soc. Am. **85**, 1935-1945 (1989).

[4] D. H. Cato, "Sound generation in the vicinity of the sea surface: source mechanisms and the coupling to the received sound field," J. Acoust. Soc. Am. **89**, 1076-1095 (1991).

[5] Y. P. Guo, "Waves induced by sources near the ocean surface," J. Fluid Mech. **181**, 293-310 (1987).

[6] R. H. Nichols, "Infrasonic ambient ocean noise measurements: Eleuthera," J. Acoust. Soc. Am. **69**, 974-981 (1981).

[7] T. E. Tapley and R. D. Worley, "Infrasonic ambient noise measurements in deep Atlantic water," J. Acoust. Soc. Am. **75**, 621-622 (1984).

[8] R. G. Adair, J. A. Orcutt, and T. H. Jordan "Low-frequency noise observations in the deep ocean," J. Acoust. Soc. Am. **80**, 633-645 (1986).

[9] G. H. Sutton and N. Barstow, "Ocean-bottom ultralow-frequency (ULF) seismo-acoustic ambient noise: 0.002 to 0.4 Hz," J. Acoust. Soc. Am. **87**, 2005-2011 (1990).

[10] G. M. Purdy and G. V. Frisk, "A long term experiment to monitor low frequency noise across the east coast of the U.S.," Woods Hole Oceanographic Institution, Proposal No. 6000.32R, Woods Hole, MA (Nov. 29, 1989).

[11] J. A. Orcutt, "Sources of ambient microseismic oceanic noise (SAMSON)," Scripps Institution of Oceanography, USDC Proposal No. 89-1471, La Jolla, CA (May 17, 1989).

[12] D. H. Cato, "Theoretical and measured underwater noise from surface wave orbital motion," J. Acoust. Soc. Am. **89**, 1096-1112 (1991).

[13] H. Schmidt, *SAFARI: Seismo-Acoustic Fast Field Algorithm for Range Independent Environments. User's Guide* SACLANT ASW Research Center, La Spezia, Italy SR 113 (1987).

[14] H. Schmidt and F. B. Jensen, " A full wave solution for propagation in multilayered viscoelastic media with application to Gaussian beam reflection at fluid-solid interfaces," J. Acoust. Soc. Am. **77**, 813-825 (1985).

[15] R. E. Sheridan, D. L. Musser, L. Glover III, M. Talwani, J. Ewing, S. Holbrook, G. M. Purdy, R. Hawman, and S. Smithson, "EDGE deep seismic reflection study of the U.S. mid-Atlantic continental margin," Am. Geophys. Union **72**, EOS, Transactions, Spring Meeting, 273-274 (1991).

[16] M. J. Lighthill, "On sound generated aerodynamically: I. General theory," Proc. of the R. Soc. **A211**, 564-578 (1952).

[17] Lord Rayleigh, *Theory of Sound* (Dover Publications, New York, second edition, 1945 reissue) (1877).

[18] P. E. Doak, "Analysis of internally generated sound in continuous materials: 2. A critical review of the conceptual adequacy and physical scope of existing theories of aerodynamic noise, with special reference to supersonic jet noise," J. Sound Vib. **25**, 263-335. (1972).

[19] J. A. Stratton, *Electromagnetic Theory*, McGraw-Hill, New York (1941).

[20] N. Curle, " The influence of solid boundaries upon aerodynamic sound," Proc. R. Soc. of London Series A **231**, 505-514 (1955).

[21] G. K. Bachelor, *An Introduction to Fluid Dynamics*, Cambridge University Press, Cambridge (1970).

[22] O. M. Phillips *The Dynamics of the Upper Ocean,* Cambridge University Press, London, (1966).

[23] H. Schmidt and W. A. Kuperman, " Estimation of surface noise source level from low-frequency seismoacoustic ambient noise measurements," J. Acoust. Soc. Am. **84**, 2153-2162 (1988).

[24] R. A. Weller, M. A. Donelan, M. G. Briscoe, and N. E. Huang, "Riding the crest: a tale of two experiments," Bull. Am. Meteor. Soc. **72**,163-183 (1991).

[25] M. S. Longuet-Higgins, D. E. Cartwright, and N. D. Smith, "Observations of the directional spectrum of sea waves using the motions of a floating buoy," *Ocean Wave Spectra* Prentice-Hall, Englewood Cliffs, New Jersey (1963).

[26] M. A. Donelan, J. Hamilton, and W. H. Hui, "Directional spectra of wind-generated waves," Trans. R. Soc. London Ser. A **315**, 509-562 (1985).

[27] A. Lygre and H. E. Krogstad, "Maximum entropy estimation of the directional distribution in ocean wave spectra," J. Phys. Oceanogr. **16**, 2052-2060 (1986).

[28] J. P. Burg, "Maximum entropy spectral analysis" Ph.D. dissertation Stanford University (1976).

[29] E. L. Hamilton, "Geoacoustic modeling of the sea floor," J. Acoust. Soc. Am. **68**, 1313-1340 (1980).

[30] S. Holbrook, Private communication, (1991).

[31] J. Ewing, Private communication, (1991).

[32] H. Mitsuyasu, F. Tasai, T. Suhara, S. Mizuno, M. Ohkuso, T. Honda, and K. Rikiisi, "Observations of the directional spectrum of ocean waves using a cloverleaf buoy," J. Phys. Oceanog. **5**, 750-760 (1975).

[33] M. J. Buckingham, "A theoretical model of surface-generated noise in a wedge-shaped ocean with pressure-release boundaries," J. Acoust. Soc. Am. **78**, 143-148 (1985).

[34] G. M. Purdy, L. Dorman, A. Schultz, and S. C. Solomon, "An ocean bottom seismometer for the Office of Naval Research," in *ULF/VLF (0.001 to 50 Hz) Seismo-Acoustic Noise in the Ocean, Proceedings of a workshop at the Institute for Geophysics, University of Texas, Austin, November 29 to December 1, 1988*, edited by G. H. Sutton (1990).

[35] R. T. Lacoss, "Data adaptive spectral analysis methods," Geophysics **36**, 661-675 (1971).

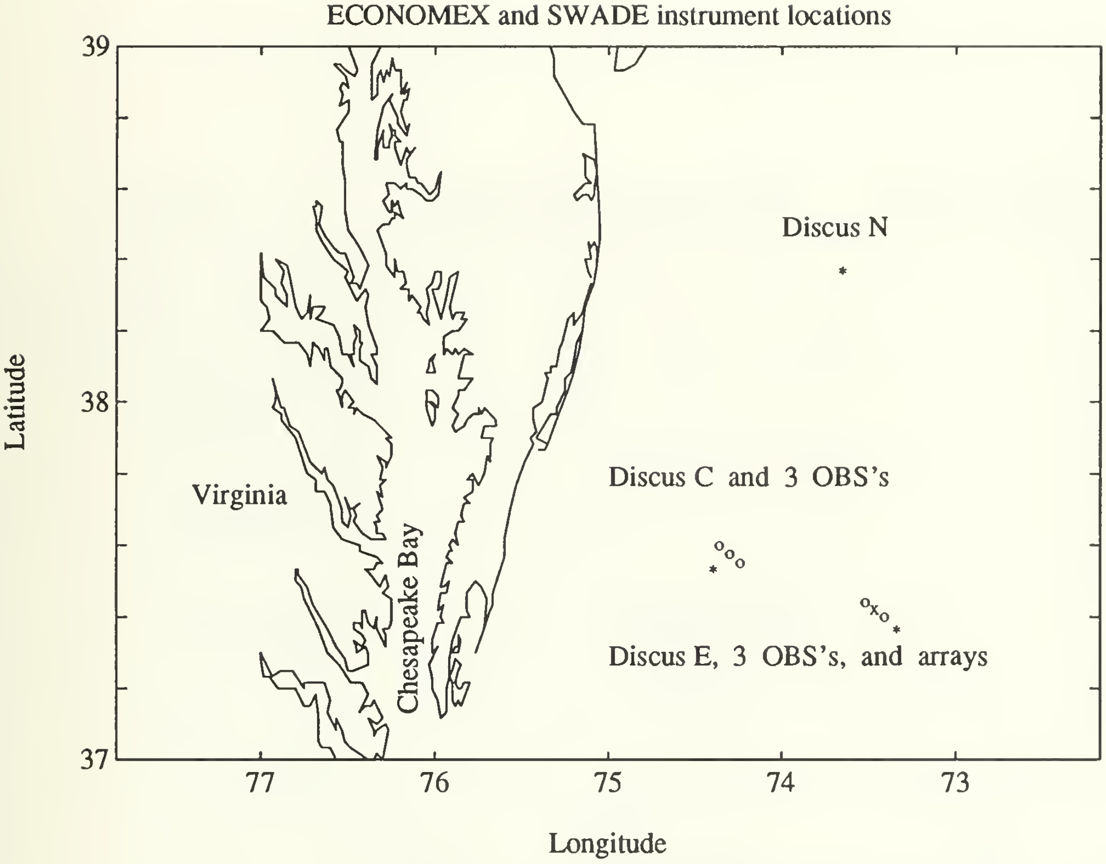
ECONOMEX and SWADE instrument locations
39
38
37
Latitude
Virginia
Chesapeake Bay
Discus N
Discus C and 3 OBS's
Discus E, 3 OBS's, and arrays
77
76
75
74
73
Longitude

Figure 1: Approximate locations of the ECONOMEX and relevant SWADE instruments. “*” denotes pitch and roll buoy location, “x” denotes location of one ONR OBS and two hydrophone arrays, and “o” denotes the location of one ONR OBS.

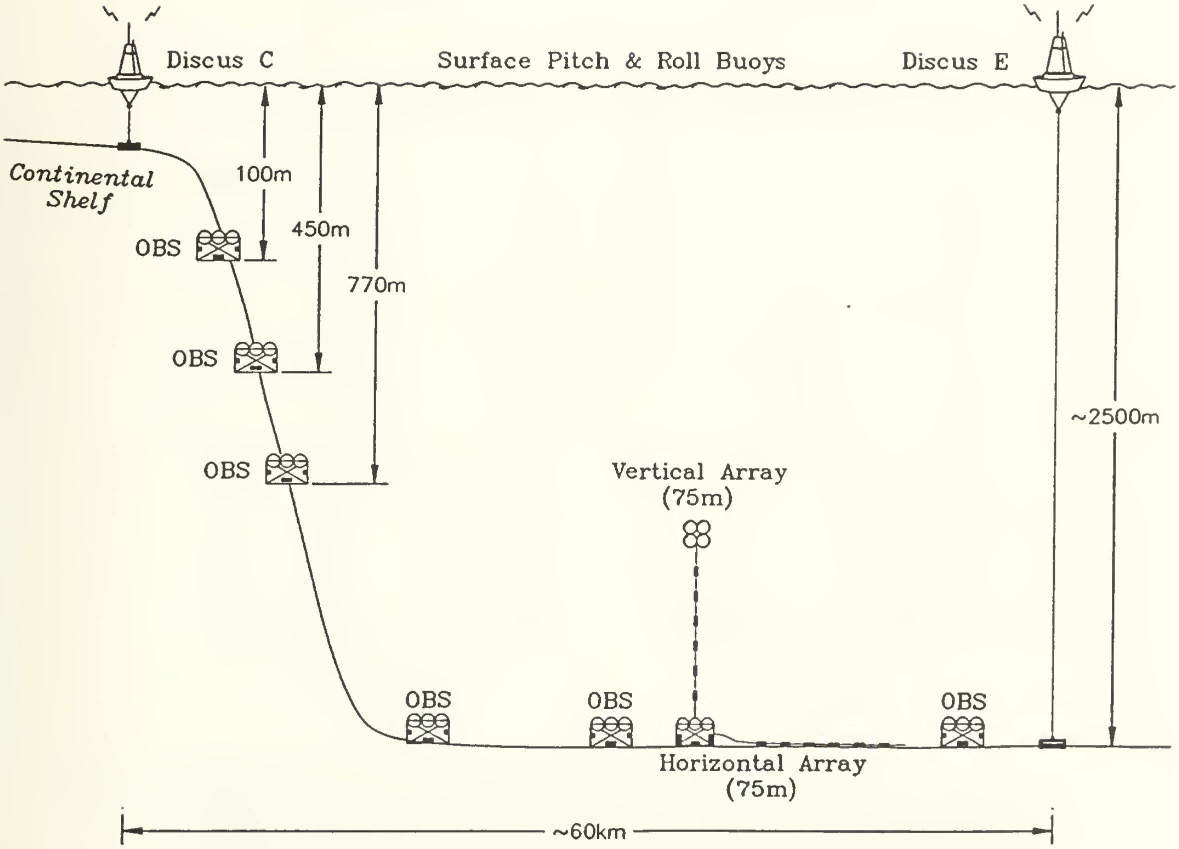
Discus C
Surface Pitch & Roll Buoys
Discus E
Continental Shelf
100m
450m
770m
OBS
OBS
OBS
Vertical Array (75m)
~2500m
OBS
OBS
OBS
Horizontal Array (75m)
~60km

Figure 2: Schematic arrangement of ECONOMEX and SWADE deployments.

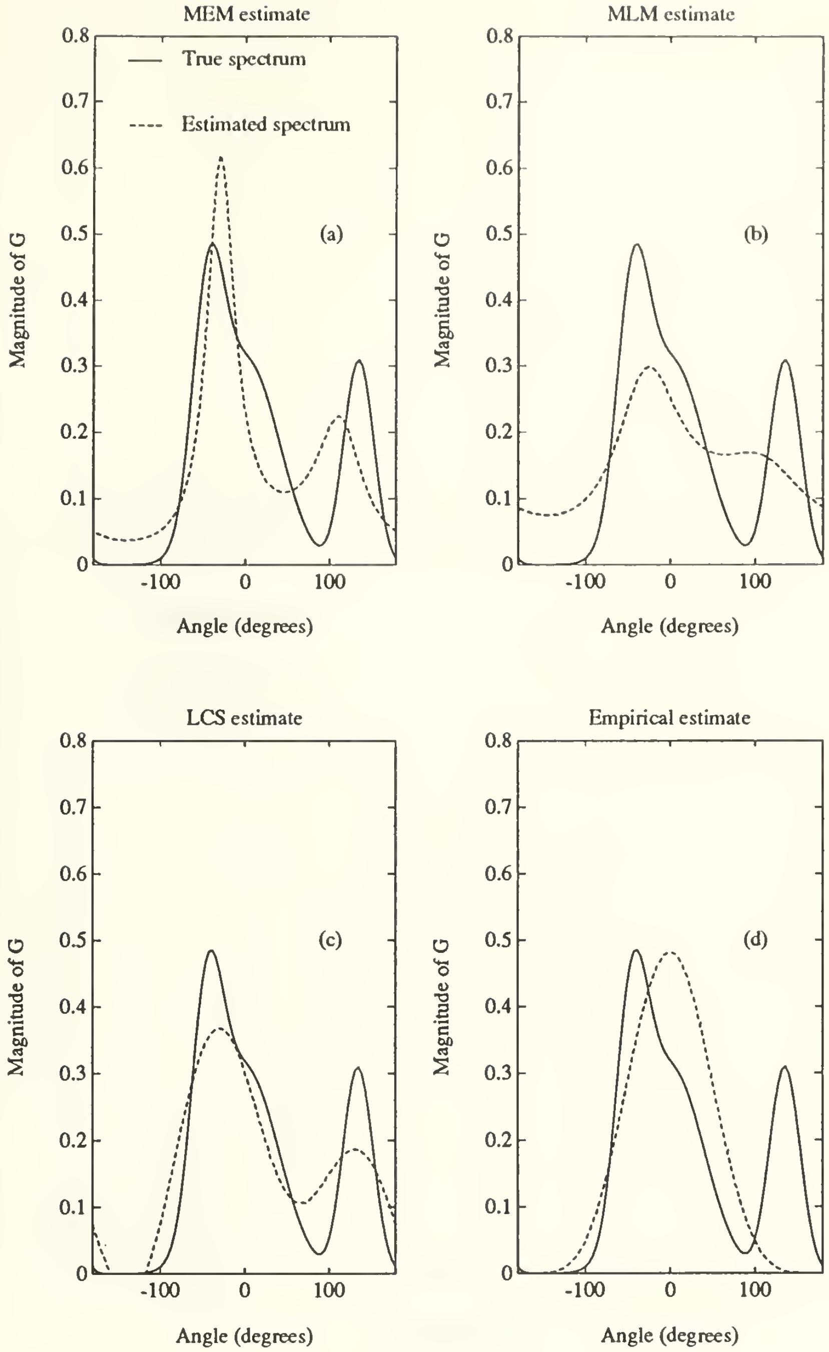

Figure 3: Estimates of the directional spectrum of $G(\gamma) = N(\cos^8(\gamma/2)+\cos^{10}(\gamma/2+\pi/4))$, where γ is the azimuthal angle, and N is chosen to normalize the spectrum. The MEM estimate was made using the Lygre-Krogstad algorithm mentioned in the text. The MLM estimate was made using an algorithm by Lacoss [35]. The LCS estimate refers to the weighted average of the first five Fourier coefficients suggested by Longuet-Higgins *et al.* [25] The empirical estimate was made by estimating the parameter s from the first five Fourier coefficients and using the empirical formula $G(\gamma) = N\cos^{2s}(\gamma/2)$.

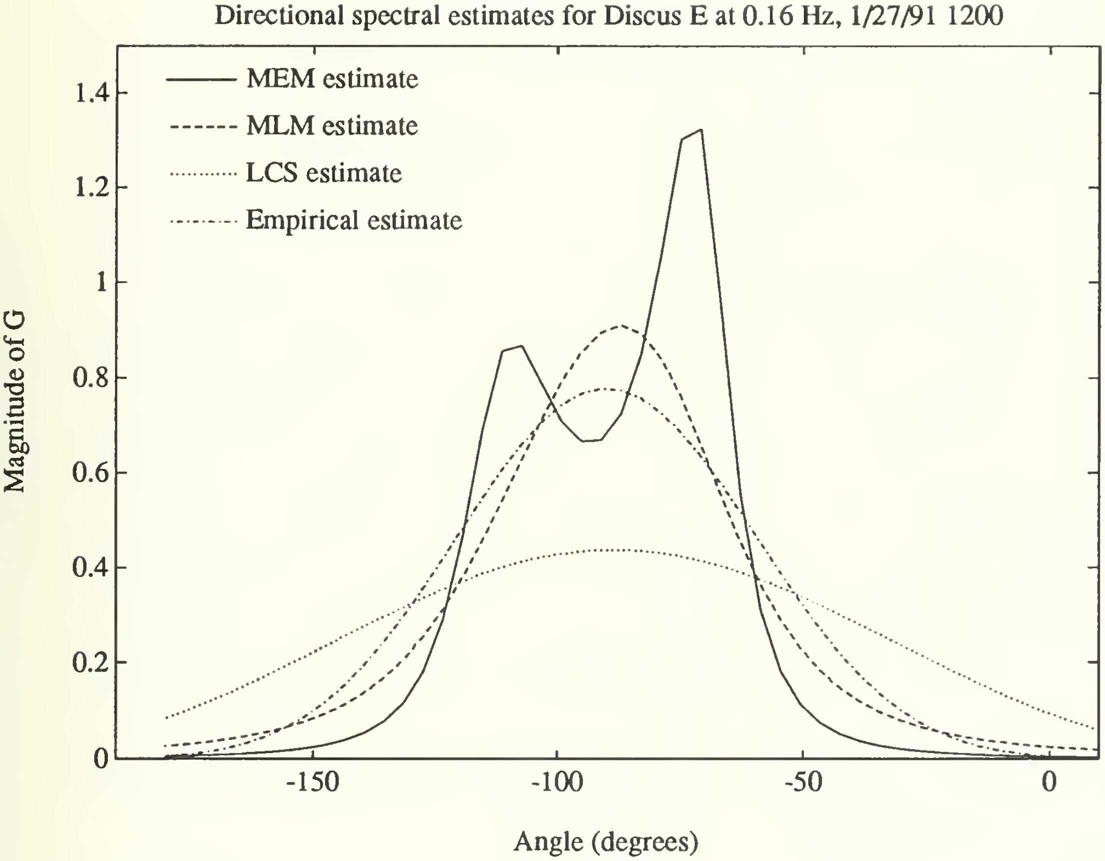

Figure 4: Estimated spectra derived from the 0.16 Hz data bin from the Discus E buoy on January 27, 1991 at 1200 hours. The estimates were made using the methods discussed in the caption to Fig. 3.

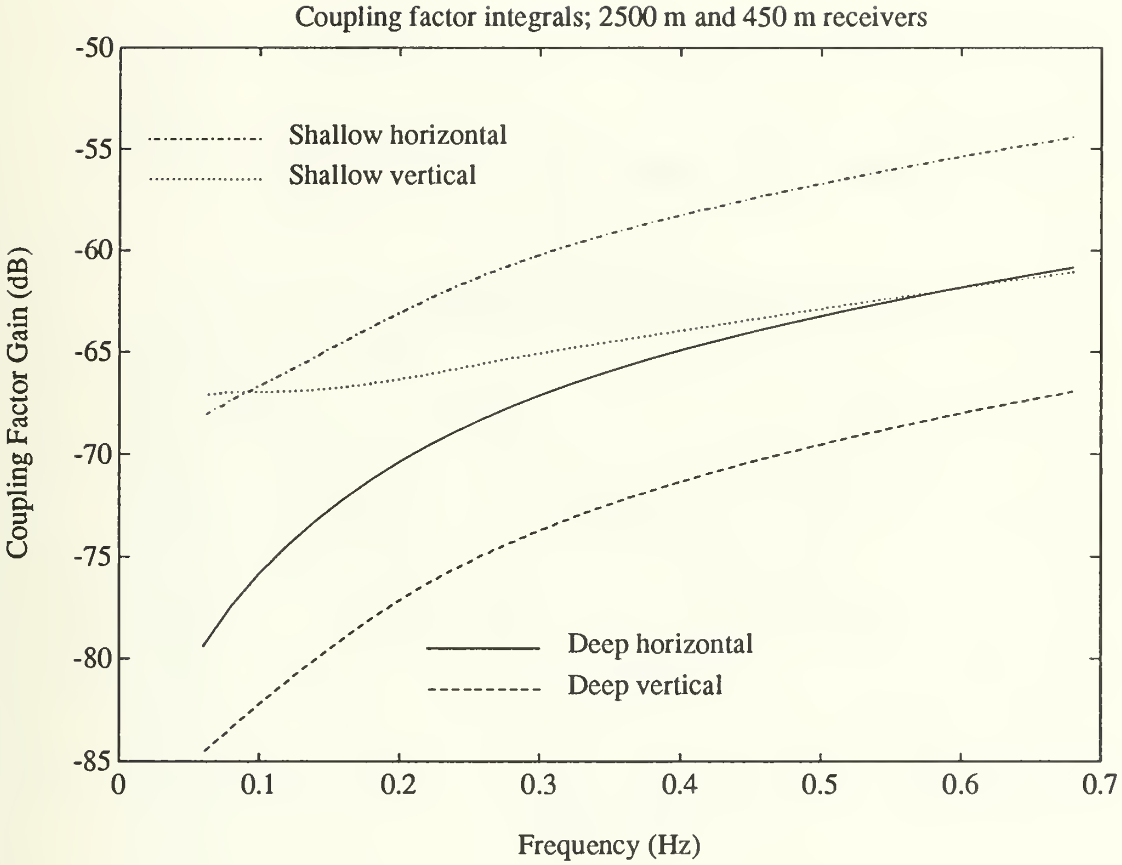

Figure 5: Plots of $10 \log \int_0^{k_0} (H_1 H_1^* + H_2 H_2^*) k \, dk$ and $10 \log \int_0^{k_0} H_3 H_3^* k \, dk$ for receiver depths of 450 meters and 2500 meters. k_0 was taken as $5\omega/c$, and an effective radius of 100 kilometers was used.

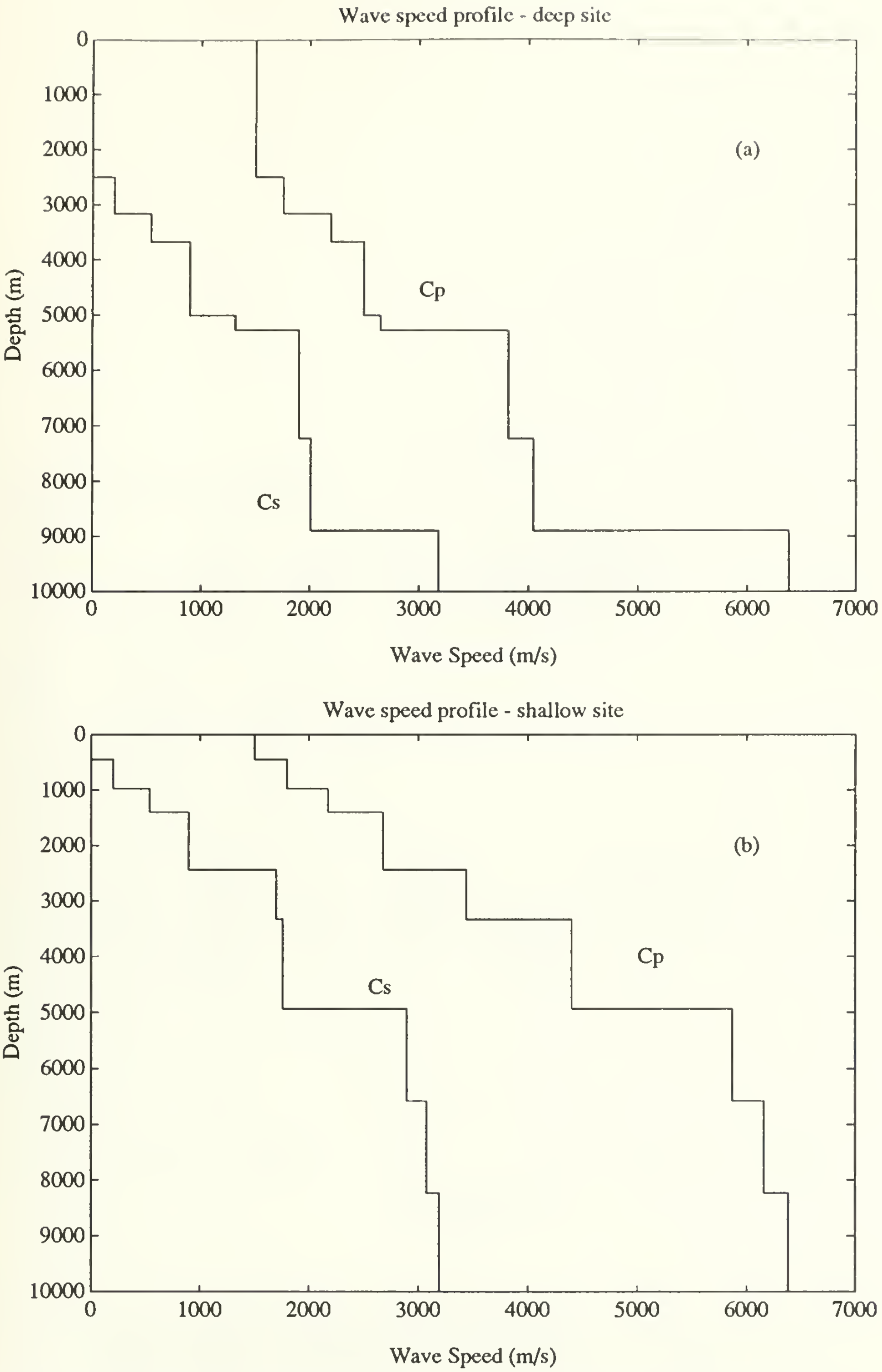

Figure 6: Profiles of compressional and shear wave speeds, Cp and Cs, used in the environmental model. Compressional wave speeds are based on unpublished data from the EDGE deep seismic reflection survey, and the shear wave speeds were derived from the compressional wave speeds, as described in the text. Figure 6a is the deep site and Fig. 6b is the shallow site.

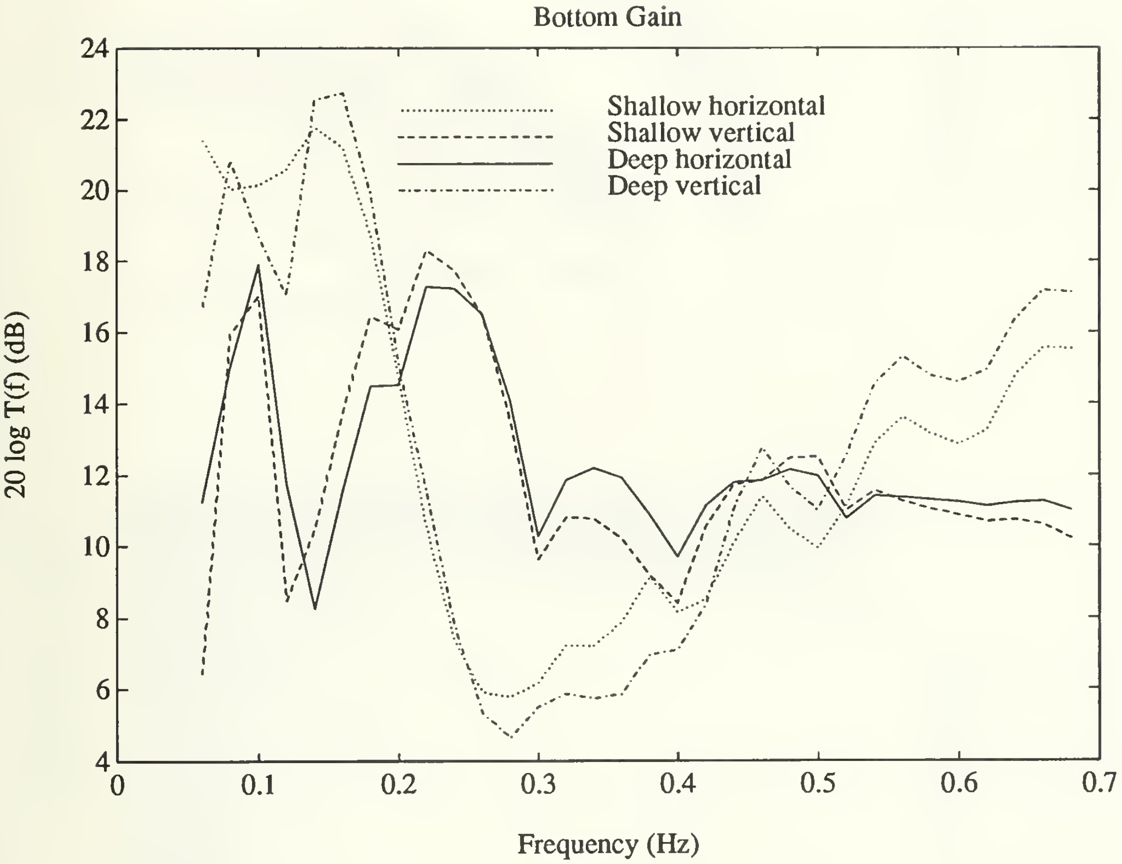

Figure 7: Plots of T_m^2 from data generated by SAFARI for the assumed bottom model at 450 m and 2500 m receiver depths for $m = 1$ and $m = 2$.

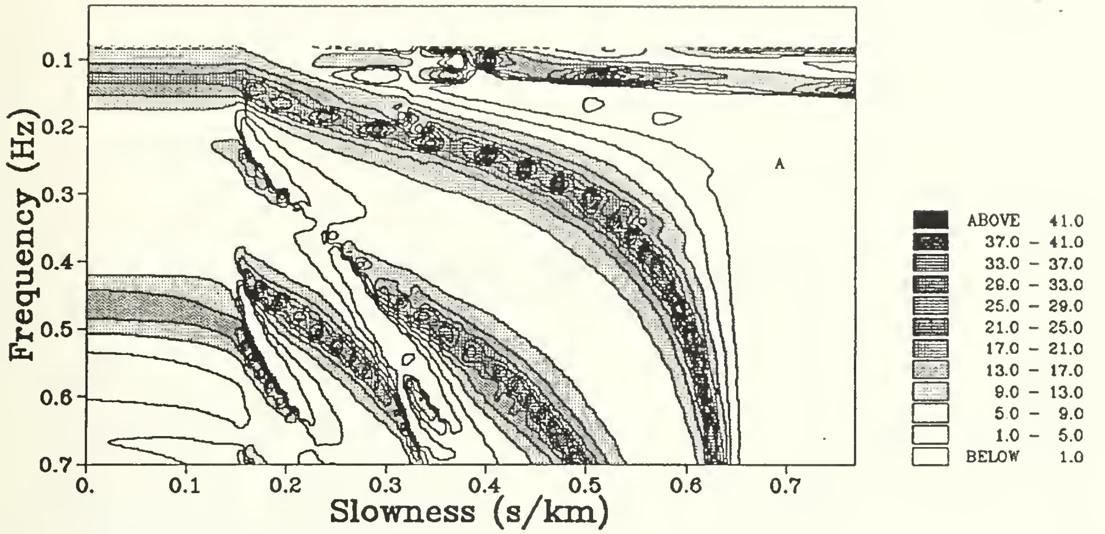

Deep site integrands

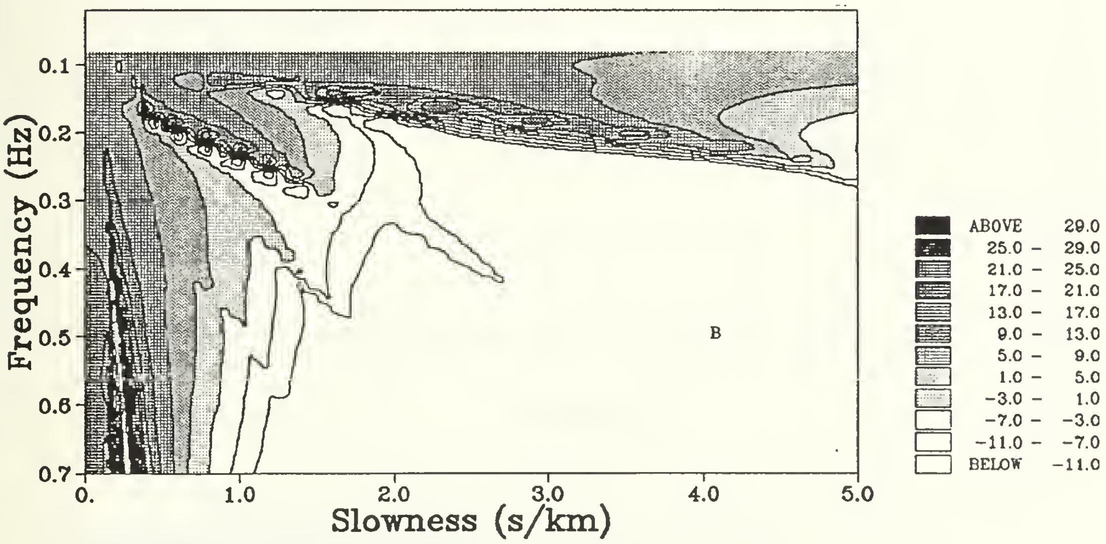

Shallow site integrands

Figure 8: Contours of the integrands of Eq. (4.41), the depth-dependent Green's functions $g(k, z, z')$, versus horizontal slowness $1/c = k/\omega$ and frequency for a) the deep site (2500 m) and b) the shallow site (450 m).

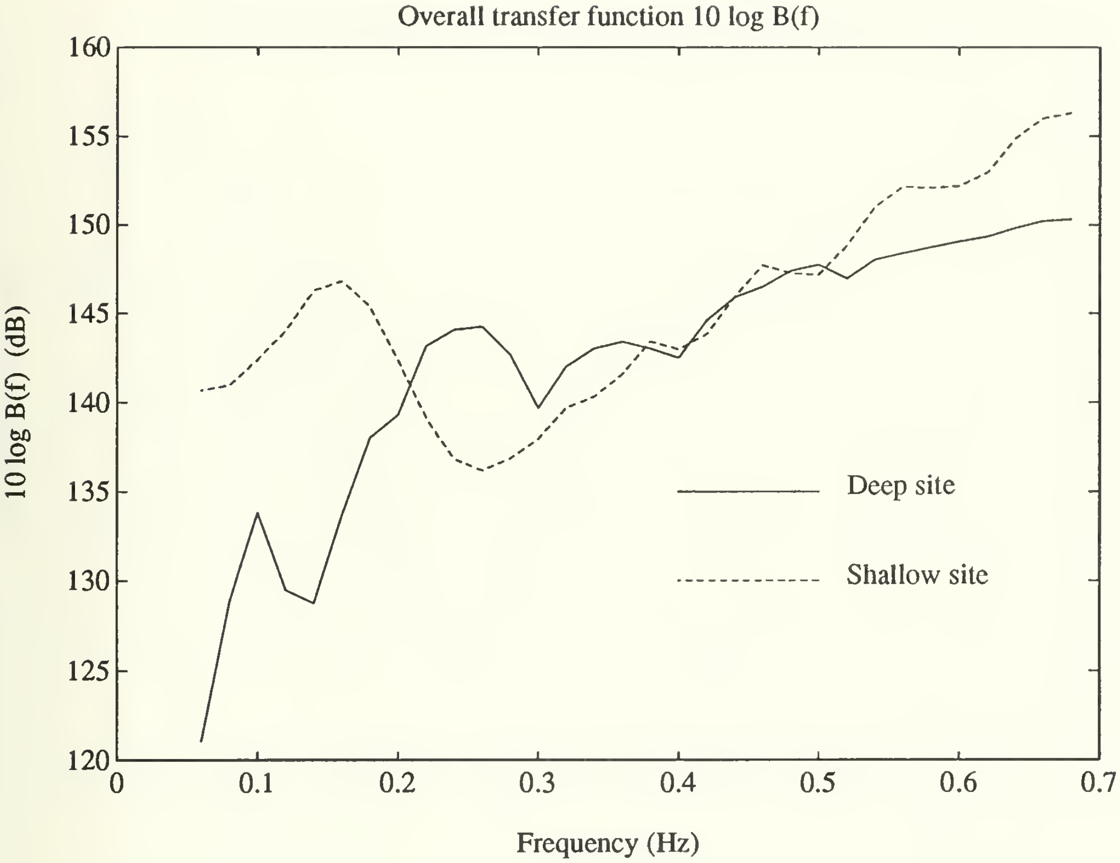

Figure 9: Plots of $10 \log B(f)$ for the deep and shallow sites.

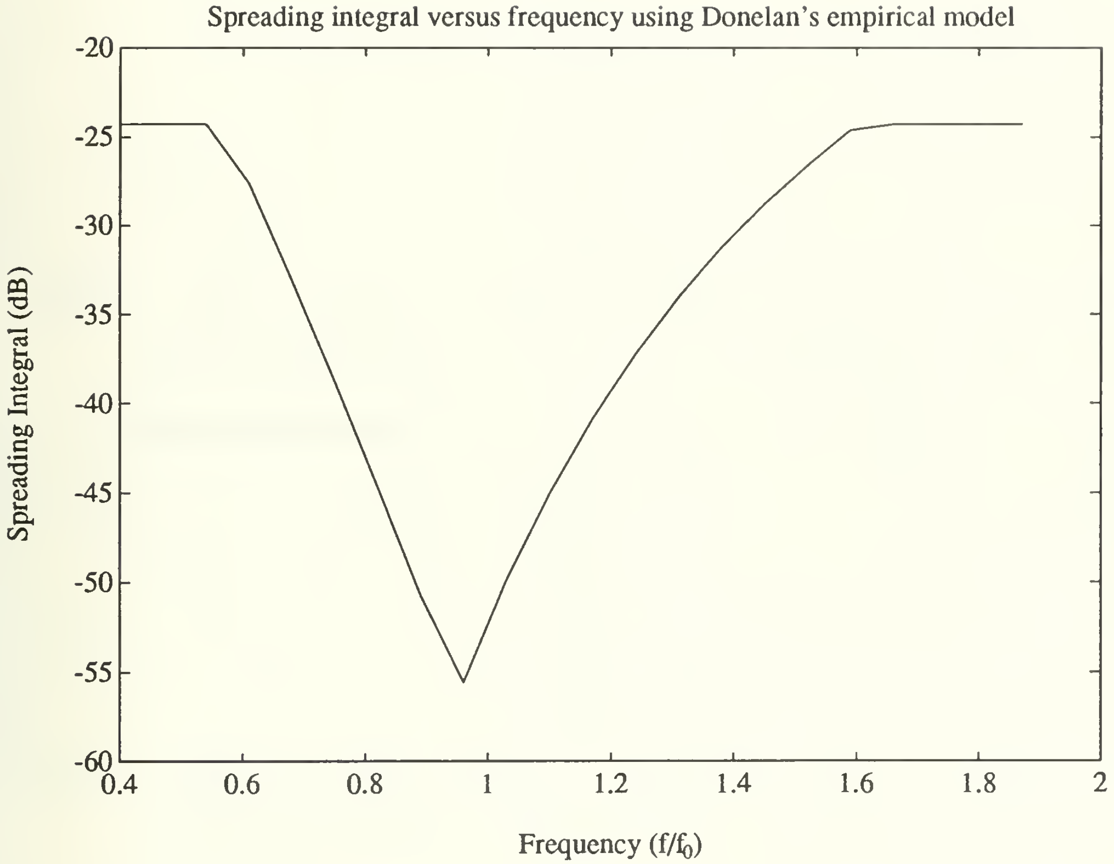

Figure 10: Plot of $10 \log I_{\alpha_{33}}$ versus normalized frequency f/f_0 using Donelan's empirical model for the directional wave spectrum [26] where f_0 is double the frequency at the peak in the wave height spectrum.

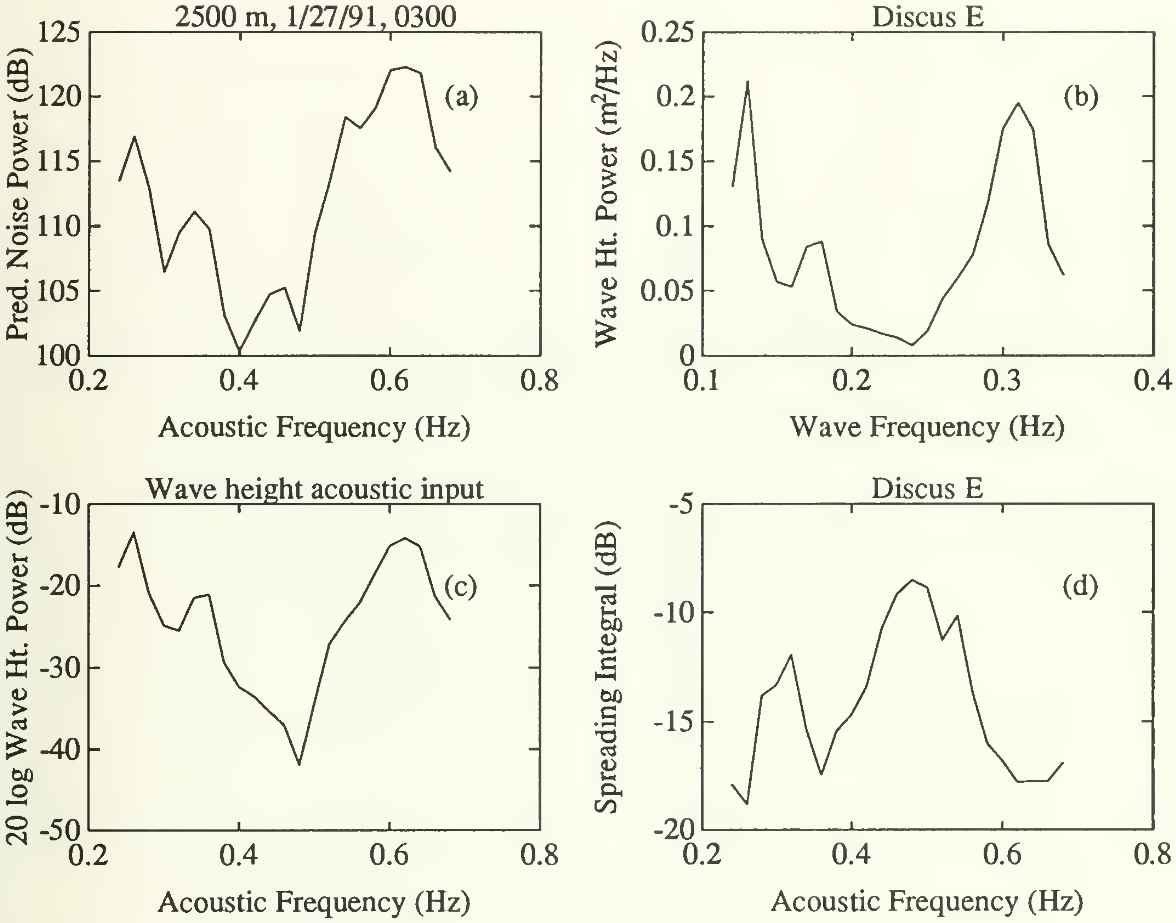

Figure 11: Predicted noise level and inputs for a 2500 meter receiver on 1/27/91 at 0300. a) Noise spectral level $10 \log P(f)$ in dB *re* $\mu\text{Pa}^2/\text{Hz}$. b) Wave height power spectrum $\Omega(\sigma/2\pi)$ in m^2/Hz. c) Wave height acoustic input $20 \log \Omega(f/2)$ in dB *re* m^2/Hz. d) Spreading integral level $10 \log I_{\alpha_{33}}(f)$ in dB *re* Hz^{-1}.

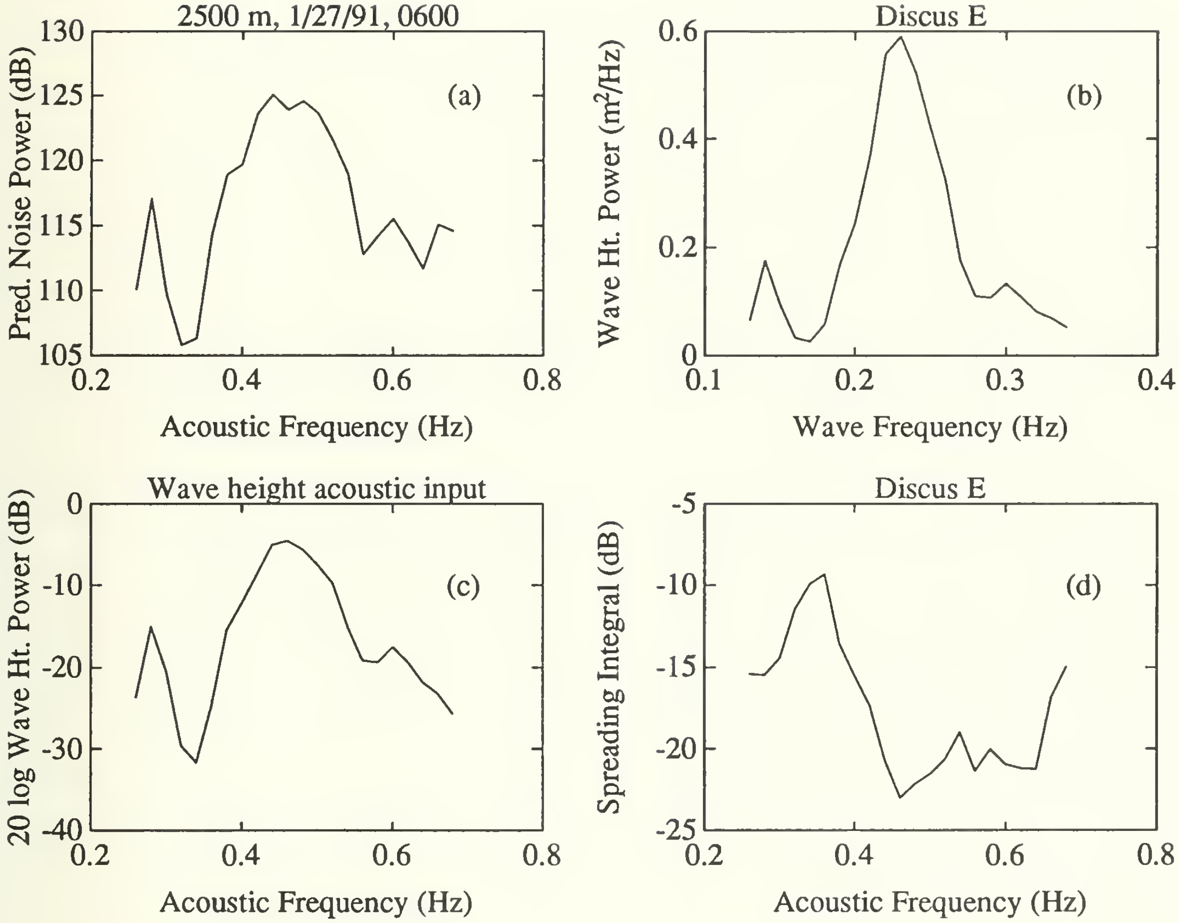

Figure 12: Predicted noise level and inputs for a 2500 m receiver on 1/27/91 at 0600. a) Noise spectral level $10 \log P(f)$ in dB *re* $\mu\mathrm{Pa}^2/\mathrm{Hz}$. b) Wave height power spectrum $\Omega(\sigma/2\pi)$ in m^2/Hz. c) Wave height acoustic input $20 \log \Omega(f/2)$ in dB *re* m^2/Hz. d) Spreading integral level $10 \log I_{\alpha_{33}}(f)$ in dB *re* Hz^{-1}.

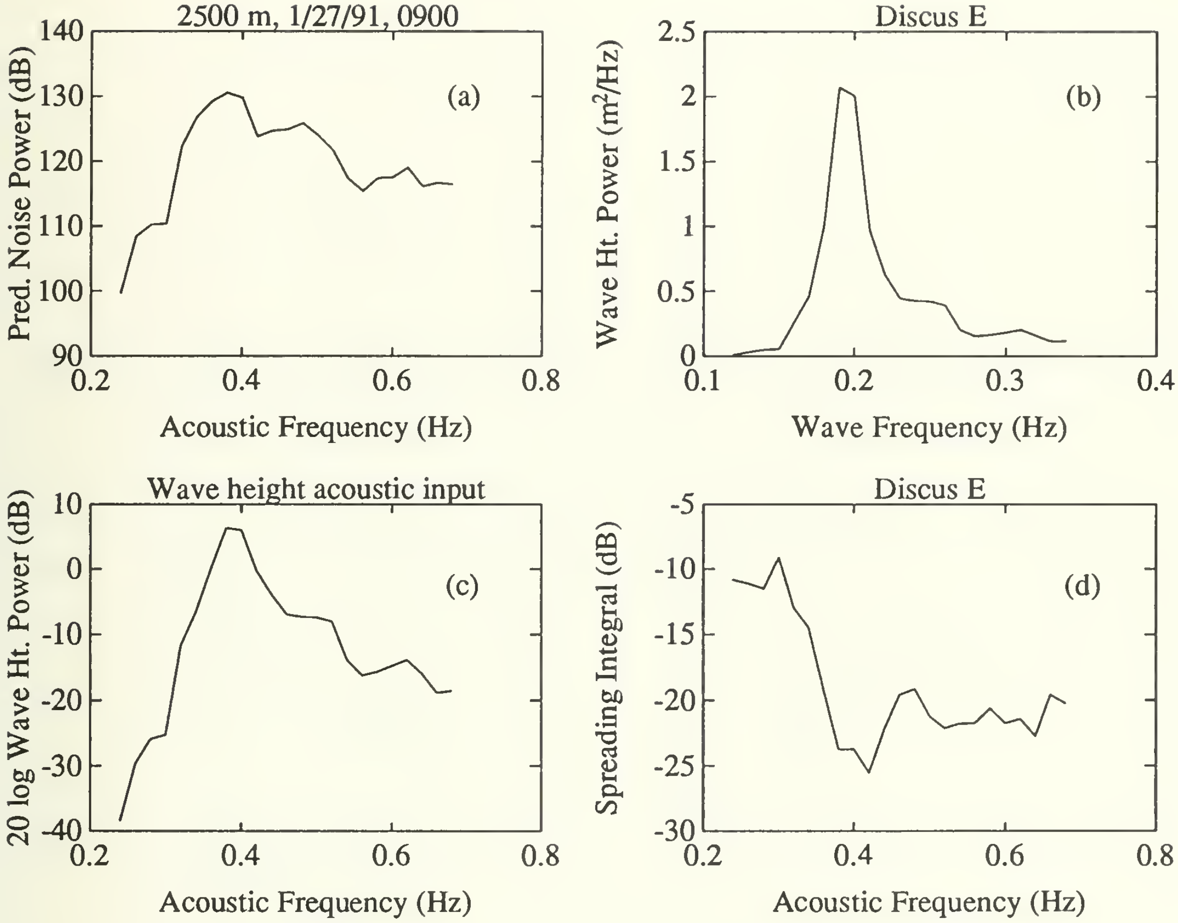

Figure 13: Predicted noise level and inputs for a 2500 m receiver on 1/27/91 at 0900. a) Noise spectral level $10 \log P(f)$ in dB *re* $\mu\mathrm{Pa}^2/\mathrm{Hz}$. b) Wave height power spectrum $\Omega(\sigma/2\pi)$ in m^2/Hz. c) Wave height acoustic input $20 \log \Omega(f/2)$ in dB *re* m^2/Hz. d) Spreading integral level $10 \log I_{\alpha_{33}}(f)$ in dB *re* Hz^{-1}.

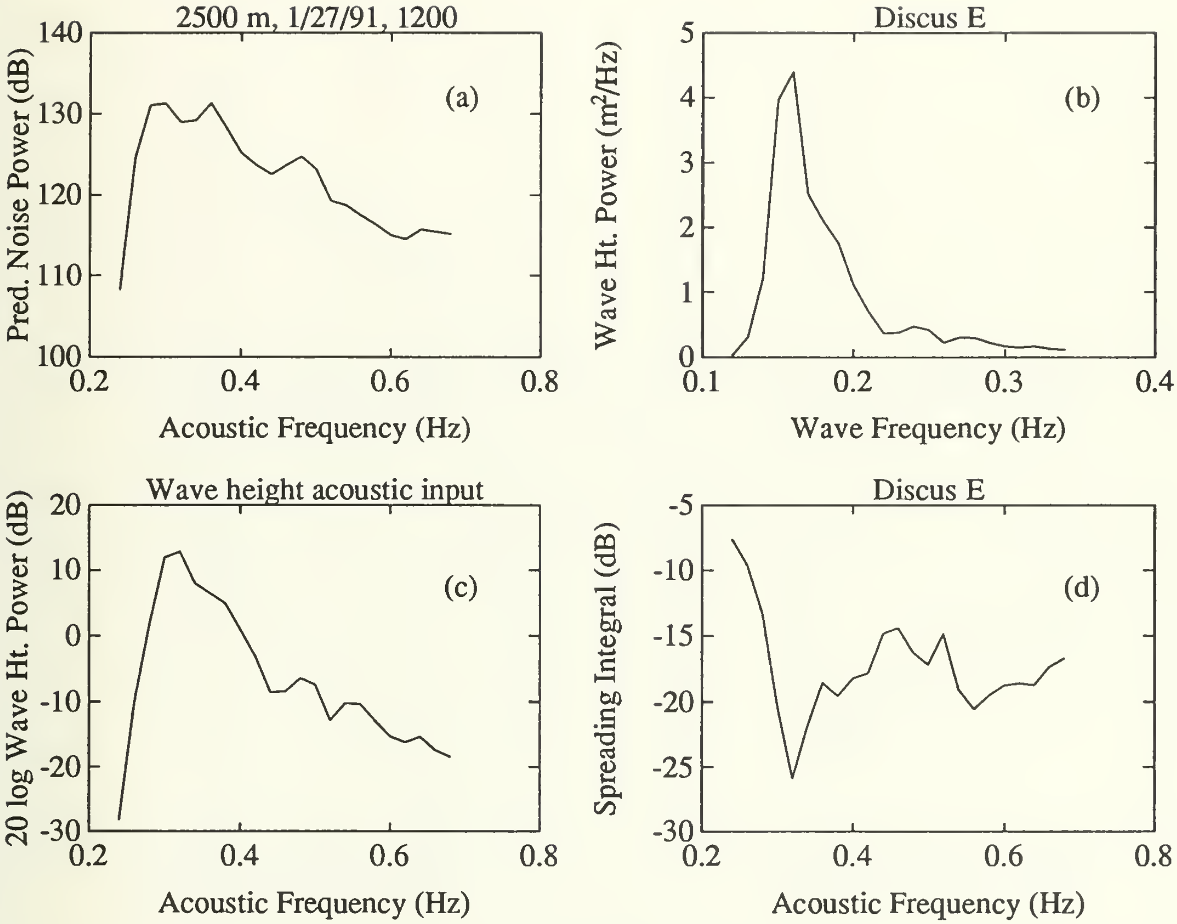

Figure 14: Predicted noise level and inputs for a 2500 m receiver on 1/27/91 at 1200. a) Noise spectral level 10 log $P(f)$ in dB *re* $\mu\mathrm{Pa}^2/\mathrm{Hz}$. b) Wave height power spectrum $\Omega(\sigma/2\pi)$ in m^2/Hz. c) Wave height acoustic input 20 log $\Omega(f/2)$ in dB *re* m^2/Hz. d) Spreading integral level 10 log $I_{\alpha_{33}}(f)$ in dB *re* Hz^{-1}.

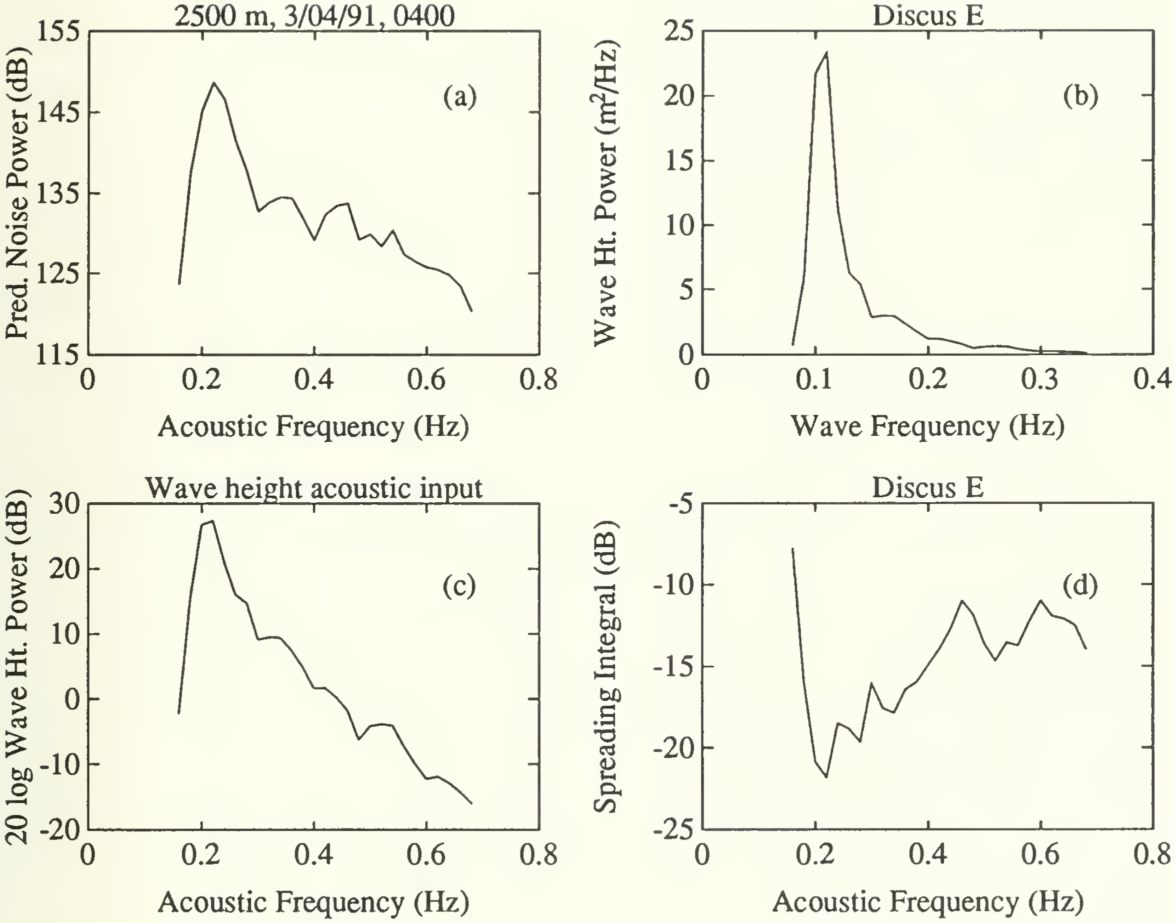

Figure 15: Predicted noise level and inputs for a 2500 m receiver on 3/04/91 at 0400. a) Noise spectral level $10 \log P(f)$ in dB *re* μPa^2/Hz. b) Wave height power spectrum $\Omega(\sigma/2\pi)$ in m^2/Hz. c) Wave height acoustic input $20 \log \Omega(f/2)$ in dB *re* m^2/Hz. d) Spreading integral level $10 \log I_{\alpha_{33}}(f)$ in dB *re* Hz^{-1}.

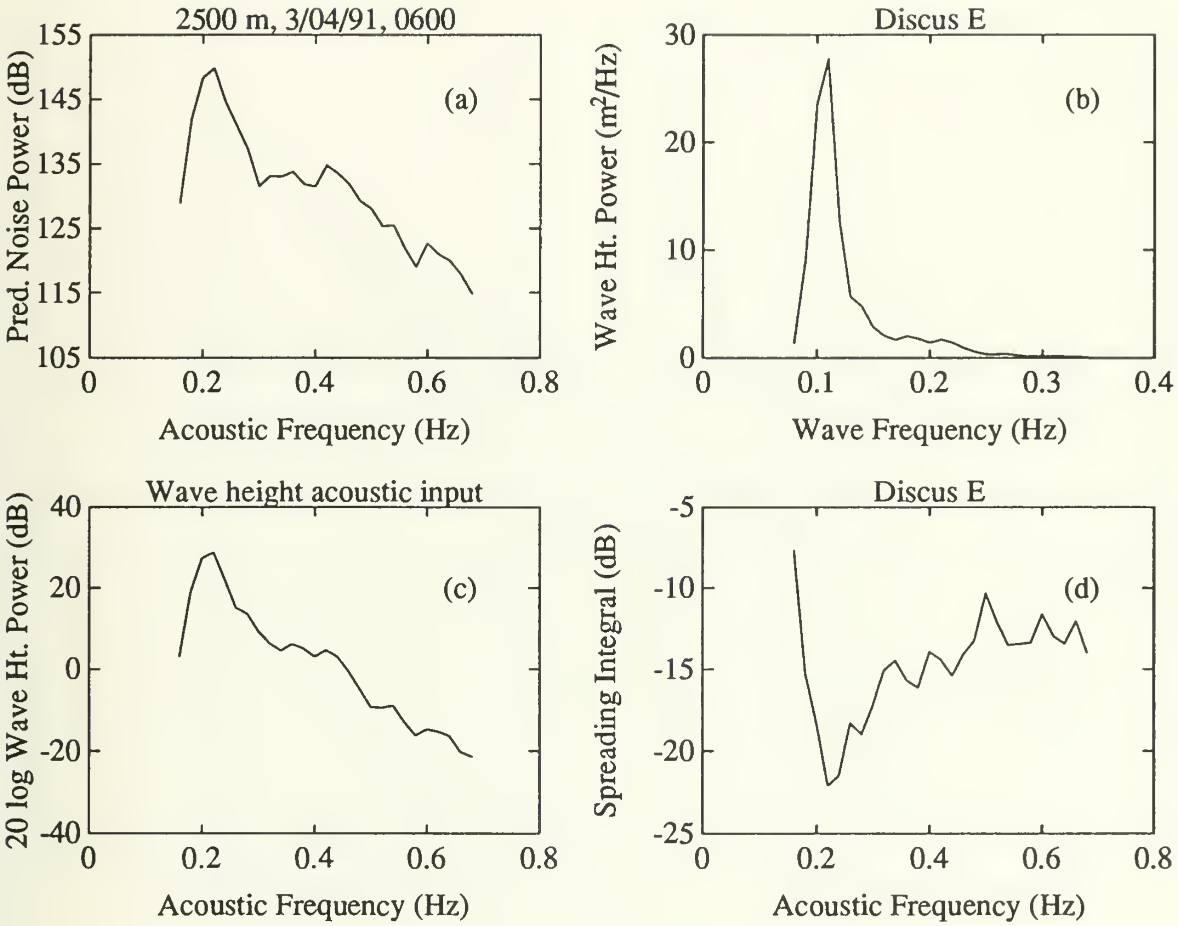

Figure 16: Predicted noise level and inputs for a 2500 m receiver on 3/04/91 at 0600. a) Noise spectral level $10 \log P(f)$ in dB *re* $\mu\text{Pa}^2/\text{Hz}$. b) Wave height power spectrum $\Omega(\sigma/2\pi)$ in m^2/Hz. c) Wave height acoustic input $20 \log \Omega(f/2)$ in dB *re* m^2/Hz. d) Spreading integral level $10 \log I_{\alpha_{33}}(f)$ in dB *re* Hz^{-1}.

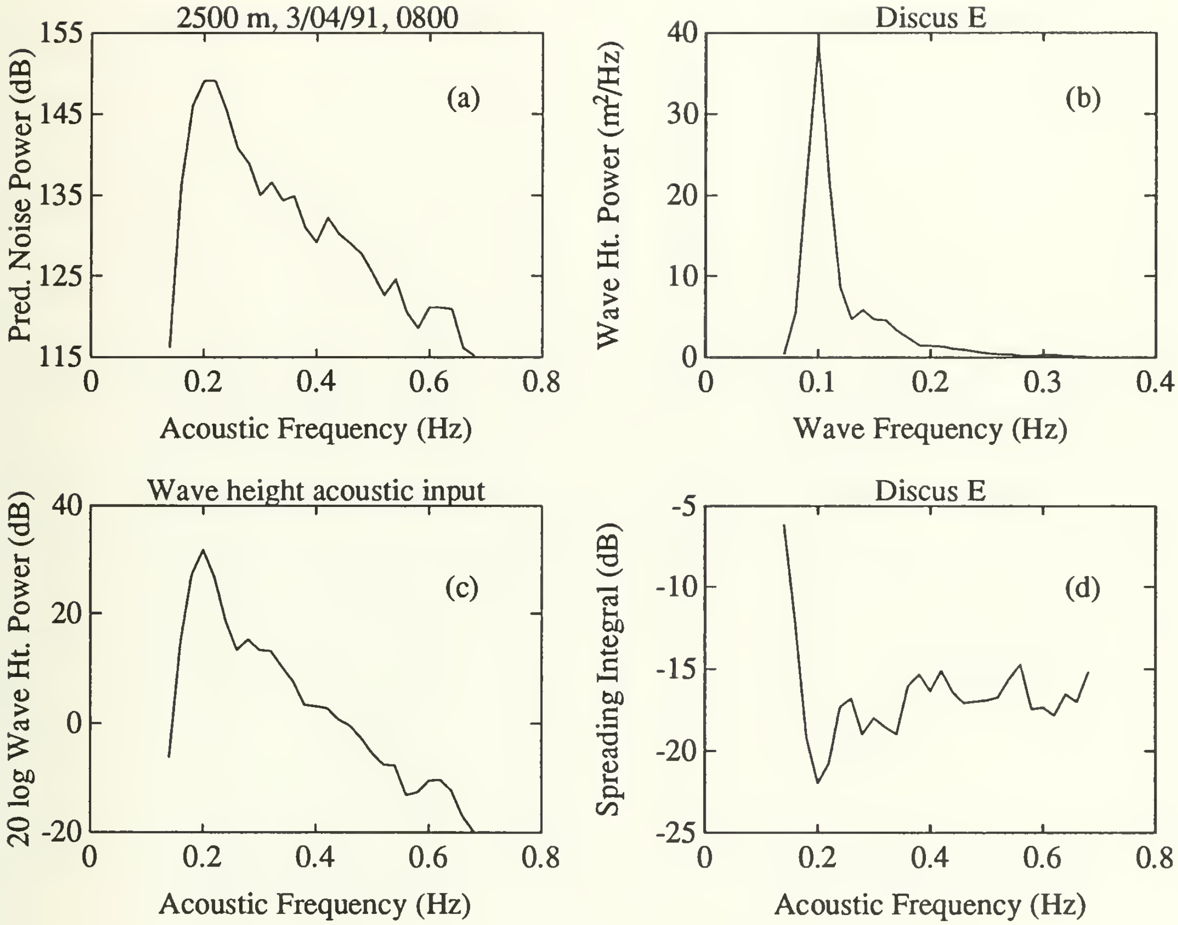

Figure 17: Predicted noise level and inputs for a 2500 m receiver on 3/04/91 at 0800. a) Noise spectral level $10\log P(f)$ in dB *re* $\mu\mathrm{Pa}^2/\mathrm{Hz}$. b) Wave height power spectrum $\Omega(\sigma/2\pi)$ in m^2/Hz. c) Wave height acoustic input $20\log\Omega(f/2)$ in dB *re* m^2/Hz. d) Spreading integral level $10\log I_{\alpha_{33}}(f)$ in dB *re* Hz^{-1}.

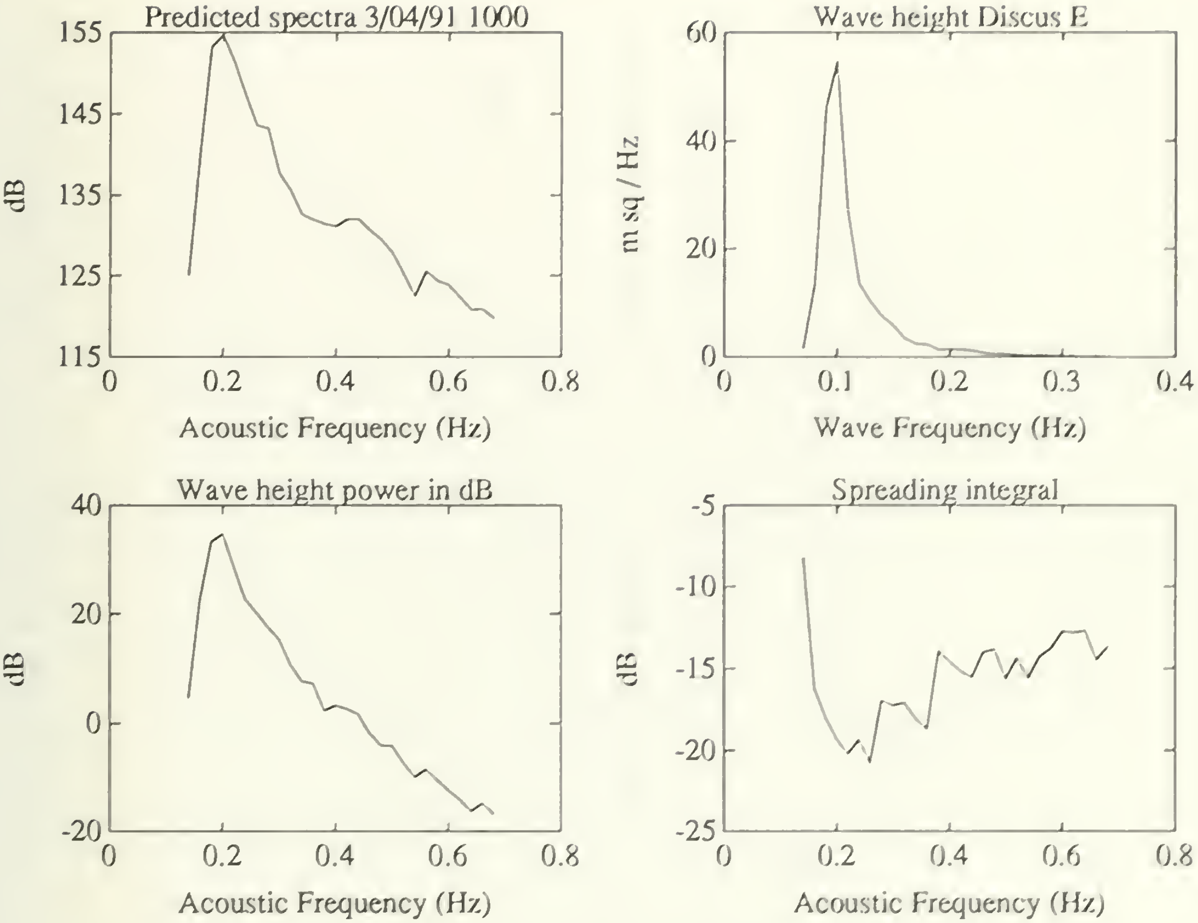

Figure 18: Predicted noise level and inputs for a 2500 m receiver on 3/04/91 at 1000. a) Noise spectral level 10 log $P(f)$ in dB *re* $\mu\text{Pa}^2/\text{Hz}$. b) Wave height power spectrum $\Omega(\sigma/2\pi)$ in m^2/Hz. c) Wave height acoustic input 20 log $\Omega(f/2)$ in dB *re* m^2/Hz. d) Spreading integral level 10 log $I_{\sigma_{11}}(f)$ in dB *re* Hz^{-1}.

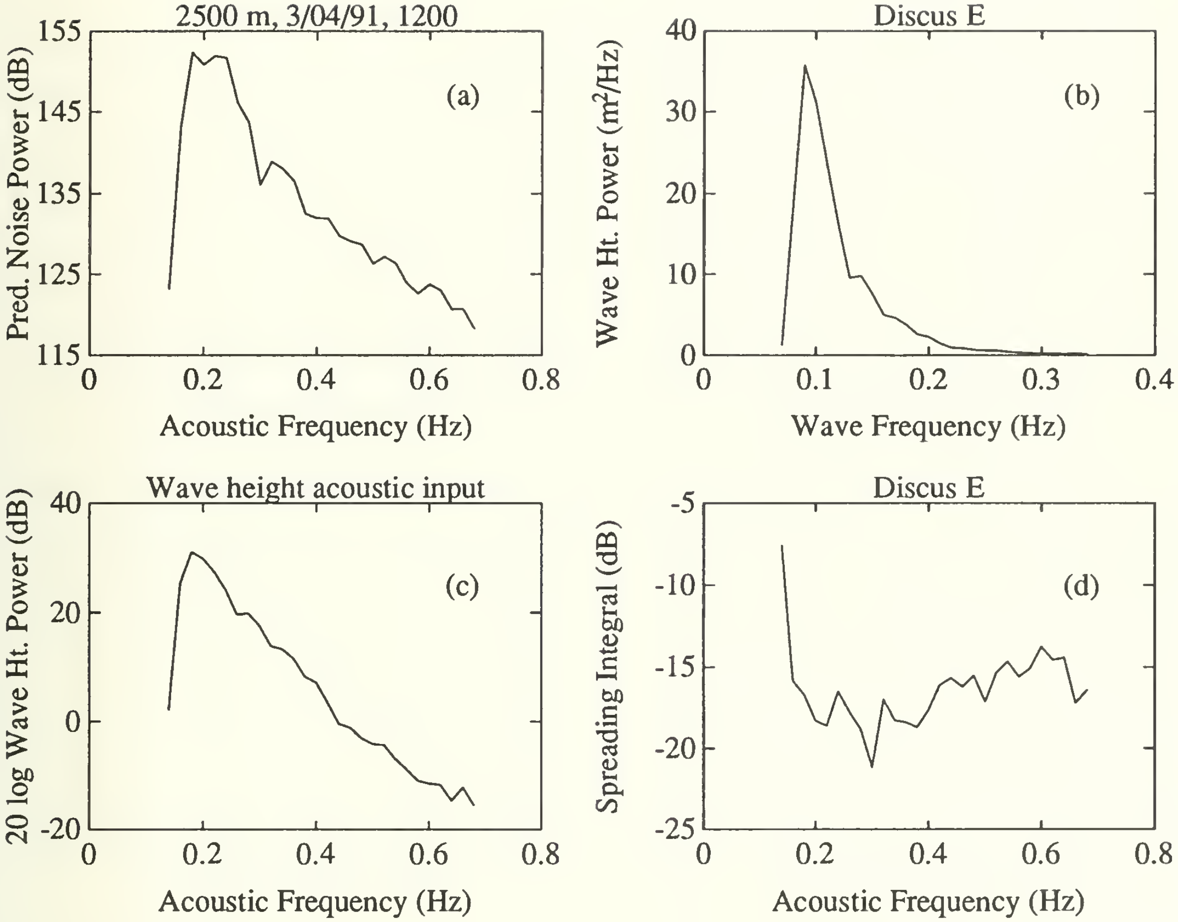

Figure 19: Predicted noise level and inputs for a 2500 m receiver on 3/04/91 at 1200. a) Noise spectral level $10 \log P(f)$ in dB *re* $\mu\mathrm{Pa}^2/\mathrm{Hz}$. b) Wave height power spectrum $\Omega(\sigma/2\pi)$ in m^2/Hz. c) Wave height acoustic input $20 \log \Omega(f/2)$ in dB *re* m^2/Hz. d) Spreading integral level $10 \log I_{\alpha_{33}}(f)$ in dB *re* Hz^{-1}.

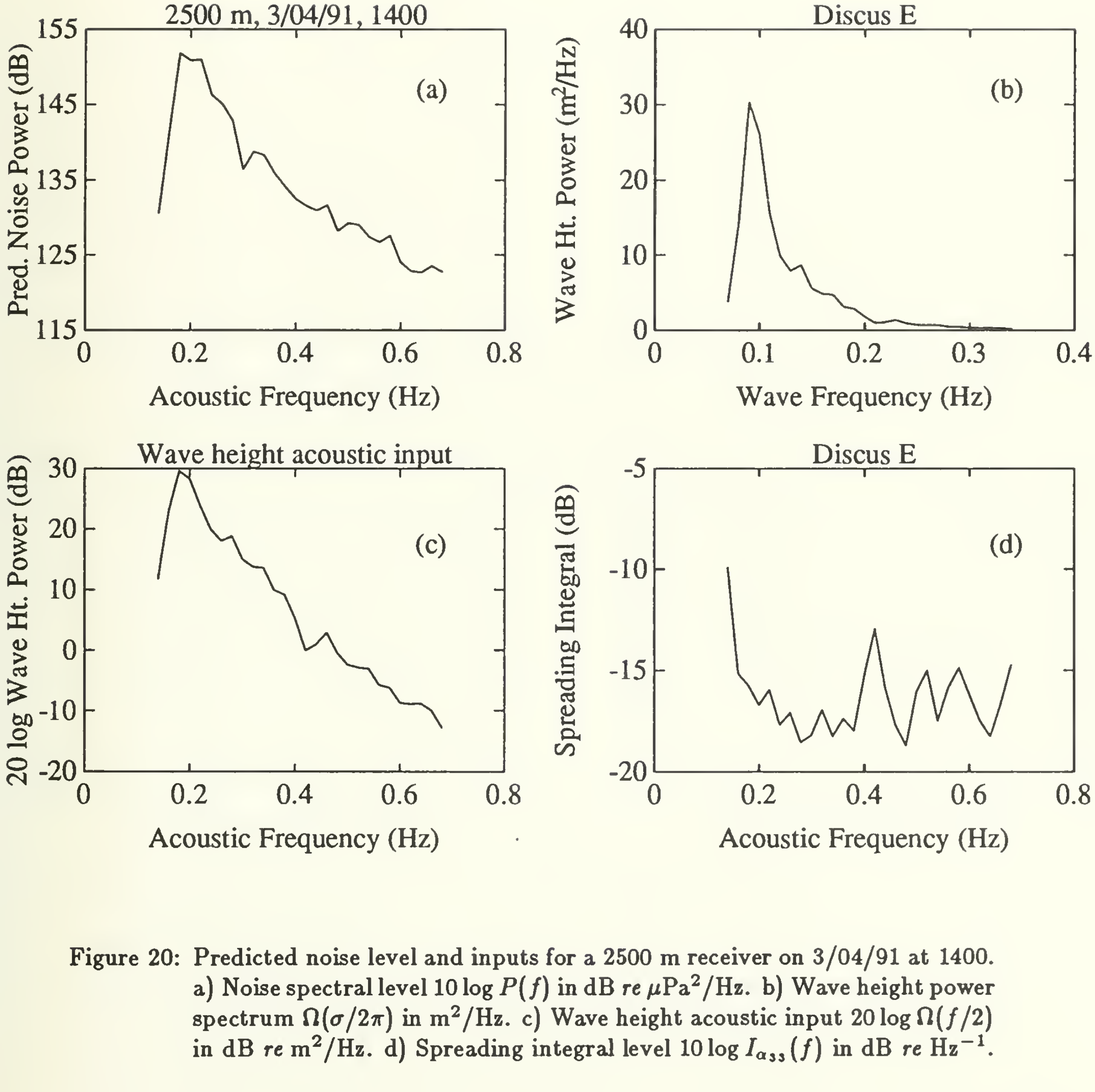

Figure 20: Predicted noise level and inputs for a 2500 m receiver on 3/04/91 at 1400. a) Noise spectral level $10\log P(f)$ in dB *re* μPa^2/Hz. b) Wave height power spectrum $\Omega(\sigma/2\pi)$ in m^2/Hz. c) Wave height acoustic input $20\log\Omega(f/2)$ in dB *re* m^2/Hz. d) Spreading integral level $10\log I_{\alpha_{33}}(f)$ in dB *re* Hz^{-1}.

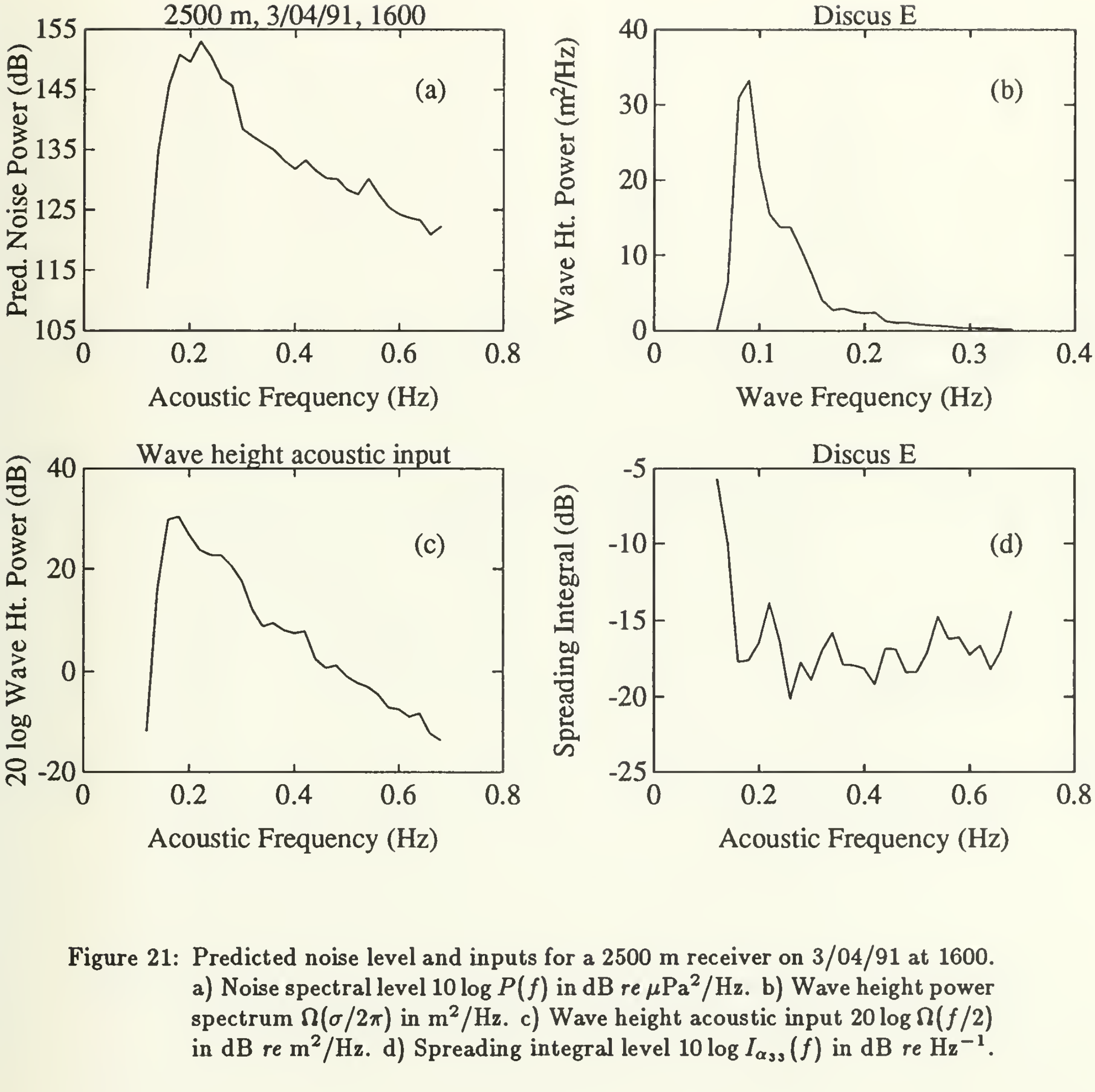

Figure 21: Predicted noise level and inputs for a 2500 m receiver on 3/04/91 at 1600. a) Noise spectral level $10 \log P(f)$ in dB *re* $\mu\mathrm{Pa}^2/\mathrm{Hz}$. b) Wave height power spectrum $\Omega(\sigma/2\pi)$ in m^2/Hz. c) Wave height acoustic input $20 \log \Omega(f/2)$ in dB *re* m^2/Hz. d) Spreading integral level $10 \log I_{\alpha_{33}}(f)$ in dB *re* Hz^{-1}.

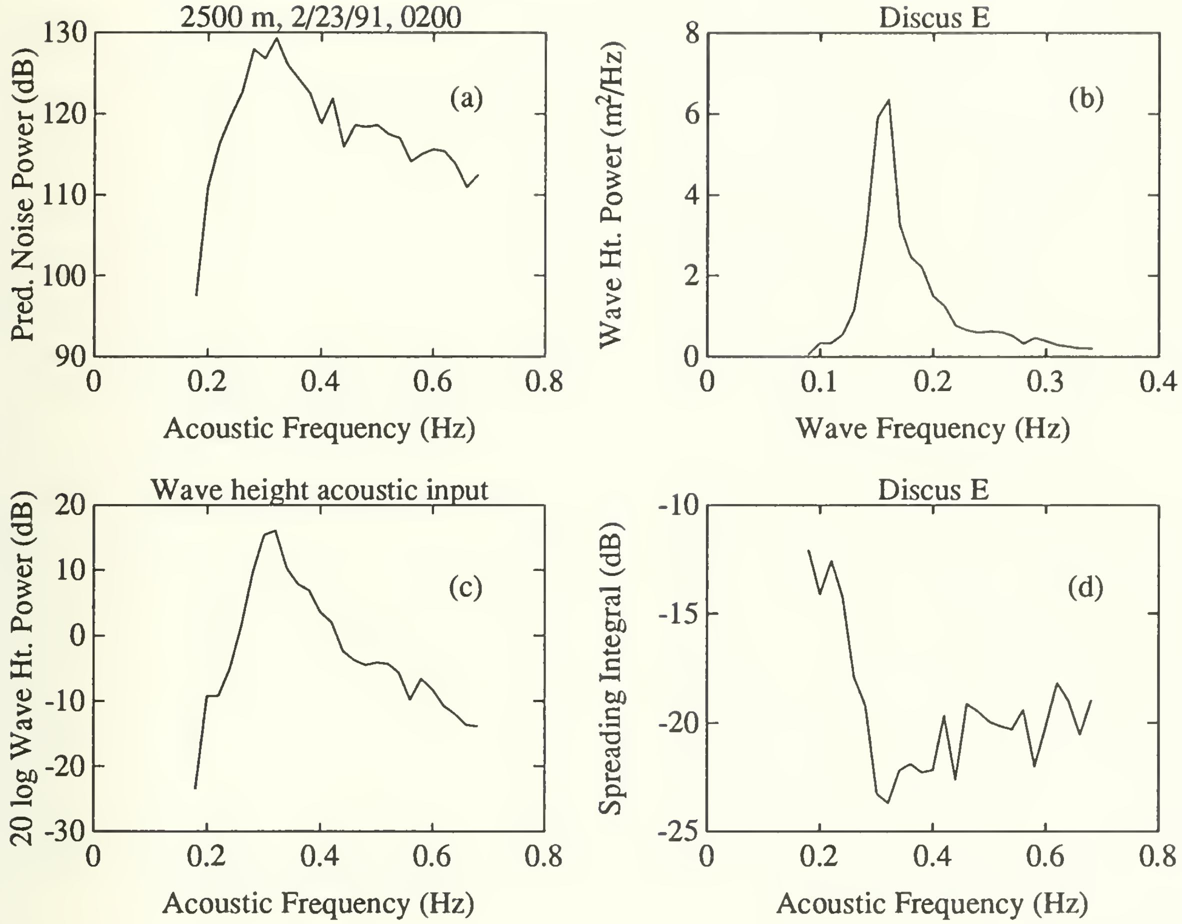

Figure 22: Predicted noise level and inputs for a 2500 m receiver on 2/23/91 at 0200. a) Noise spectral level $10 \log P(f)$ in dB *re* $\mu\mathrm{Pa}^2/\mathrm{Hz}$. b) Wave height power spectrum $\Omega(\sigma/2\pi)$ in m^2/Hz. c) Wave height acoustic input $20 \log \Omega(f/2)$ in dB *re* m^2/Hz. d) Spreading integral level $10 \log I_{\alpha_{33}}(f)$ in dB *re* Hz^{-1}.

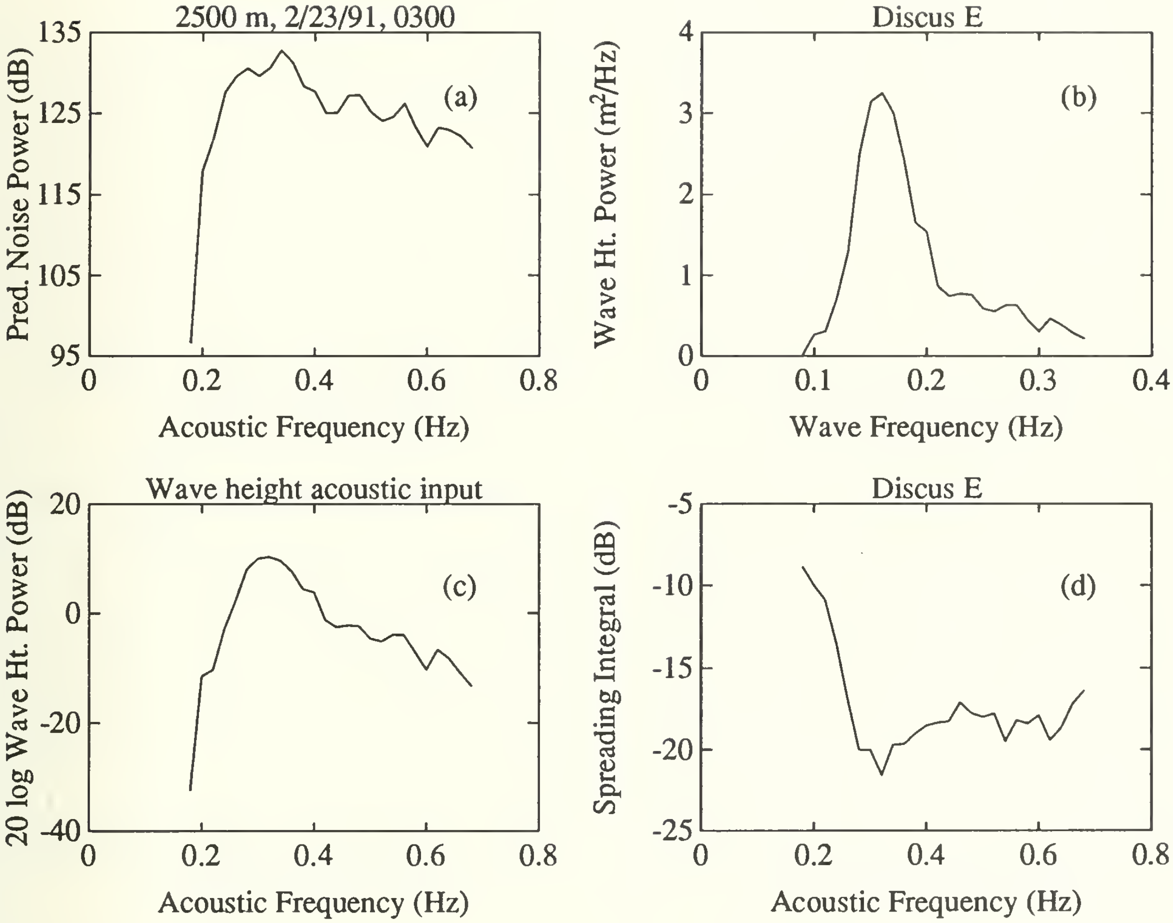

Figure 23: Predicted noise level and inputs for a 2500 m receiver on 2/23/91 at 0300. a) Noise spectral level $10 \log P(f)$ in dB *re* $\mu\mathrm{Pa}^2/\mathrm{Hz}$. b) Wave height power spectrum $\Omega(\sigma/2\pi)$ in m^2/Hz. c) Wave height acoustic input $20 \log \Omega(f/2)$ in dB *re* m^2/Hz. d) Spreading integral level $10 \log I_{\alpha_{33}}(f)$ in dB *re* Hz^{-1}.

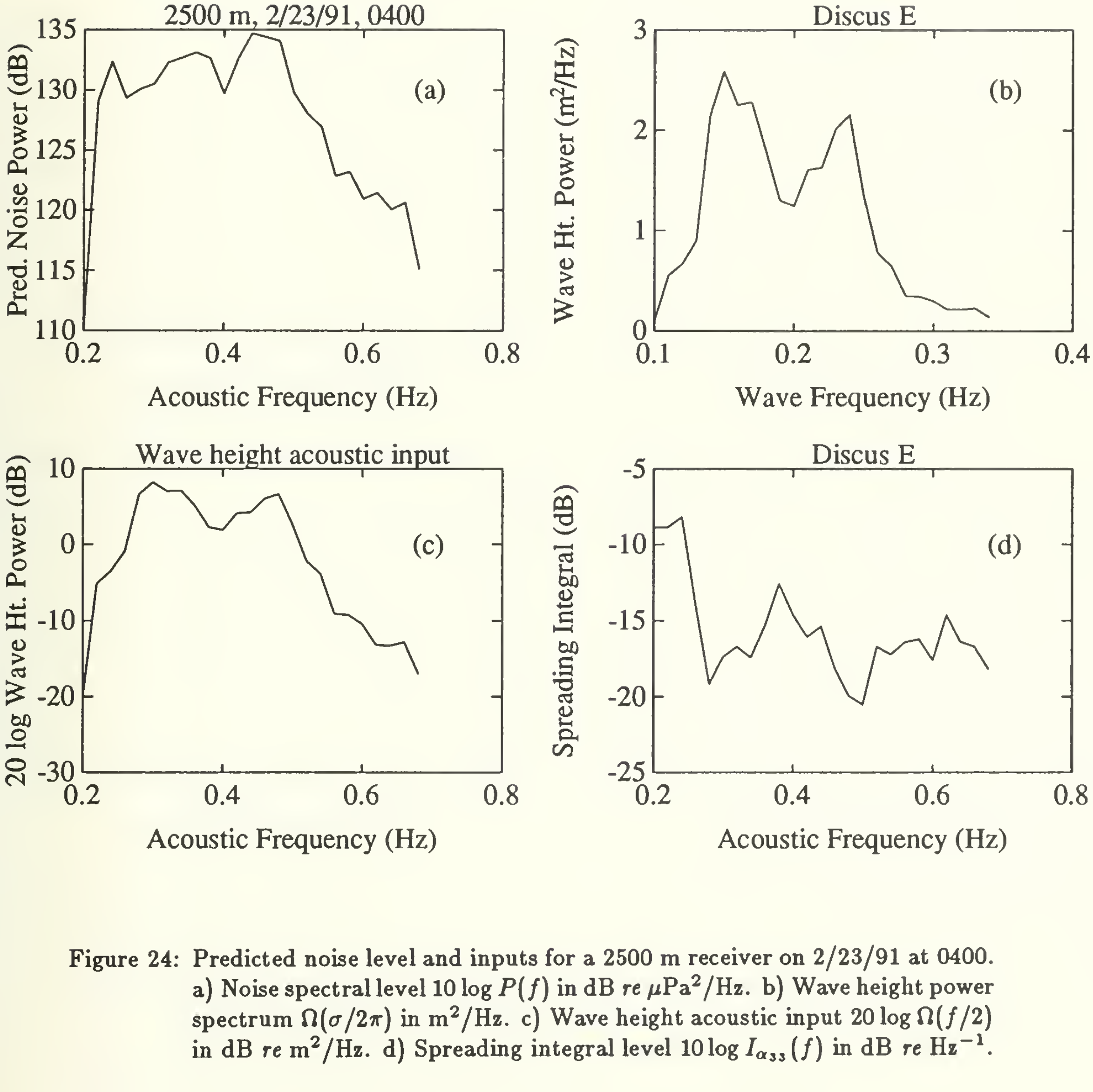

Figure 24: Predicted noise level and inputs for a 2500 m receiver on 2/23/91 at 0400. a) Noise spectral level $10 \log P(f)$ in dB *re* $\mu\text{Pa}^2/\text{Hz}$. b) Wave height power spectrum $\Omega(\sigma/2\pi)$ in m^2/Hz. c) Wave height acoustic input $20 \log \Omega(f/2)$ in dB *re* m^2/Hz. d) Spreading integral level $10 \log I_{\alpha_{33}}(f)$ in dB *re* Hz^{-1}.

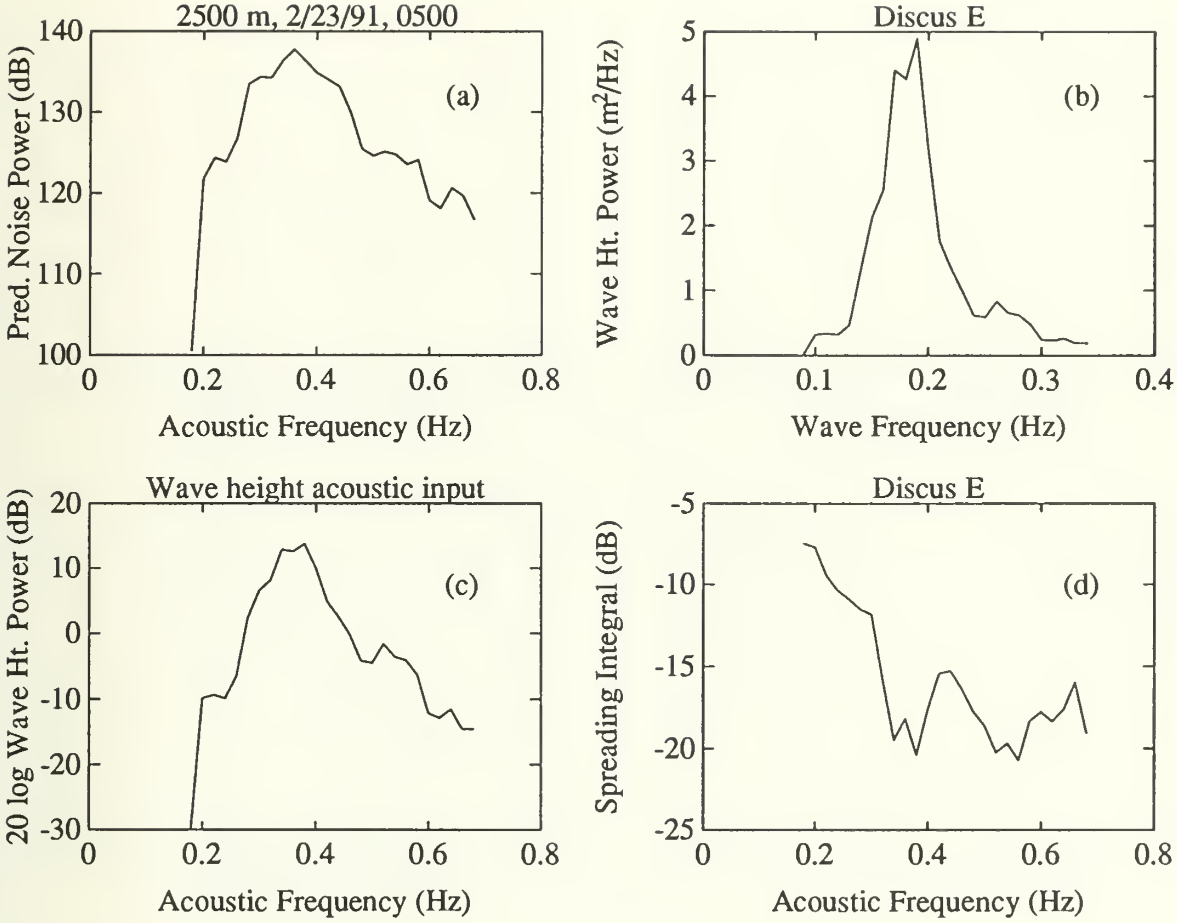

Figure 25: Predicted noise level and inputs for a 2500 m receiver on 2/23/91 at 0500. a) Noise spectral level $10 \log P(f)$ in dB *re* $\mu\mathrm{Pa}^2/\mathrm{Hz}$. b) Wave height power spectrum $\Omega(\sigma/2\pi)$ in m^2/Hz. c) Wave height acoustic input $20 \log \Omega(f/2)$ in dB *re* m^2/Hz. d) Spreading integral level $10 \log I_{\alpha_{33}}(f)$ in dB *re* Hz^{-1}.

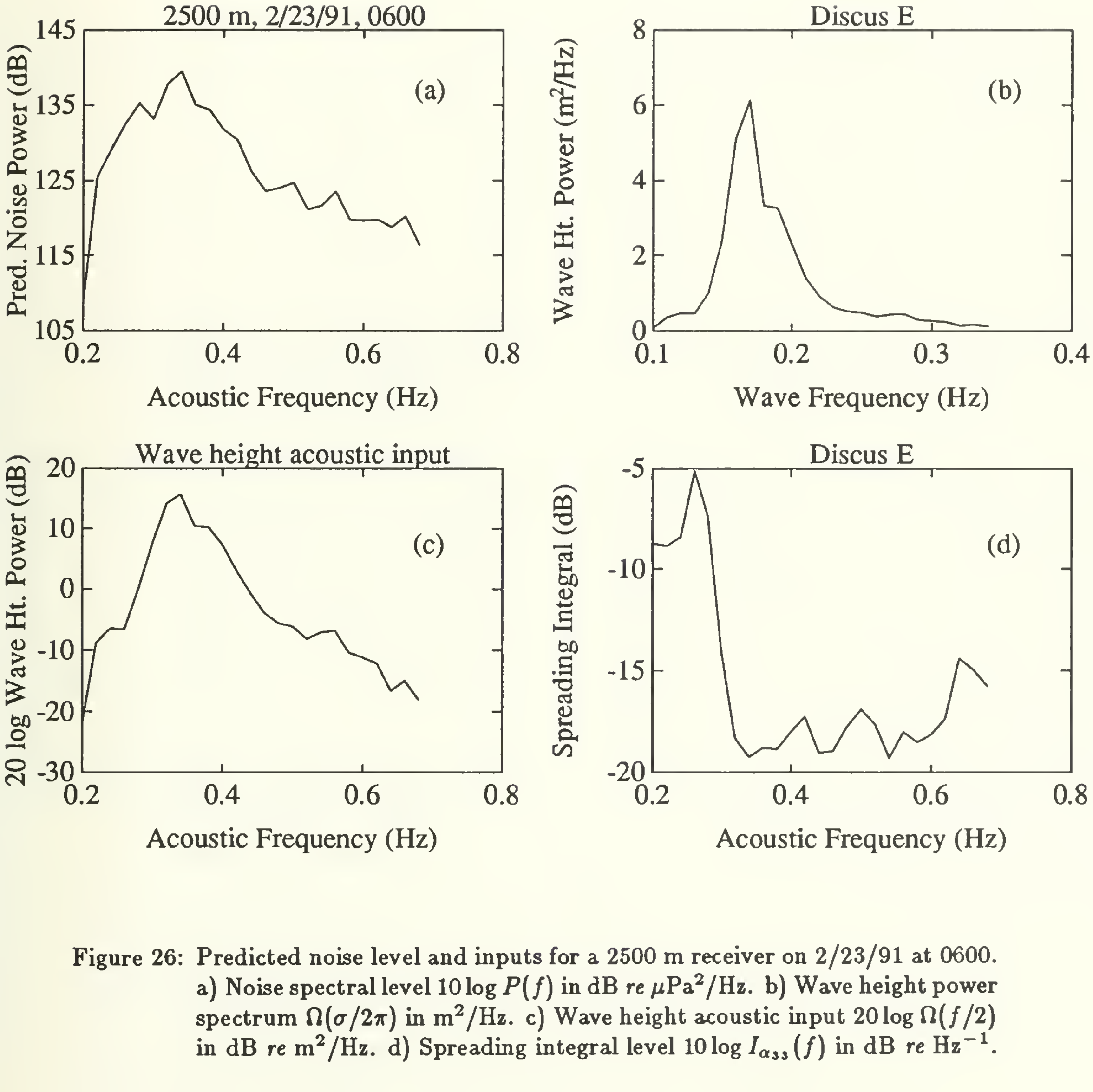

Figure 26: Predicted noise level and inputs for a 2500 m receiver on 2/23/91 at 0600. a) Noise spectral level $10 \log P(f)$ in dB *re* μPa^2/Hz. b) Wave height power spectrum $\Omega(\sigma/2\pi)$ in m^2/Hz. c) Wave height acoustic input $20 \log \Omega(f/2)$ in dB *re* m^2/Hz. d) Spreading integral level $10 \log I_{\alpha_{33}}(f)$ in dB *re* Hz^{-1}.

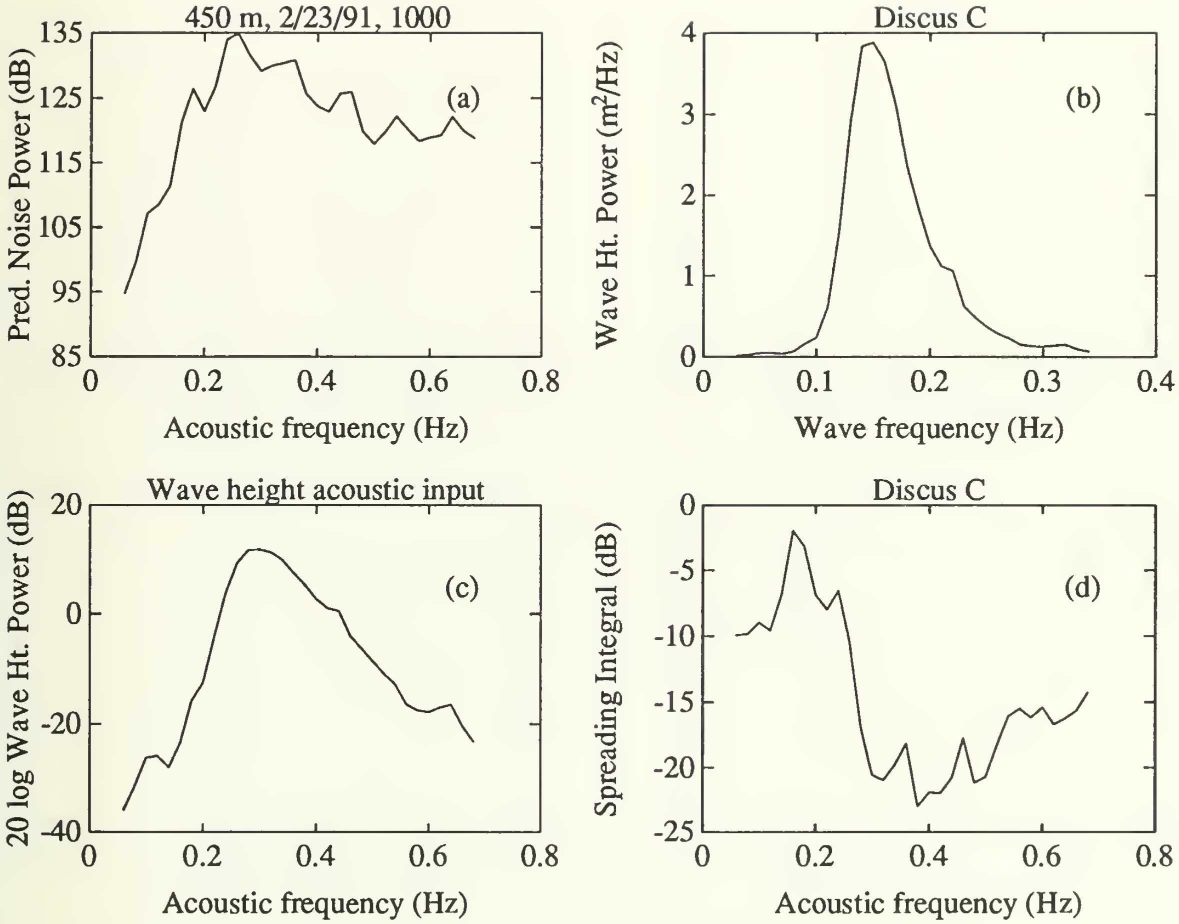

Figure 27: Predicted noise level and inputs for a 450 m receiver on 2/23/91 at 1000. a) Noise spectral level $10 \log P(f)$ in dB *re* $\mu\text{Pa}^2/\text{Hz}$. b) Wave height power spectrum $\Omega(\sigma/2\pi)$ in m^2/Hz. c) Wave height acoustic input $20 \log \Omega(f/2)$ in dB *re* m^2/Hz. d) Spreading integral level $10 \log I_{\alpha_{33}}(f)$ in dB *re* Hz^{-1}.

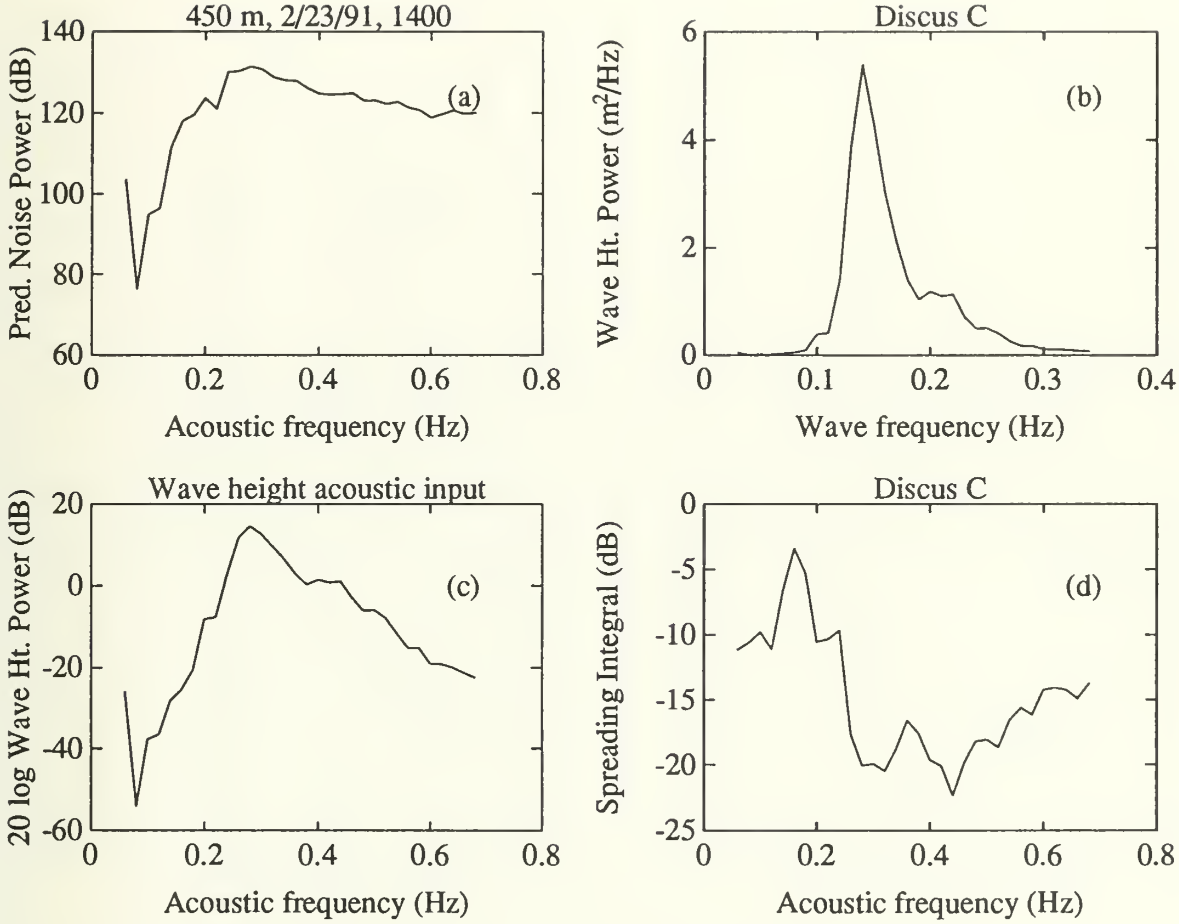

Figure 28: Predicted noise level and inputs for a 450 m receiver on 2/23/91 at 1400. a) Noise spectral level $10 \log P(f)$ in dB *re* $\mu\mathrm{Pa}^2/\mathrm{Hz}$. b) Wave height power spectrum $\Omega(\sigma/2\pi)$ in m^2/Hz. c) Wave height acoustic input $20 \log \Omega(f/2)$ in dB *re* m^2/Hz. d) Spreading integral level $10 \log I_{\alpha_{33}}(f)$ in dB *re* Hz^{-1}.

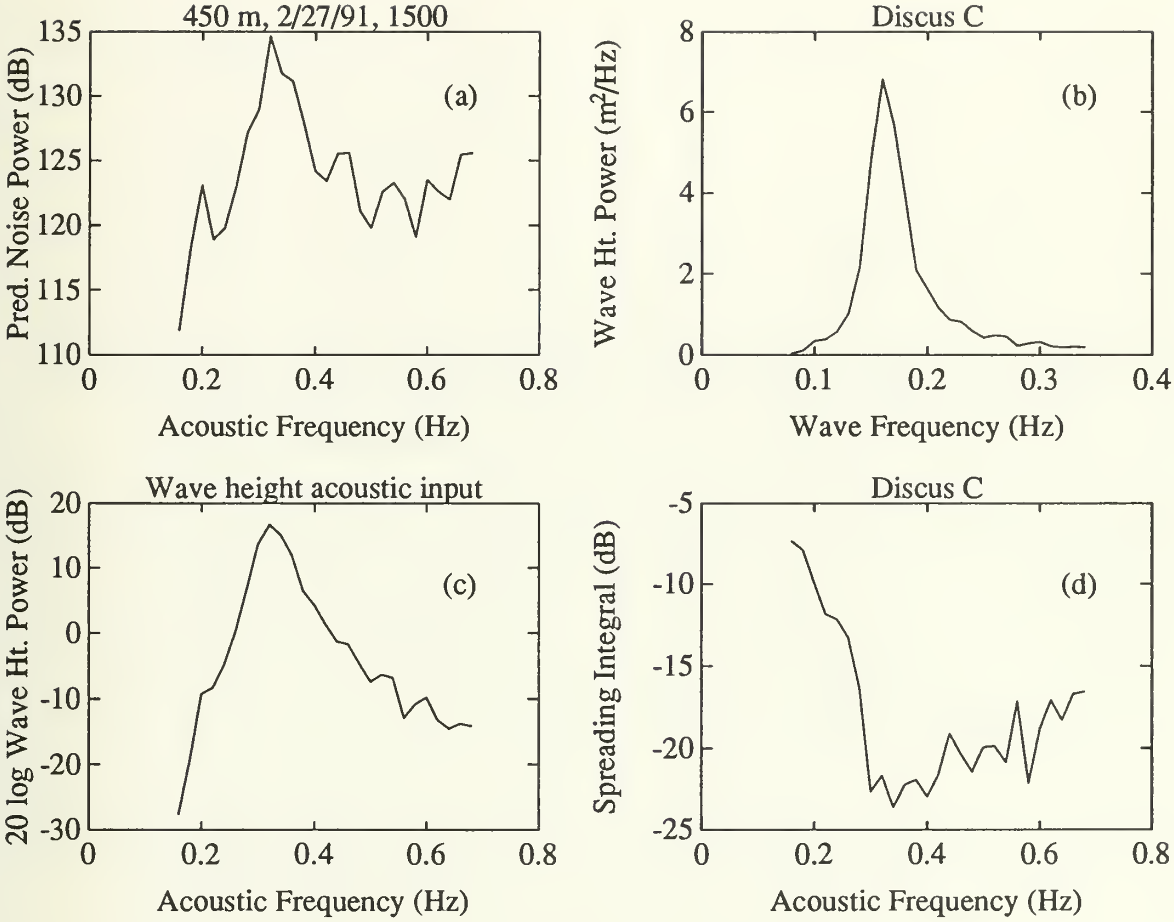

Figure 29: Predicted noise level and inputs for a 450 m receiver on 2/27/91 at 1500. a) Noise spectral level $10 \log P(f)$ in dB *re* $\mu\text{Pa}^2/\text{Hz}$. b) Wave height power spectrum $\Omega(\sigma/2\pi)$ in m^2/Hz. c) Wave height acoustic input $20 \log \Omega(f/2)$ in dB *re* m^2/Hz. d) Spreading integral level $10 \log I_{\alpha_{33}}(f)$ in dB *re* Hz^{-1}.

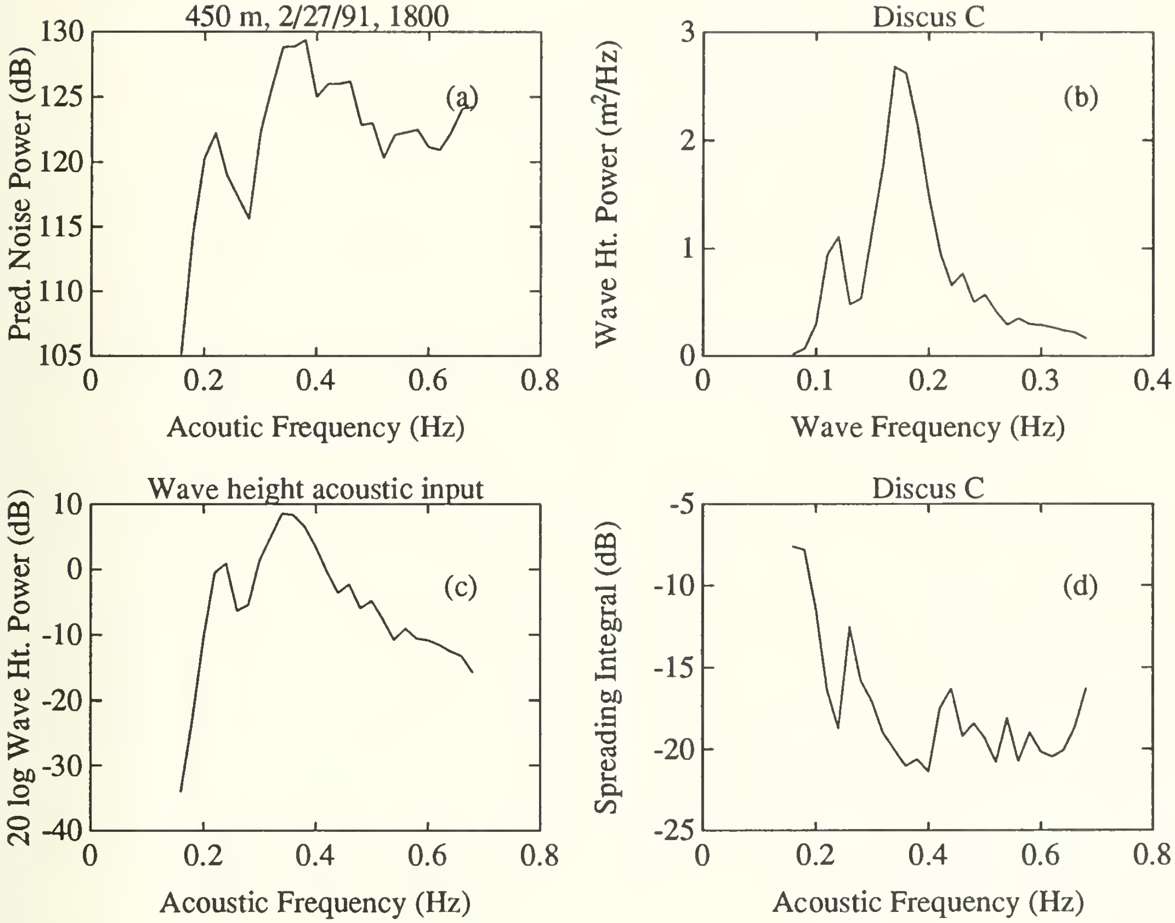

Figure 30: Predicted noise level and inputs for a 450 m receiver on 2/27/91 at 1800. a) Noise spectral level $10 \log P(f)$ in dB *re* $\mu\text{Pa}^2/\text{Hz}$. b) Wave height power spectrum $\Omega(\sigma/2\pi)$ in m^2/Hz. c) Wave height acoustic input $20 \log \Omega(f/2)$ in dB *re* m^2/Hz. d) Spreading integral level $10 \log I_{\alpha_{33}}(f)$ in dB *re* Hz^{-1}.

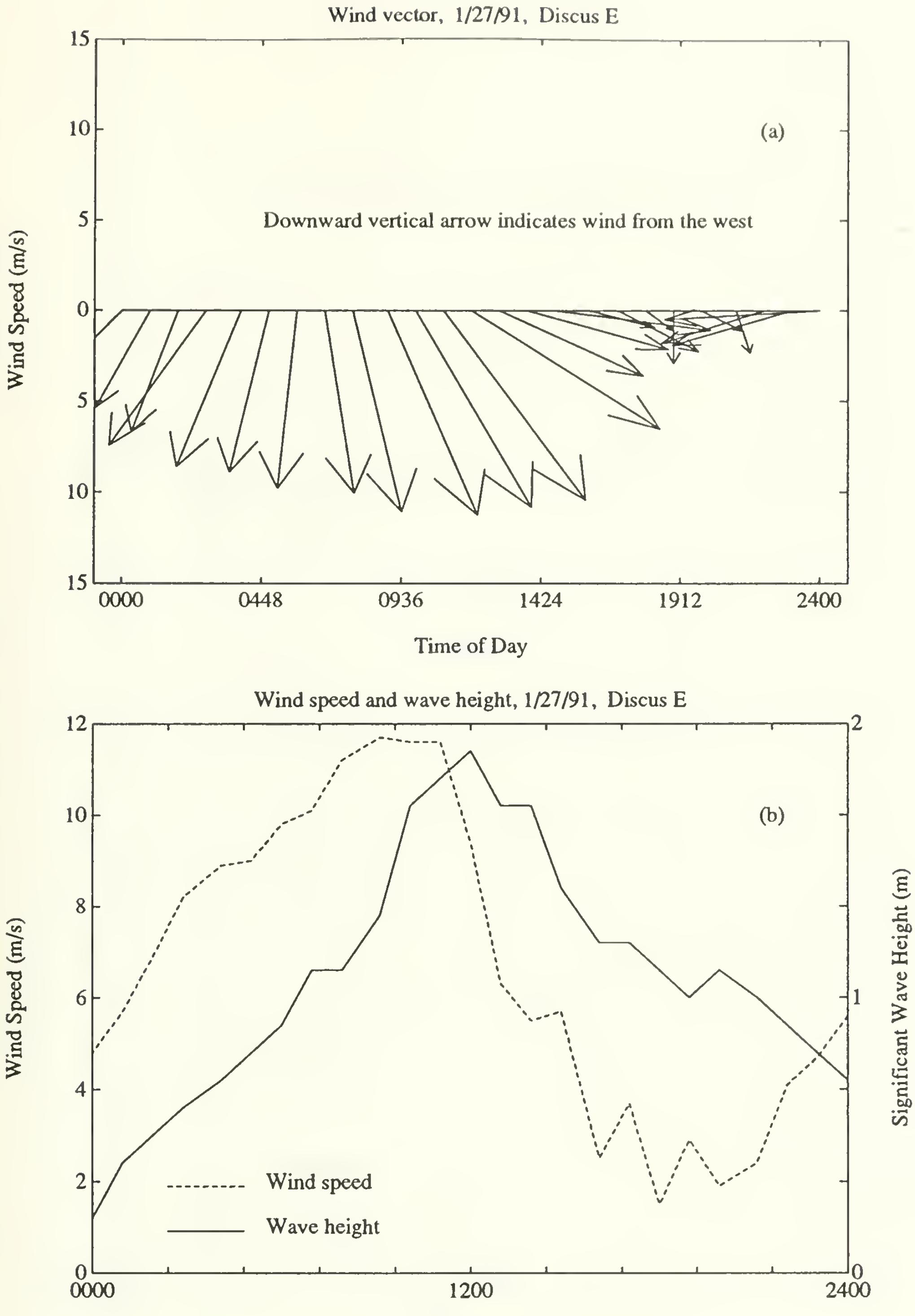

Figure 31: Meteorological data as measured at Discus E on 1/27/91. a) Wind vector. The direction of the arrow indicates the direction of the wind, with a downward arrow indicating a wind from the west. The magnitude of the arrow indicates the wind speed, with the wind speed scale given on the vertical axis. b) Wind speed and wave height.

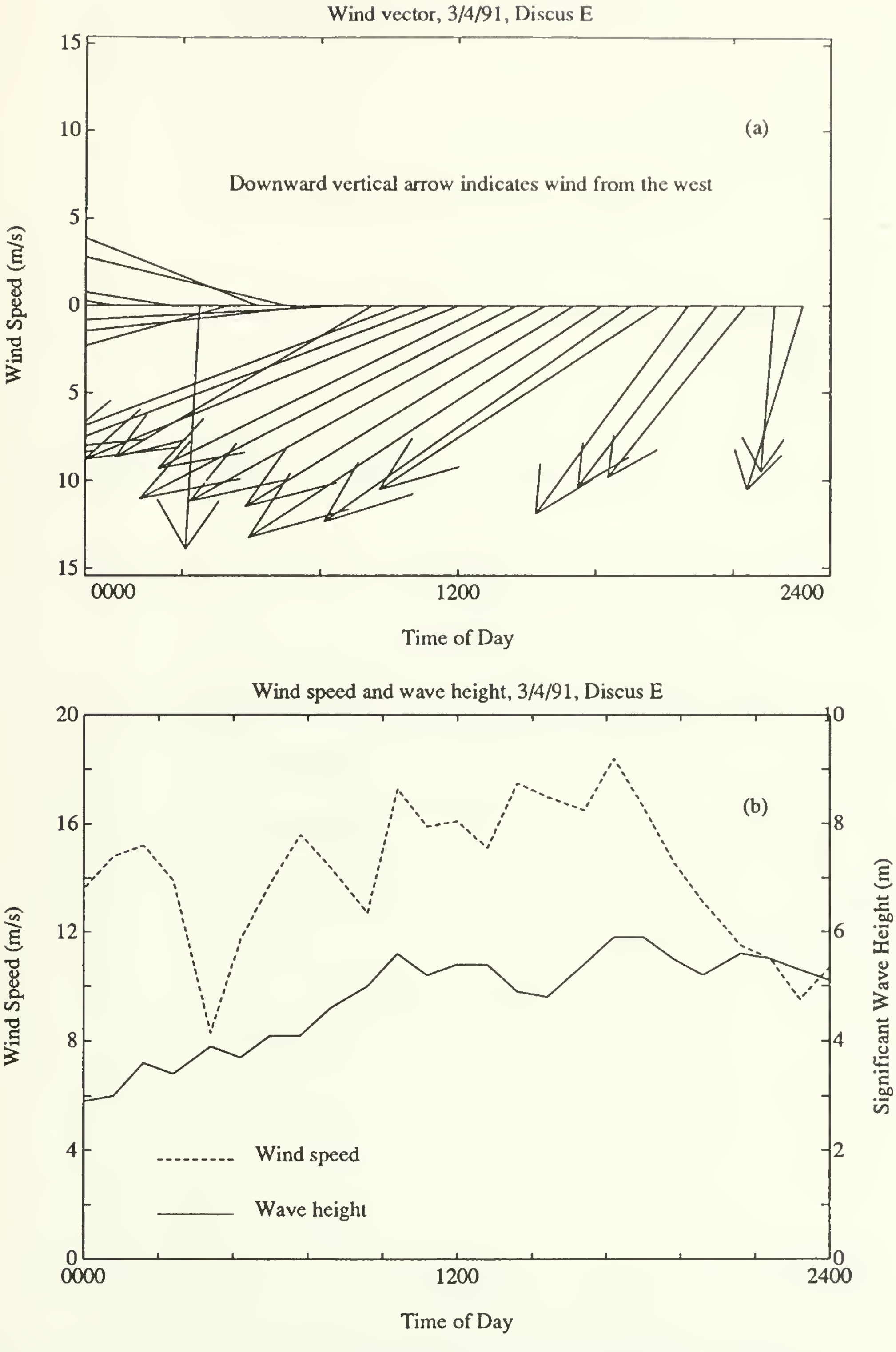

Figure 32: Meteorological data as measured at Discus E on 3/04/91. a) Wind vector. The direction of the arrow indicates the direction of the wind, with a downward arrow indicating a wind from the west. The magnitude of the arrow indicates the wind speed, with the wind speed scale given on the vertical axis. b) Wind speed and wave height.

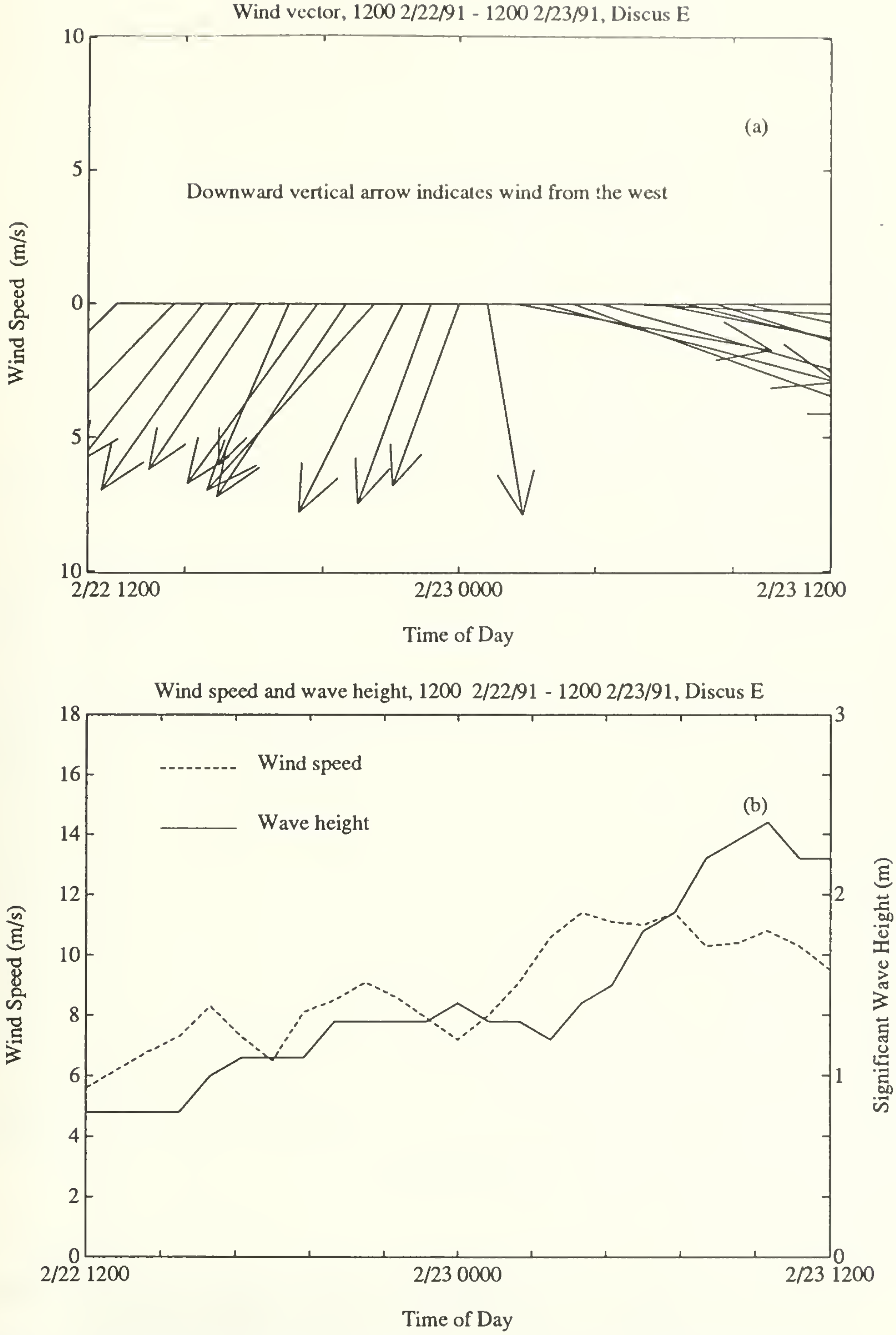

Figure 33: Meteorological data as measured at Discus E on 2/22/91-2/23/91. a) Wind vector. The direction of the arrow indicates the direction of the wind, with a downward arrow indicating a wind from the west. The magnitude of the arrow indicates the wind speed, with the wind speed scale given on the vertical axis. b) Wind speed and wave height.

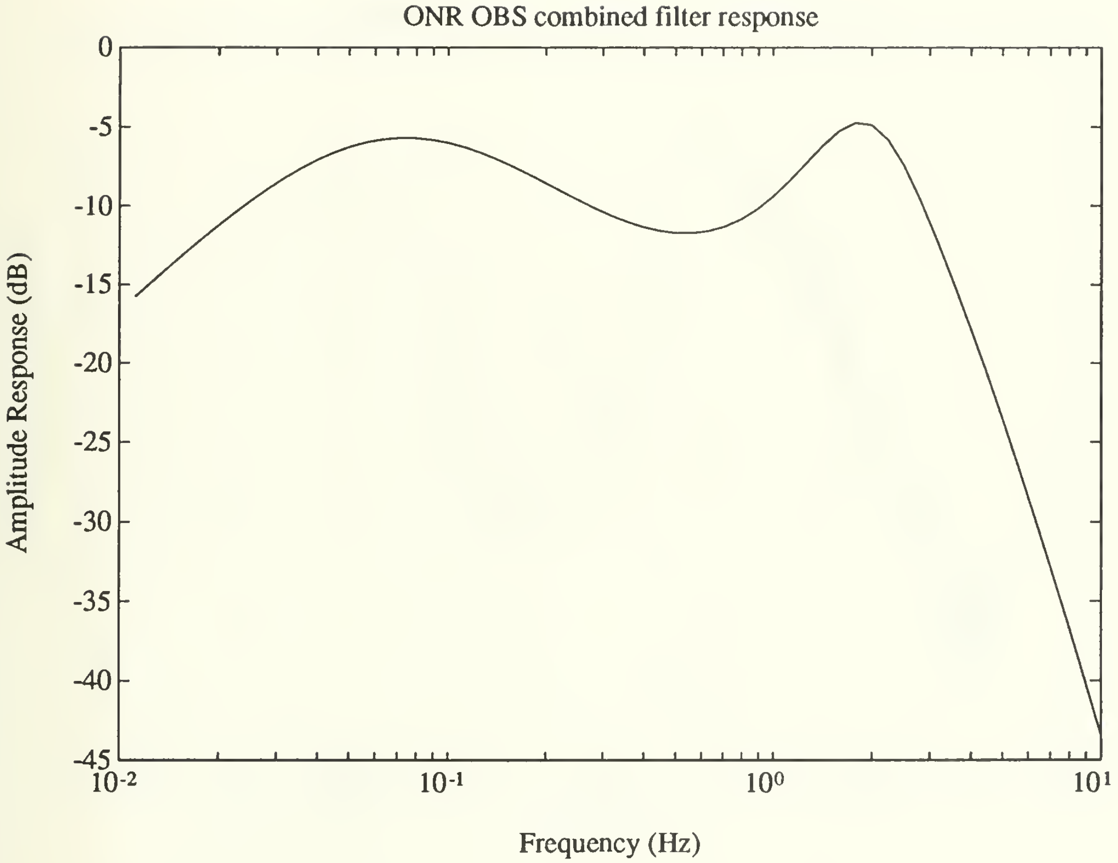

Figure 34: Amplitude response of the anti-aliasing and pre-whitening filter used in the ECONOMEX instruments with an 8 Hz sampling rate. Response amplitude in dB *re* 1 Volt.

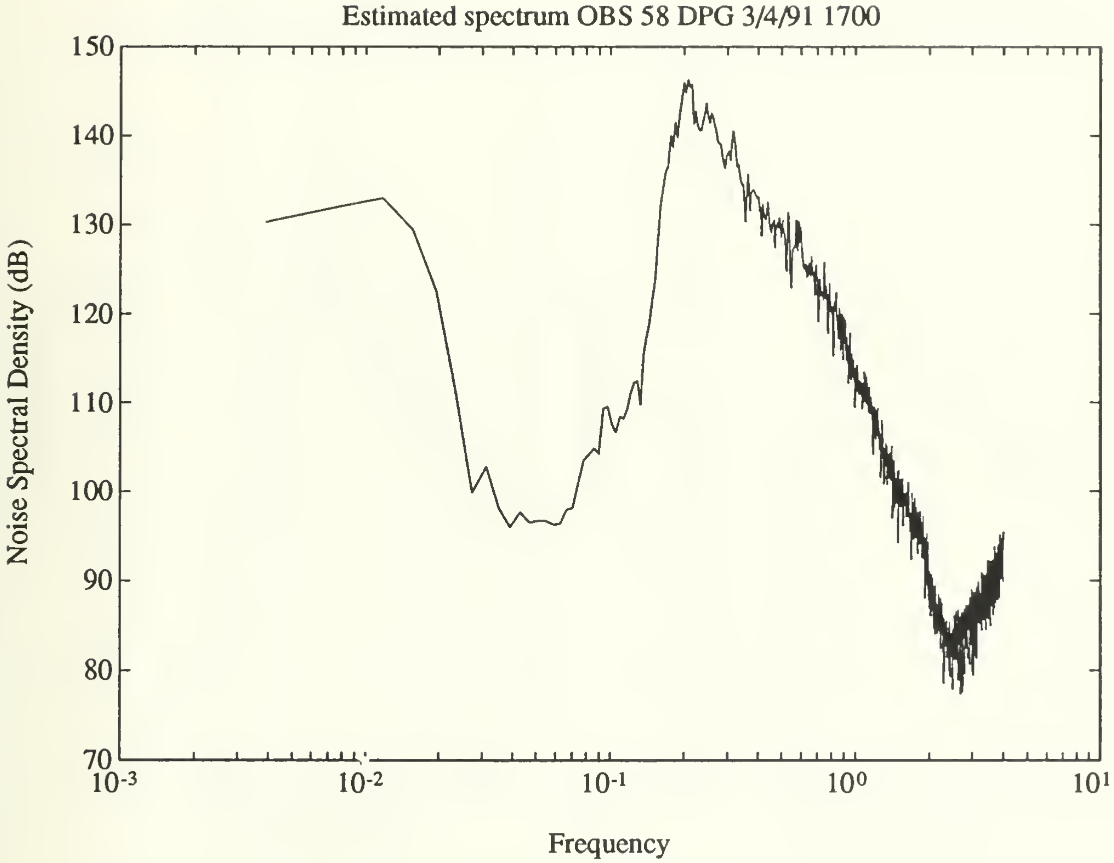

Figure 35: An example of a full spectral estimate using data from OBS 58 DPG on 3/04/91 at about 1700 hours. This spectrum was generated as described in the text with the exception that a 2048 point FFT was used versus a 512 point FFT. The spectral level is in dB *re* $\mu Pa^2/Hz$.

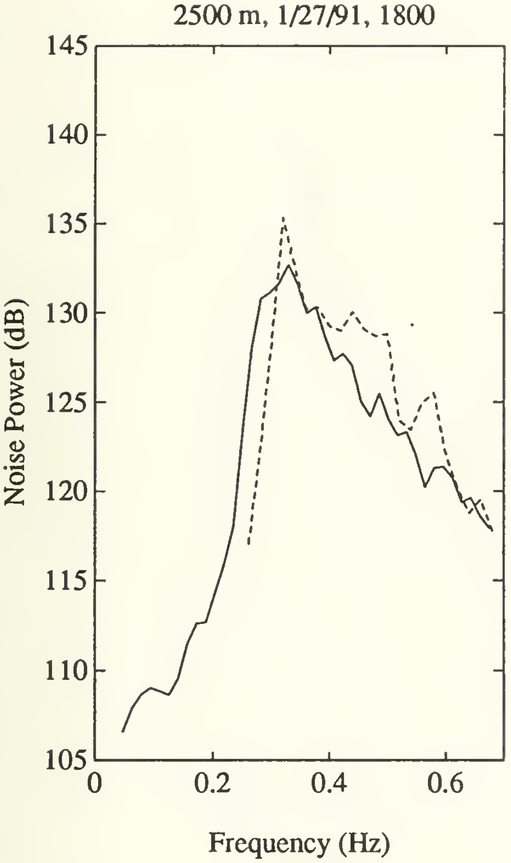

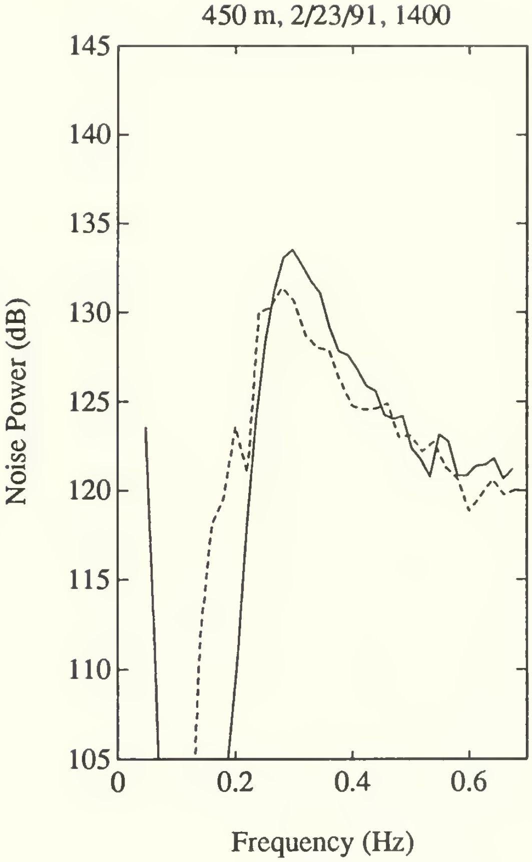

Figure 36: Predicted and observed noise levels, 1/27/91, 1800, OBS 58 (2500 m), in dB *re* $\mu\mathrm{Pa}^2/\mathrm{Hz}$. Observed spectrum is solid curve.

Figure 37: Predicted and observed noise levels, 2/23/91, 1400, OBS 63 (450 m), in dB *re* $\mu\mathrm{Pa}^2/\mathrm{Hz}$. Observed spectrum is solid curve.

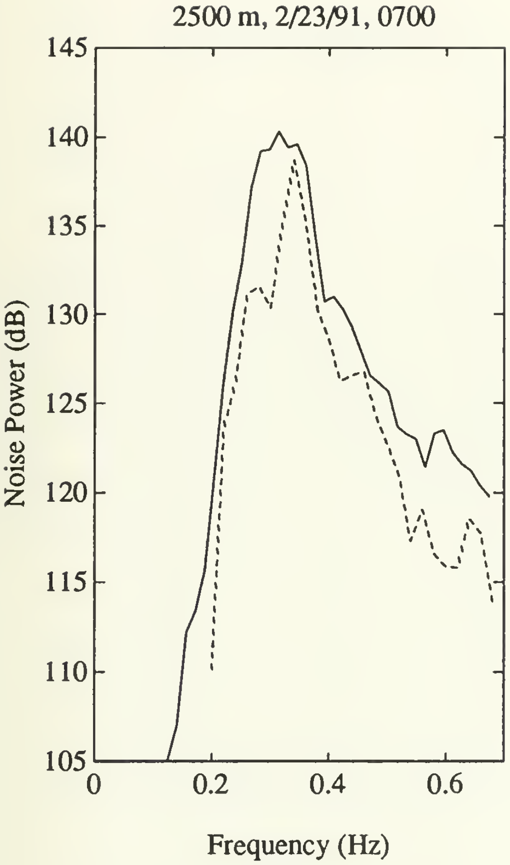

Figure 38: Predicted and observed noise levels, 2/23/91, 0700, OBS 58 (2500 m), in dB *re* μPa^2/Hz. Observed spectrum is solid curve.

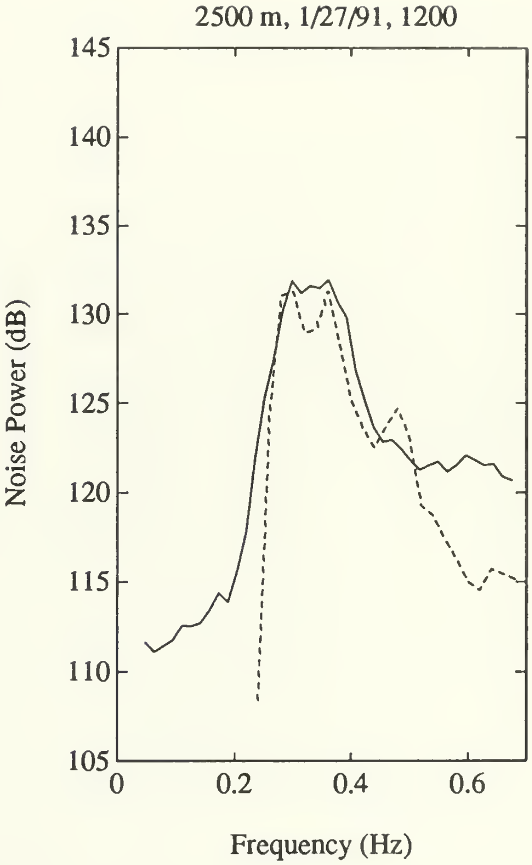

Figure 39: Predicted and observed noise levels, 1/27/91, 1200, OBS 58 (2500 m), in dB *re* μPa^2/Hz. Observed spectrum is solid curve.

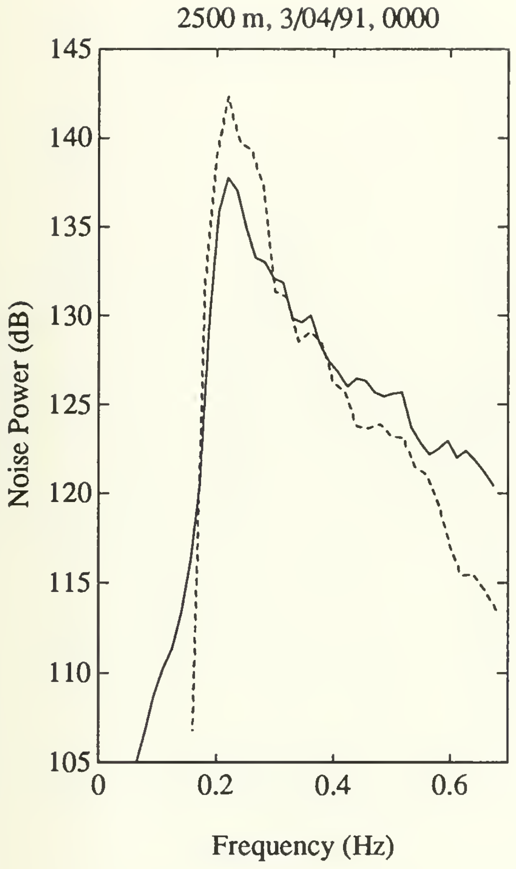

Figure 40: Predicted and observed noise levels, 3/04/91, 0000, OBS 58 (2500 m), in dB *re* $\mu\text{Pa}^2/\text{Hz}$. Observed spectrum is solid curve.

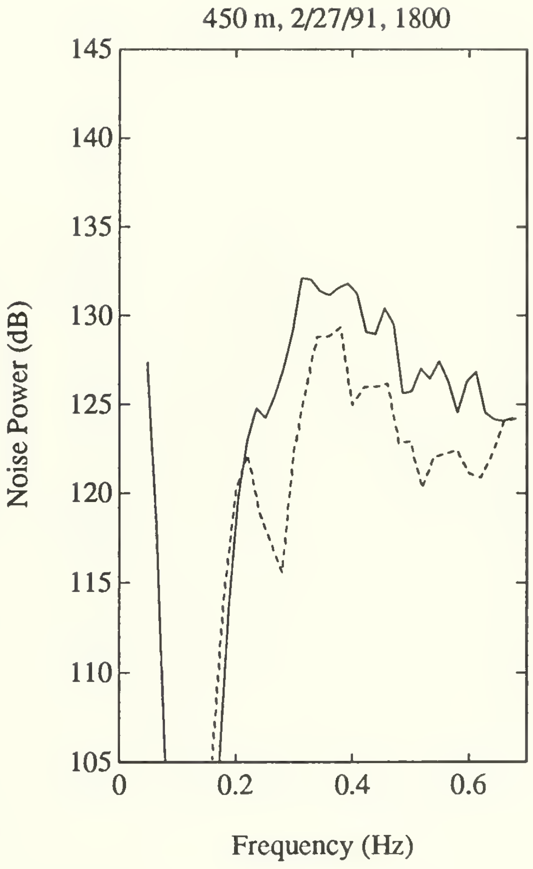

Figure 41: Predicted and observed noise levels, 2/27/91, 1800, OBS 63 (450 m), in dB *re* $\mu\text{Pa}^2/\text{Hz}$. Observed spectrum is solid curve.

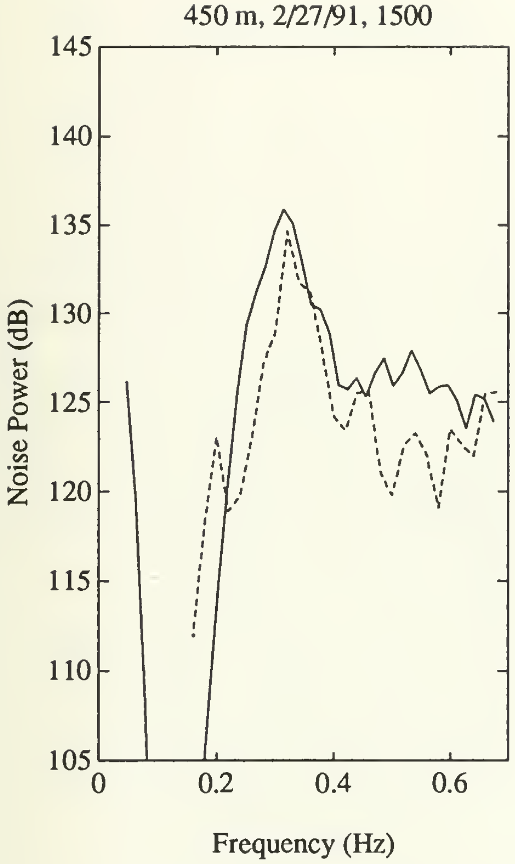

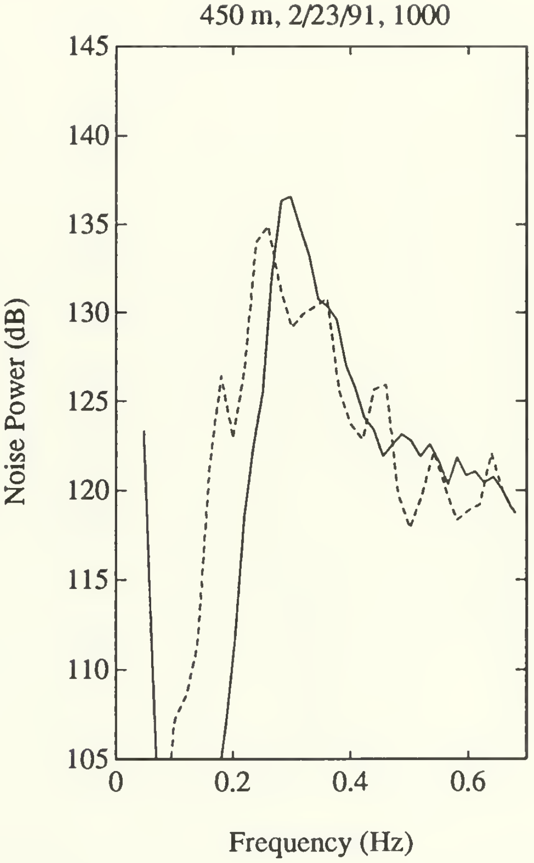

Figure 42: Predicted and observed noise levels, 2/27/91, 1500, OBS 63 (450 m), in dB *re* μPa^2/Hz. Observed spectrum is solid curve.

Figure 43: Predicted and observed noise levels, 2/23/91, 1000, OBS 63 (450 m), in dB *re* μPa^2/Hz. Observed spectrum is solid curve.

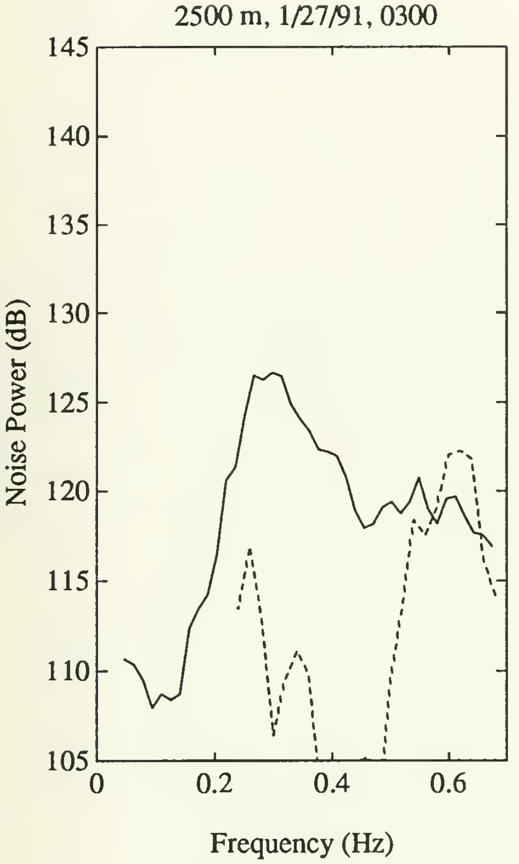

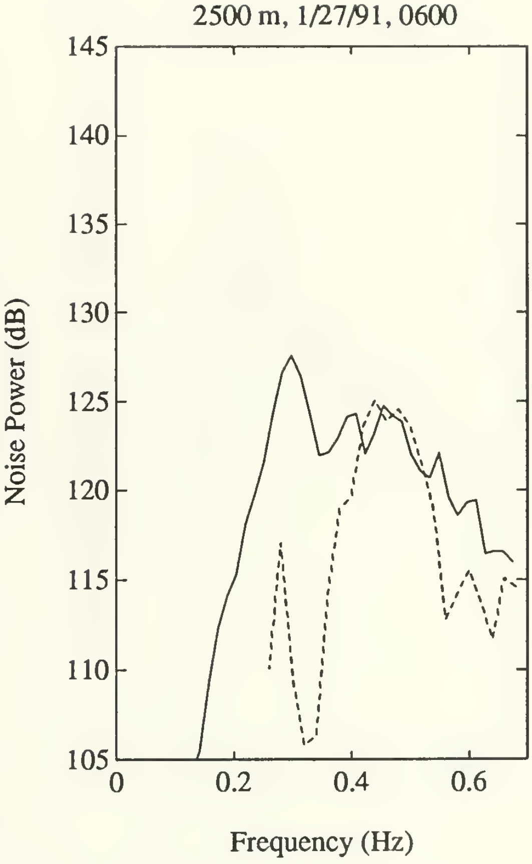

Figure 44: Predicted and observed noise levels, 1/27/91, 0300, OBS 58 (2500 m), in dB *re* $\mu Pa^2/Hz$. Observed spectrum is solid curve.

Figure 45: Predicted and observed noise levels, 1/27/91, 0600, OBS 58 (2500 m), in dB *re* $\mu Pa^2/Hz$. Observed spectrum is solid curve.

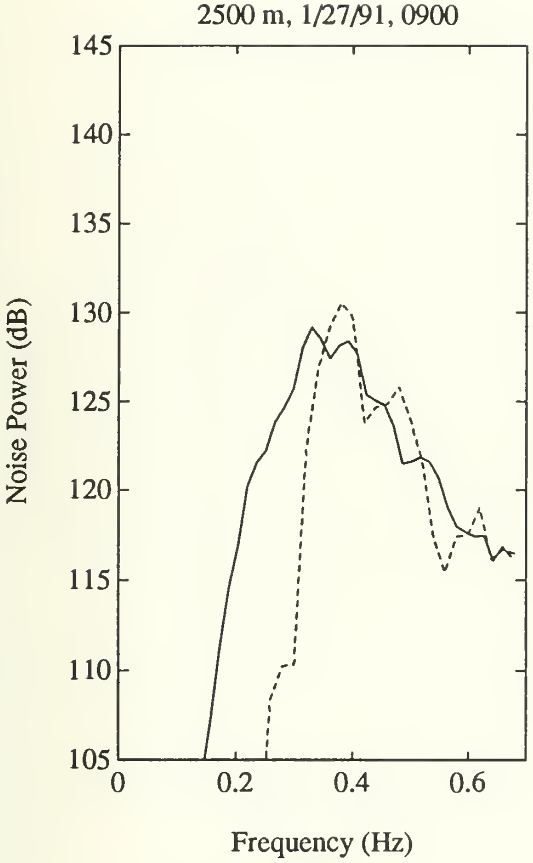

Figure 46: Predicted and observed noise levels, 1/27/91, 0900, OBS 58 (2500 m), in dB *re* $\mu\text{Pa}^2/\text{Hz}$. Observed spectrum is solid curve.

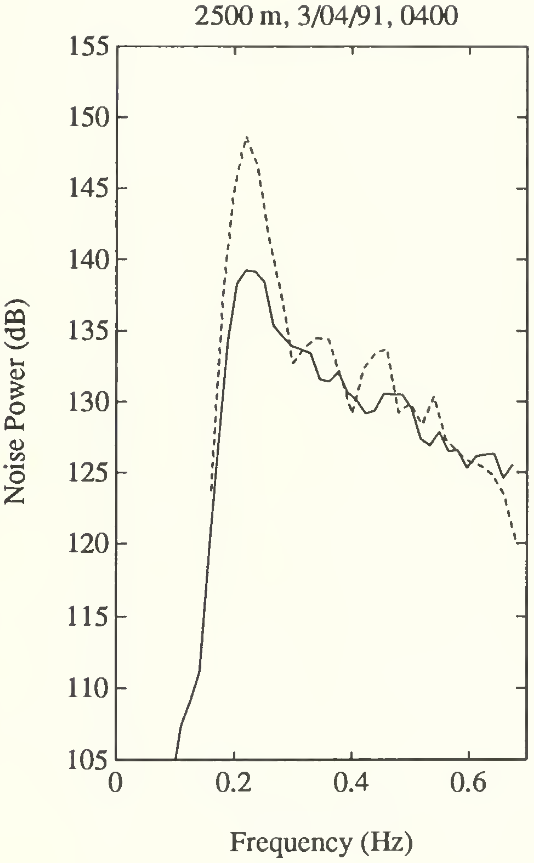

Figure 47: Predicted and observed noise levels, 3/04/91, 0400, OBS 58 (2500 m), in dB *re* $\mu\text{Pa}^2/\text{Hz}$. Observed spectrum is solid curve.

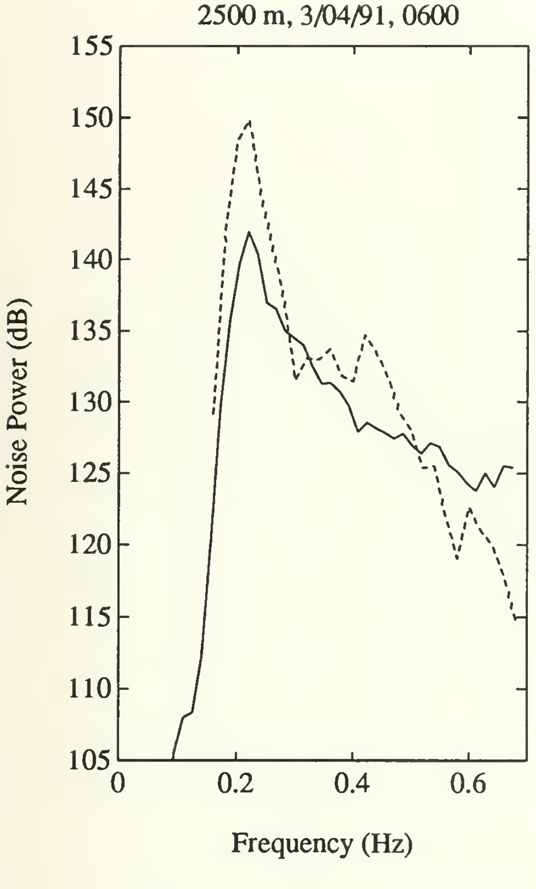

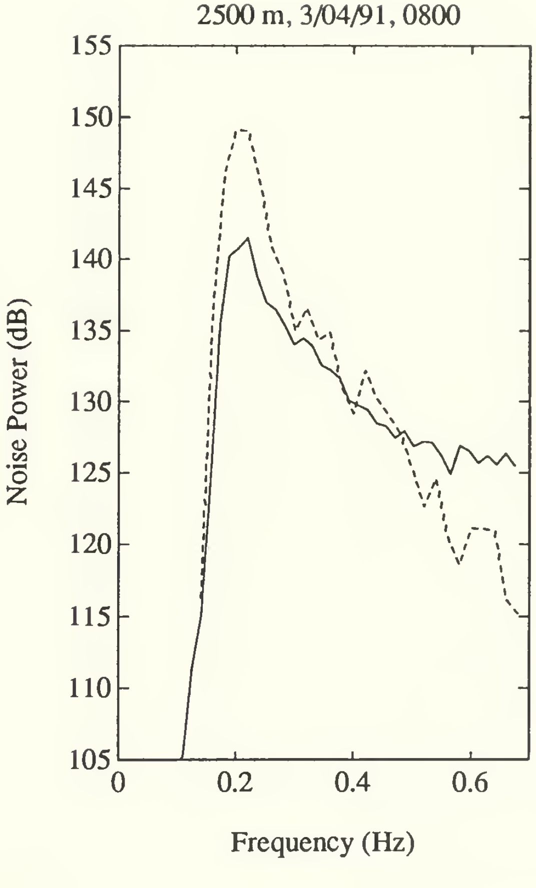

Figure 48: Predicted and observed noise levels, 3/04/91, 0600, OBS 58 (2500 m), in dB *re* $\mu\mathrm{Pa}^2/\mathrm{Hz}$. Observed spectrum is solid curve.

Figure 49: Predicted and observed noise levels, 3/04/91, 0800, OBS 58 (2500 m), in dB *re* $\mu\mathrm{Pa}^2/\mathrm{Hz}$. Observed spectrum is solid curve.

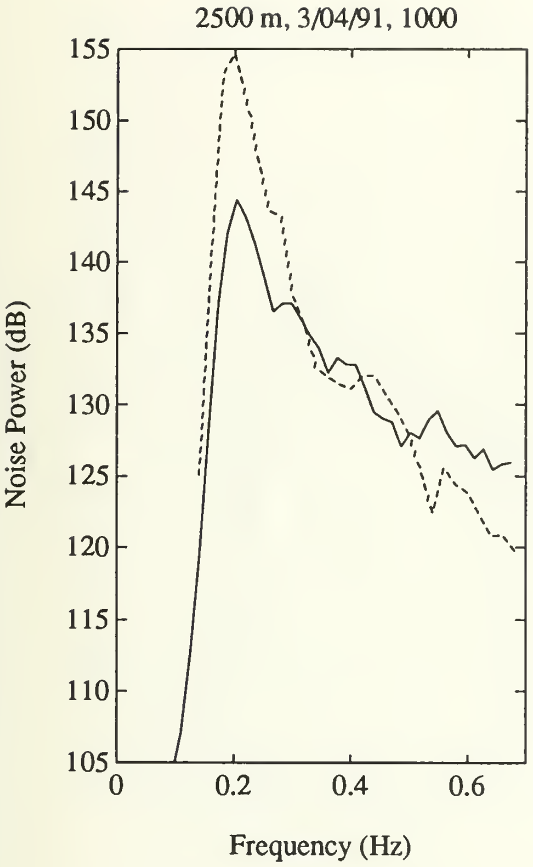

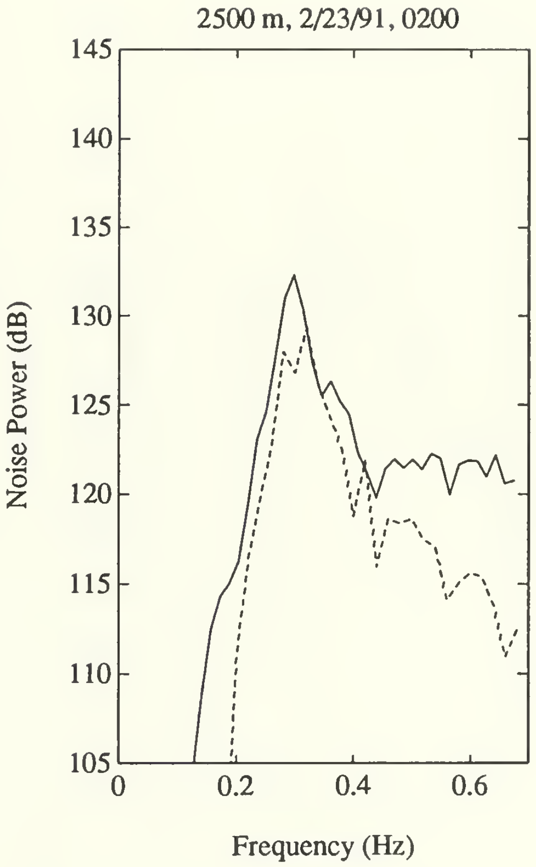

Figure 50: Predicted and observed noise levels, 3/04/91, 1000, OBS 58 (2500 m), in dB *re* μPa^2/Hz. Observed spectrum is solid curve.

Figure 51: Predicted and observed noise levels, 2/23/91, 0200, OBS 58 (2500 m), in dB *re* μPa^2/Hz. Observed spectrum is solid curve.

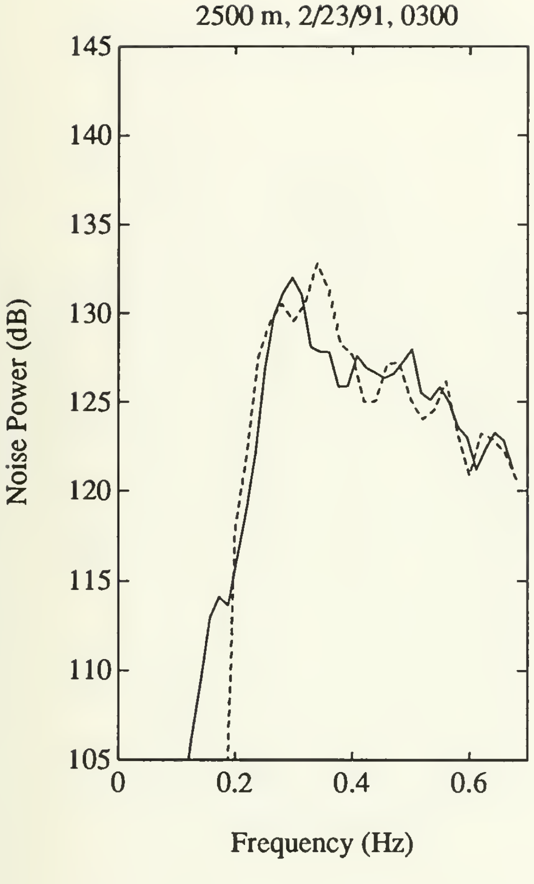

Figure 52: Predicted and observed noise levels, 2/23/91, 0300, OBS 58 (2500 m), in dB *re* $\mu\mathrm{Pa}^2/\mathrm{Hz}$. Observed spectrum is solid curve.

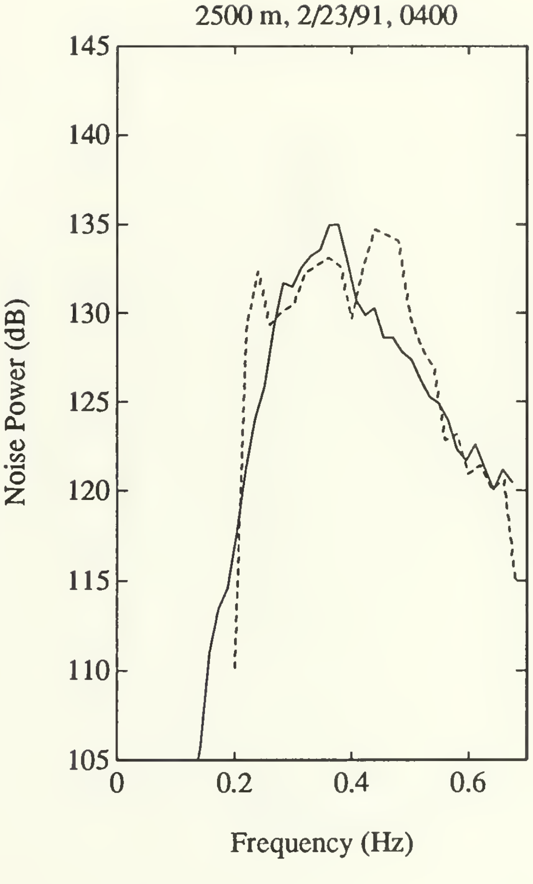

Figure 53: Predicted and observed noise levels, 2/23/91, 0400, OBS 58 (2500 m), in dB *re* $\mu\mathrm{Pa}^2/\mathrm{Hz}$. Observed spectrum is solid curve.

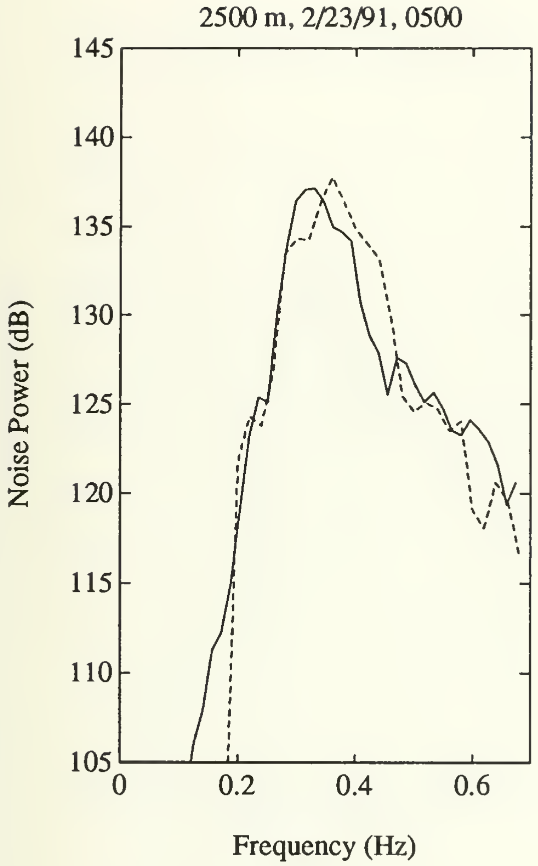

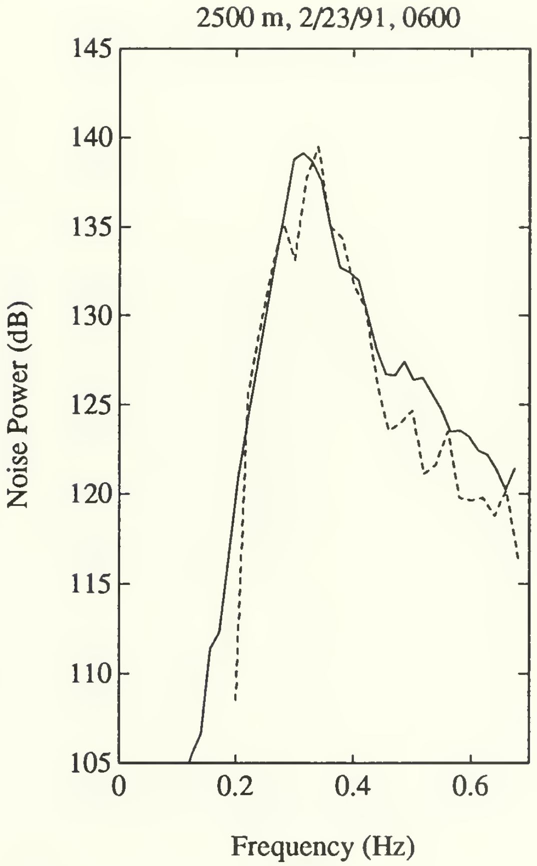

Figure 54: Predicted and observed noise levels, 2/23/91, 0500, OBS 58 (2500 m), in dB *re* $\mu\text{Pa}^2/\text{Hz}$. Observed spectrum is solid curve.

Figure 55: Predicted and observed noise levels, 2/23/91, 0600, OBS 58 (2500 m), in dB *re* $\mu\text{Pa}^2/\text{Hz}$. Observed spectrum is solid curve.

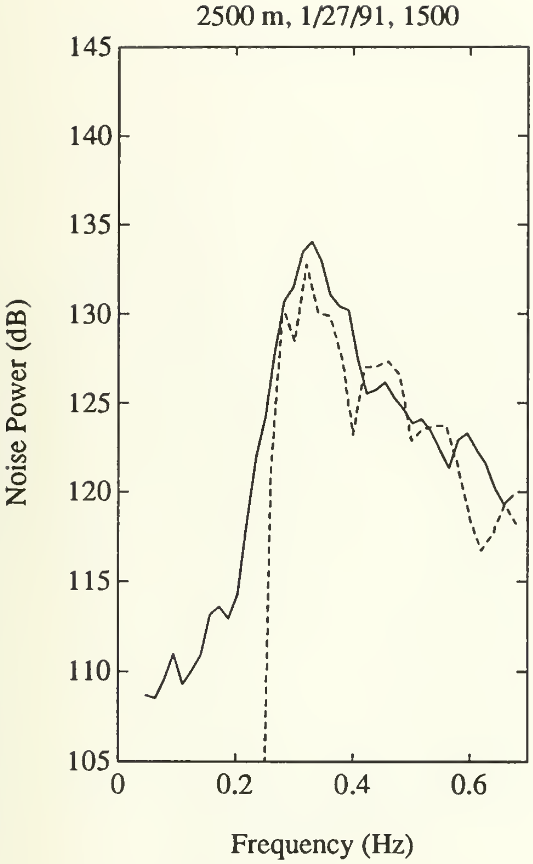

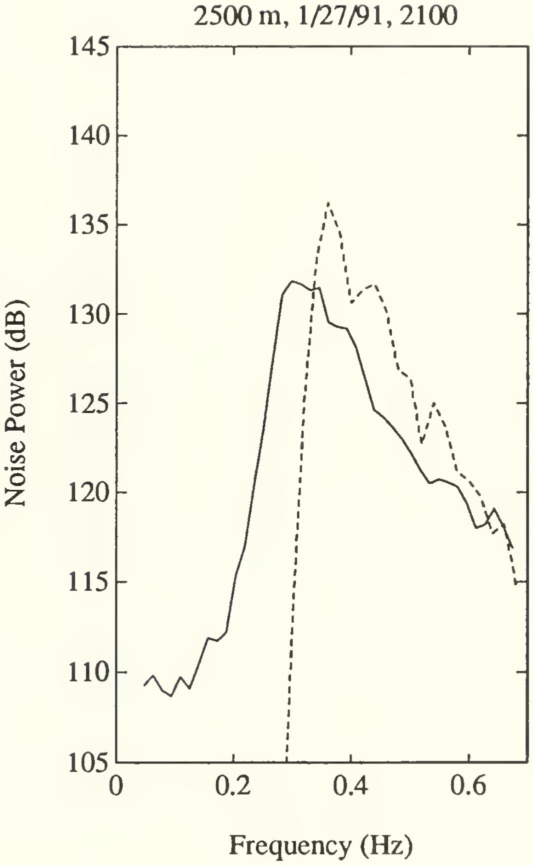

Figure 56: Predicted and observed noise levels, 1/27/91, 1500, OBS 58 (2500 m), in dB *re* μPa^2/Hz. Observed spectrum is solid curve.

Figure 57: Predicted and observed noise levels, 1/27/91, 2100, OBS 58 (2500 m), in dB *re* μPa^2/Hz. Observed spectrum is solid curve.

492-767

Thesis
L663232 Lindstrom
c.1
Predictions and observations of seafloor infrasonic noise generated by sea surface orbital motion.

Thesis
L663232 Lindstrom
c.1
Predictions and observations of seafloor infrasonic noise generated by sea surface orbital motion.

AMERICAN BINDERY
TOPEKA, KANSAS

DUDLEY KNOX LIBRARY

3 2768 00014315 0